UNIVERSITY OF OKLAHOMA

GRADUATE COLLEGE

RADAR AND THERMODYNAMIC ANALYSIS OF THE 6 APRIL 2018 MONROE, LA TORNADIC SUPERCELL

A THESIS

SUBMITTED TO THE GRADUATE FACULTY

in partial fulfillment of the requirements for the

Degree of

MASTER OF SCIENCE IN METEOROLOGY

By

MICHAEL JOSEPH HOSEK
Norman, Oklahoma
2022

RADAR AND THERMODYNAMIC ANALYSIS OF THE 6 APRIL 2018 MONROE, LA TORNADIC SUPERCELL

A THESIS APPROVED FOR THE
SCHOOL OF METEOROLOGY

BY THE COMMITTEE CONSISTING OF

Dr. Michael Biggerstaff, Chair

Dr. Conrad Ziegler

Dr. Cameron Homeyer

Acknowledgements

I first would like to thank my adviser, Dr. Conrad Ziegler, and my committee members, Dr. Michael Biggerstaff and Dr. Cameron Homeyer, for their support and guidance during this project. I also want to thank Dr. Zhien Wang for his assistance in interpreting the CRL results and Dr. Daniel Stechman for helping me run and understand the various scripts used in this project. And I want to thank all of those who participated in VORTEX-SE 2018 and provided the unique dataset I was able to analyze.

I would like to thank my parents, Maureen and Matthew Hosek, and my siblings, Matthew Jr. and Melissa, for their continual support and encouragement. I would also like to thank my friends here at the School of Meteorology, not only for making this unbearable process slightly more bearable, but also for their help in bringing me up to speed on the meteorological concepts I did not yet have experience with.

This research was funded by NSF grant AGS-1917701, and computer and infrastructure support provided by the National Severe Storms Laboratory.

Table of Contents

List of Tables

List of Figures

Abstract

This case study analyzes a tornadic supercell observed in northeast Louisiana as part of the Verification of the Origins of Rotation in Tornadoes Experiment Southeast (VORTEX-SE) on April 6—7 2018. Two mobile research radars (SR2 and SR3), one WSR-88D equivalent (KULM) and two airborne radars (TAFT and TFOR) sampled the storm at close proximity for ~70 minutes through its mature phase, tornadogenesis at 2340 UTC, and dissipation and subsequent ingestion into a developing MCS segment. The 4-D wind field and reflectivity from up to five-Doppler analyses every five minutes, combined with 4-D Diabatic Lagrangian Analysis (DLA, Ziegler 2013a,b) retrievals, enabled kinematic and thermodynamic analysis of storm-scale boundaries leading up to, during, and after the dissipation of the 13 minute-long EF-0 tornado. Additional near-storm thermodynamic measurements from the Compact Ramen Lidar (CRL), a P-3 aircraft-mounted downward-pointing lidar which profiles boundary layer water vapor mixing ratio and temperature, were compared to far-field proximity soundings to provide an accurate representation of the storm inflow environment.

Trajectory analysis using the DLA reveals that ambient environmental low-level vertical vorticity was present in the inflow region, and additional low-level vertical vorticity appeared to be generated by the shearing zone between the Rear-Flank Gust Front (RFGF) and inflow at the location of tornadogenesis. Baroclinically-generated horizontal vorticity which was tilted into vertical by downdrafts did not appear to be a significant source of vorticity for the tornado.

The kinematic and thermodynamic analysis also reveal a transient current of baroclinically-generated low-level streamwise vorticity leading into the low-level supercell updraft, appearing similar to the Streamwise Vorticity Current (SVC) that has been identified in supercell simulations and observed only kinematically previously. Although the SVC did not

directly feed streamwise vorticity to the tornado-cyclone, its development coincided with tornadogenesis.

The evolution of the supercell’s updraft and its induced surface boundaries were investigated in the context of its unique vertical thermodynamic profile and hodograph compared to most previous observations and simulations based on Central Plains supercells. Although the mesoscale environment was not high-shear/low-CAPE, the Monroe supercell shared many similarities to such storms due to meager temperature lapse rates aloft which are commonplace in southeast severe convection events.

Chapter 1: Introduction

The Verification of the Origins of Rotation in Tornadoes Experiment Southeast (VORTEX-SE) program was designed to study the formation, intensity, structure, and path of tornadoes which occurred in the southeastern United States. Study in this area is particularly important due to the overlap of environmental and socioeconomic factors which result in the Southeast region having the greatest concentration of tornado-related fatalities, including but not limited to the following: (1) tornado events occurring during seasons not traditionally associated with tornadoes (i.e., the cool season); (2) fast storm motions through complex and forested terrain; and (3) an overall higher population density than the Central Plains region (Ashley 2007). Southeast tornado events tend to occur in environments with lower Convective Available Potential Energy (CAPE) and larger vertical wind shear than their Central Plains counterparts, making them more difficult to accurately forecast and warn on (Anderson-Frey et al. 2019) and changing some of the larger storm-scale structures we are typically used to seeing in high-CAPE/high-shear Central Plains tornadic supercells (Wade and Parker 2021). VORTEX-SE represents the first VORTEX project not focused on Central Plains convection, providing a wealth of observations which can be analyzed against the observations, simulations, and conceptual models derived from earlier supercell research focused in the Central Plains region. This thesis will present multi-radar analysis results from a moderate-CAPE/high-shear tornadic supercell observed as part of the VORTEX-SE program on 6 April 2018.

1.1. Supercell and non-supercell storm dynamics and tornadogenesis

The defining characteristic of a supercell thunderstorm is its rotating mesocyclonic main updraft. A mesocyclone is broadly defined as a column of rotating air 3—9 km wide within the convective updraft containing at least 10×10^{-3} s^{-1} vertical vorticity (Davies-Jones 1984).

Supercells are typically prolific producers of severe wind gusts, severe hail, the majority of tornadoes, and nearly all strong (EF2+) tornadoes (Davies-Jones 1984; Smith et al. 2012). The mesocyclone can usefully be partitioned into three different layers: the mid-level mesocyclone (common to all supercells), defined here as being within the 1—3 km AGL layer; the low-level mesocyclone from 0—1 km AGL (Davies-Jones 1984), which is necessary for all supercellular tornadoes but can also be present in non-tornadic supercells; and the upper-level mesocyclone above 3 km AGL. Mesocyclone classification in this manner is based on the source of vertical vorticity which feeds it. Decades of observations and modeling have shown that the mid-level and upper-level mesocyclone develops as a result of the tilting of ambient horizontal vorticity into the vertical as air parcels are carried into the updraft (Barnes 1970; Rotunno 1981; Davies-Jones 1984; Lilly 1986; Adlerman et al. 1999; Mashiko 2016).

While sufficient for the development of the mid-level mesocyclone, the tilting and subsequent stretching of ambient horizontal vorticity is insufficient to develop either the low-level low-level mesocyclone or a tornado, since the tilting process by the main supercell updraft also carries air parcels up away from the surface (Davies-Jones 1982). Further observational and simulation studies focused on the low-level mesocyclone have revealed that the low-level mesocyclone often develops from the tilting of baroclinically-generated horizontal vorticity in the low levels of the storm (Davies-Jones and Brooks 1993; Rotunno and Klemp 1985; Wicker and Wilhelmson 1995; Markowski et al. 2012, part II; Dahl et al. 2014; Parker and Dahl 2015; Dahl 2015; Marquis et al. 2016). A slippage mechanism whereby parcels descending in the rear-flank downdraft (RFD) experience rotation of the vector vorticity toward the horizontal via persistent baroclinic forcing can importantly generate positive vertical vorticity as the parcel exits the RFD at very low levels and subsequently experience rapid stretching intensification as the parcel enters the low-level updraft base (Davies-Jones and Brooks 1993). The baroclinic mechanism (also known as the solenoidal mechanism) generates horizontal vorticity via a secondary circulation induced by the temperature difference across a boundary, with air rising while moving toward the cool air from the warm side and sinking while moving toward the warm air from the cool side (Davies-Jones 2000).

Numerous low-level boundaries have been shown to exist between the supercell's inflow region and both its forward-flank downdraft (FFD) and RFD as a result of a surface-based cold pool (Figure 1) being created by diabatic cooling from rain evaporation and graupel/hail melting (Lemon and Doswell 1979; Beck and Weiss 2013, hereafter referred to as BW13). The forward-flank in particular has seen increased research attention over the last decade as it has become clear that it plays a significant role in mesocyclogenesis. The BW13 simulation showed that, in addition to the Rear Flank Gust Front (RFGF), two kinematic and thermodynamic boundaries exist within supercells: the Left-Flank Convergence Boundary (LFCB) and the Forward-Flank Convergence Boundary (FFCB). Unlike the RFGF, which features a notable wind shift with strong, gusty winds as the RFD and inflow collide, the LFCB and FFCB feature subtle confluence within a long fetch of along-boundary flow extending from the forward-flank to the low-level main updraft. The LFCB in a classic supercell often separates diabatically-cooled air at the surface from diabatically-cooled air descending from aloft in the FFD, and tends to be located within the front-left quadrant of the storm's main precipitation region relative to the main updraft motion. The FFCB in a classic supercell often extends into the inflow sector and across the forward anvil, thus separating unmodified surface inflow air from air which has been slightly cooled in the distant forward flank. Both of these forward-flank boundaries have been shown to produce baroclinically-generated streamwise horizontal vorticity (BW13).

Baroclinically-generated horizontal vorticity has been shown in simulations (e.g., Orf et al. 2017) and observations (e.g., Markowski et al. 2012b) to play a significant role in the development of the low-level mesocyclone. A very high resolution supercell simulation depicted a concentrated flow of streamwise vorticity – the "Streamwise Vorticity Current" (SVC) – extending along a forward flank baroclinic boundary at low levels and feeding the low-level mesocyclone (Orf et al. 2017). The SVC has been shown in simulations to develop as a combination of baroclinically-generated streamwise vorticity in a Kelvin-Helmholtz wave-like circulation at the baroclinic boundary and horizontal stretching of both ambient and baroclinically-generated streamwise vorticity as airflow accelerates into the low-level updraft (Schueth et al. 2021). By enhancing the amount of streamwise vorticity ingested by a low-level updraft, the SVC enables a low-level mesocyclone to develop and intensify as even minimal low-level tilting of an intense SVC results in a large vertical vorticity concentration. Although the SVC does not directly feed a tornado, simulations have associated its onset with the subsequent onset of tornadogenesis, and have analogously associated its dissipation with tornado dissipation (Orf et al. 2017). Although the KH-wave morphology of the SVC has been identified in single-radar radial velocity observations (Murdzek et al. 2020; Schueth et al. 2021), the present thesis to the author's knowledge presents the first radar-based thermodynamic retrieval of an SVC. Due to the SVC's narrow width and confinement within roughly the lowest 1 km AGL, even obtaining single-radar data and corresponding multi-radar analyses with the necessary fine spatial resolution is challenging, and independent low- or mid-level in situ thermodynamic observations have until recently been unavailable to document the morphology of the surface-based supercell outflow precipitation boundary layer.

Despite decades of significant progress, many questions regarding the multi-faceted tornadogenesis process remain. The tornadogenesis process can broadly be divided into two sub-categories: supercell and non-supercell tornadogenesis. Non-supercell tornadogenesis involves barotropically-generated low-level vertical vorticity becoming collocated with an updraft, which then intensifies the vertical vorticity into a tornado via low-level stretching (Wakimoto and Wilson 1989). The pure non-supercell tornadogenesis process does not involve any baroclinic boundaries or downdrafts produced by a convective storm. Instead, the low-level vertical vorticity is generated by the horizontal shear along the kinematic boundary between two different flow regimes (Wakimoto and Wilson 1989). Non-supercellular tornadoes are typically associated with slow-moving convective updrafts along a kinematic boundary, particularly early in the life cycle of the storm. It has been speculated that vertical vortices spawned by a horizontal shearing instability (HSI) may “roll-up” at the surface along the flanking lines of supercells and result in dust-devil like low-level misovortical circulations, that in turn may connect with and experience stretching intensification in deep-convective flanking line updrafts or play a role in some way in supercellular tornadoes (Brandes 1977; Wakimoto and Wilson 1989; Lee and Wilhelmson 1997a-b; Buban and Ziegler 2016a-b).

Baroclinic supercellular tornadogenesis involves the tilting and stretching of baroclinically generated low-level streamwise horizontal vorticity into the vertical due to a distinctive phasing of downdrafts with the main supercell updraft. Although there has conventionally been a particular focus on the RFD and the RFD surge associated with tornadogenesis, there is residual uncertainty regarding which downdrafts within the storm contribute the most to tornadogenesis (Davies-Jones and Brooks 1993; Walko 1993; Wicker and Wilhelmson 1995; Adlerman et al. 1999; Markowski et al. 2008, 2012, 2014; Dahl et al. 2014;

Dahl 2015; Marquis et al. 2016). Specifically, streamwise vorticity is baroclinically generated in parcels within the lowest hundred meters AGL, and the horizontal vorticity is reoriented into vertical vorticity as these parcels descend within a downdraft towards the surface (e.g., Davies-Jones and Brooks 1993; Dahl et al. 2014). This process enables the growth of positive vertical vorticity near the surface which can be immediately intensified via stretching if the parcel subsequently enters the base of the low-level updraft. Once the tornado develops, its associated intense low-level updraft is thought to be able to sufficiently tilt baroclinically-generated streamwise vorticity into vertical vorticity close enough to the ground such that the tornado can be sustained (Markowski et al. 2012; Marquis et al. 2016; Mashiko 2016). However, in the absence of a tornado already being present, there does not exist a low-level updraft strong enough to tilt baroclinically-generated horizontal vorticity into vertical vorticity close enough to the surface to initiate a tornado (Davies-Jones and Markowski 2013). Although baroclinically-generated vorticity is believed to be crucial for supercell tornadogenesis, observational studies have found that tornadogenesis is more likely in supercells with cold pool deficits less than 5°C relative to inflow (Markowski et al. 2002; Shabbott and Markowski 2006; Grzych et al. 2007; Hirth et al. 2008; Markowski et al. 2012a-b; Weiss et al. 2015; Markowski et al. 2018). These observational findings imply that a delicate balance exists between the need for baroclinically-generated vorticity by the developing low-level mesocyclone on the one hand, versus the required diabatic parcel cooling that also increases negative buoyancy and in turn resists vertical updraft acceleration required for stretching.

1.2. Storm analysis via multi-Doppler radar synthesis and thermodynamic retrieval

Dual-Doppler and multi-Doppler (three or more) radar analyses using a variety of mobile and fixed radars have been used to study supercells over the past four decades (e.g., Ray 1976).

As radar technology and deployment techniques have improved, the spatial and temporal resolution of these observations have improved to the point where we are able to observe the finescale internal details of supercells, including the low-level mesocyclone and tornado-cyclone (the larger parent circulation of the tornado), although direct Doppler radar observations of tornadoes themselves remains challenging (e.g., Wurman and Ghil 2000). The distance from a radar to the target supercell of interest can greatly limit the low-level data that can be collected and analyzed, and the lowest several hundred meters are of upmost importance for processes like tornadogenesis (e.g., Markowski et al. 2018). This problem is exacerbated in the Southeast US region due to irregular road networks and low-level beam blockage from trees and complex terrain, partially explaining why multi-Doppler analyses of supercells in the Southeast region are somewhat rare (e.g., Murphy et al. 2013; Knupp et al. 2014). One approach to ameliorate this issue has been the use of airborne radars aboard research aircraft such as the NOAA P-3 flying transects near storms of interest (e.g., Ziegler et al. 2001), enabling high-resolution data collection that may be relatively easy to obtain compared to moving and repositioning ground-based mobile radars. Airborne Doppler radar deployments pose unique challenges relative to their ground-based counterparts, including the aircraft motion as the radar scans and significant main- and side-lobe ground echo returns. Multiple studies over the past two decades have shown that 3-D wind field analyses from airborne radars sufficiently capture the wind field of a supercell (especially from the mid-levels to the surface in previous studies with excessive upper level wind shears that hampered velocity editing), where the standard deviation of horizontal wind error is ~1 m s^{-1} and for vertical wind is 2.5—5 m s^{-1} (Bluestein et al. 1997; Wakimoto et al. 1998; Ziegler et al. 2001; Bluestein 2002).

Sampling target storms from multiple directions offers distinct advantages of increased velocity accuracy, reduced random errors, and covered baselines in analyses that combine data from well-positioned multiple radars in an optimal, over-determined least squares sense (Ray et al. 1978; Ray et al. 1979; Ray et al. 1980; Ray and Sangren 1983; Kessinger et al. 1987; Ziegler et al. 1991; Ziegler 2013b). To assist in improving spatial data resolution while increasing the number of independent, non-colinear radar measurements of targeted storms, the NOAA P-3 has been equipped from 2017 onward with dual solid-state 360° vertically scanning tail Doppler radars (TDRs) whose flat-plate antenna beams are pointed fore and aft at ±20° relative to the unit normal plane of the aircraft fuselage (Jorgensen et al. 2017; Ziegler et al. 2018). The current simultaneous dual-TDR sampling at 20 deg s^{-1} antenna rotation rates, in contrast with the single TDR that rotated at 10 deg s^{-1} prior to 2017, facilitates a four-fold decrease in the along-track sweep gate spacing to enable high-resolution dual-Doppler airflow syntheses of proximate storms.

In addition to the 3-D wind fields that multi-Doppler analyses are able to provide, techniques were developed to extract dynamic and thermodynamic information from these observations (e.g., Gal-Chen 1978; Hane and Scott 1978; Hane et al. 1981; Brandes 1984; Roux 1985; Hane and Ray 1985). However, these retrieval methods have limitations. In microphysical retrievals (e.g., Rutledge and Hobbs 1984; Ziegler 1985, 1988; Marecal et al. 1993) the retrieval is based on solution of a set of 3-D Eulerian-frame parabolic partial differential equations to describe heat and water substance, and this requires prescribed initial and boundary conditions. In dynamical buoyancy retrievals (e.g., Gal-Chen 1978; Hane et al. 1981; Brandes 1984; Roux 1985), wind analysis errors can be amplified significantly by high-order spatial differencing. The high-order vertical spatial differencing of dynamic buoyancy retrievals also results in the lowest analysis levels being used for boundary conditions, thus preventing the dynamic retrieval of near-surface buoyancies which as noted above are critically important for resolving baroclinity impacts of cold pools on supercell vorticity dynamics.

An improved method for studying the thermodynamic details of observed convective storms has been to assimilate the observed radar radial velocities into a convective or cloud-resolving model using the ensemble Kalman filter technique (EnKF) to generate analyses and predictions of complete, internally consistent momentum, thermodynamic, and hydrometeor fields in storms (Snyder and Zhang 2003; Dowell et al. 2004; Marquis et al. 2012; Marquis et al. 2014). While this powerful technique has enabled high-resolution thermodynamic analysis of supercells, it is noted that the ensemble method effectively approximates the individual single-radar analysis variables via localization radius averaging (i.e., smoothing) to predict the individual member and ensemble mean fields.

In contrast, the diabatic Lagrangian analysis (DLA) retrieval method (Ziegler 2013a,b) effectively combines the direct assimilation of multi-radar airflow synthesis fields with the advantages of a simple kinematic cloud model, thus enabling the retrieval of comprehensive 4-D thermodynamic fields in a broadly analogous fashion to retrievals achieved by the more sophisticated ensemble methods, while avoiding several limitations of previous microphysical and dynamical retrieval methods. The DLA solves a system of first-order ordinary differential equations for heat and water substance continuity in a Lagrangian reference frame, applying only a thermodynamic Lagrangian condition from in situ measurements such as proximity soundings to initialize the individual parcel trajectories in the storm environment. The DLA is also able to diagnose values at lateral, upper, and lower boundaries of the retrieval domain via advection and source/sink terms for heat and water substance, enabling it to usefully represent features very near the surface (Ziegler 2013a). The DLA has been validated against model output (Ziegler 2013a) and successfully demonstrated in observed severe local storms (Ziegler 2013b; DiGangi et al. 2016; Chmielewski et al. 2020) and mesoscale convective systems (Miller 2018; Miller et al. 2020).

1.3. Analysis of supercells in the Southeast region

As mentioned previously, there is a dearth of literature on supercells in the Southeast region, both observed and modeled, due to the degree of difficulty in attaining the observational data and the decades-long focus on Central Plains convection. Murphy and Knupp (2013) used a synthetic dual-Doppler technique to study two supercells which passed near a Weather Surveillance Radar-1988 Doppler (WSR-88D) site in Tennessee and showed that supercells in HSLC environments have their updraft maxima below 4km AGL, and not near the storm-top, as in typical Central Plains convection. Knupp et al. (2014) reported dual-Doppler analyses from the 27 April 2011 tornado outbreak, the first analysis documenting a mesoscale convective vortex (MCV) within a northern AL quasi-linear convective system (QLCS) and the second analysis probing the Cullman AL supercell which produced a violent tornado. These results have been reproduced in some of the few modeling studies of HSLC supercells, which demonstrated the importance of dynamic perturbation pressure forces in HSLC updrafts (Sherburn and Parker 2019; Wade and Parker 2021). In a supercell, the low- and mid-level updraft is driven largely by an upward-directed perturbation pressure force that is driven by the large mid-level mesocyclonic vertical vorticity ζ, owing to the approximate inverse relationship between perturbation pressure and enstrophy in pure rotation of the form $\pi' = -\zeta^2$ (Klemp and Rotunno 1983). Once air parcels are lifted above the main updraft maximum and core of the mesocyclone, the direction of the pressure perturbation force reverses to become downward-directed in opposition to thermal buoyancy below the equilibrium level (EL). In most Central Plains supercells, which feature large CAPE, the upward buoyant acceleration dominates this negative dynamic accelerations and the parcel continues to gain updraft speed as it rises higher in the storm. In HSLC supercells, however, due to narrow, skinny CAPE that often results from weak temperature lapse rates (a common feature in southeast severe convective environments), the dynamical acceleration forces remain dominant. As a result, parcel updraft speed slows considerably and can even be fully neutralized in the mid-levels (Wade and Parker 2021). In addition, while a typical Central Plains long-lived supercell features a steady-state updraft, supercells in HSLC environments feature a "pulse-like" evolution with discrete, intense upward pulses superimposed on the broader storm-scale updraft field, resulting in an updraft structure resembling the "weak evolution" scenario described by Foote and Frank (1983) and Wade and Parker (2021). Another notable difference in southeastern supercells is their consistent lack of a strong cold pool. Surface cold pool observations of discrete storms in the southeast reveal that most cold pools were only about ~ 2—3 °C colder than the environment (Wade and Parker 2021). This is of particular interest given the findings described previously that tornado occurrence is more common in Central Plains tornadic supercells if cold pool temperatures are weaker within ~ 2 km of the center of circulation (Markowski et al. 2002).

This thesis features a multi-radar analysis of a tornadic supercell near Monroe, Louisiana (termed the "Monroe supercell") on 6 April 2018. An array of five total radars, comprised of two mobile ground-based research radars, one WSR-88D-equivalent fixed radar, and two airborne radars sampled the supercell for well over an hour at close range. Ground-based research sounding teams in the area and the downward-pointing Compact Raman Lidar (CRL) system on the P-3 aircraft sampled the near-storm thermodynamic environment and provided the initialization of DLA parcel trajectories, enabling a full 4-D kinematic and thermodynamic analysis of the supercell. The evolution of the Monroe supercell and its tornado are evaluated with a particular focus on three questions: (1) what were the origins of low-level rotation for mesocyclogenesis and tornadogenesis? (2) Did the storm feature an SVC, and if so what was the SVC's structure and role?; and 3) How do the broader morphology and evolution of the Monroe supercell compare to previous observed and simulated storms in the Southeast region and HSLC environments? Chapter 2 describes the data and analysis methods, Chapter 3 provides a case overview, Chapter 4 presents analysis results, Chapter 5 presents an analysis of air trajectories, Chapter 6 presents further discussion of results, and Chapter 7 presents a concluding summary of the main findings of the thesis.

Chapter 2: Data and Analysis Methods

2.1. Ground-based fixed and mobile radars

Two ground-based mobile research radars and one fixed radar provided simultaneous, full-volume Doppler observations of the 6-7 April 2018 convection (Table 1). The mobile radars were SMART-R2 (SR2) and SMART-R3 (SR3, formerly SR1), 5-cm wavelength (C-band) radars operated by Dr. Michael Biggerstaff of the University of Oklahoma and his research team. These two mobile radars were positioned in a triangular array with the University of Louisiana-Monroe's 10-cm wavelength (S-band) NEXRAD-equivalent radar located in Monroe, LA (Figure 2). The radar volumes were synchronized at a 5-min interval for the duration of the analysis period (Table 2). These three radars performed scans at 20 tilt angles between 0.8 degrees and 43.0 degrees, each full volume taking approximately 4 minutes to complete. Within each volume, a temporal adjustment algorithm linearly shifted the radar data to analysis time, defined as the nearest minute to the 0.8 degree scan, according to an approximate storm motion vector and assumed inter-scan steady-state morphology as described in Ziegler (2013b).

2.2. NOAA P-3 aircraft

The National Oceanic and Atmospheric Administration (NOAA) P-3 aircraft carried numerous instruments recording radar and in situ thermodynamic data. The P-3 flew eleven consecutive legs transecting the inflow region along the southwest flank of the Monroe Supercell from 2254 UTC (6 April) to 0007 UTC (7 April) at an approximate elevation of 1 km AGL (Figure 2). Each leg was approximately 5 minutes in length, after which the aircraft would reverse course and reposition to maintain a distance of ~10 km from the supercell, a maneuver which took about 3 minutes. Radar data collected during turns were excluded from the analysis due to the distortion caused by the high roll angle of the aircraft combined with potential for small beam navigation errors.

2.2.1. Tail Doppler radars

The P-3 operated two single-polarization 3-cm (X-band) Tail Doppler Radars (TDR) scanning vertically-oriented sweeps every 3 seconds (Table 1). TDR-aft (TAFT) and TDR-fore (TFOR) were oriented at approximately 20 degrees normal to the flight track in the aft and forward direction, respectively (Figure 3). With an average flight speed of about 120 m s^{-1}, the radar scans were slightly helical in shape. Given that the target storm was sampled in 3/4 second, the individual sweeps were essentially instantaneous in time and space. Each volume of data, representing a vertical cross section of the storm, was separated by approximately 360 m of horizontal distance.

Radar data from each P-3 leg was synchronized to the closest 5-minute nominal analysis time utilizing the same spatial-temporal linear interpolation algorithm described in section 2.1 (Table 2). For a few select volumes with no corresponding P-3 leg, radar data of the closest leg was used (Table 2). No leg of radar data was used for more than two consecutive analysis times.

2.2.2. Flight-level in situ measurements

Various instruments aboard the P-3 measured positional and thermodynamic data at flight-level. These instruments recorded data at a frequency of 1 Hz, which corresponds to a 120 m horizonal data spacing (Table 3). Additional thermodynamic variables were derived from these measurements using the relationships from Bolton (1980). Altitude was determined as the average of five separate instruments which measured GPS altitude; all other variables were recorded or derived from data recorded by a single instrument. All thermodynamic variables were passed through a symmetric ramp low-pass filter with a window length of 18Δt to smooth random oscillations prior to in situ data analysis.

2.2.3. Compact Raman Lidar

The Compact Raman Lidar (CRL) is a downward-pointing lidar system mounted on the P-3 (Wang et al. 2016). It measures air temperature, water vapor mixing ratio, and lidar scattering ratio (LSR) with a vertical spacing of 1.2 m and a horizontal spacing of 360 m (i.e., based on a temporal resolution of approximately 3 seconds and an average flight speed of 120 m s^{-1}).

The LSR, the ratio of laser output power to returned power, was used to determine regions where the signal return was too weak to provide accurate thermodynamic measurements. For southeastern US springtime events, an LSR value exceeding 2 was the threshold used to mask potentially untrustworthy data (Zhien Wang, personal communication, 2020). In addition, temperature data within the first 100 m below the P-3 and water vapor mixing ratio above 800 m MSL (~200 m below the P-3) were also masked due to poor data quality in close proximity to the instrument.

The CRL data were analyzed for the first ten of the total eleven legs of the P-3 as it transected the inflow to the Monroe supercell from 2250 UTC through 0001 UTC. Within each leg, vertical gaps in the data caused by the masking of regions with locally higher LSR (likely the result of the P-3 flying over or through boundary layer convective clouds) were hole-filled using a horizontal linear interpolation algorithm. Masked data was only hole-filled if there were non-masked measurements on either side of the hole within a given leg.

A vertical pressure profile of the boundary layer was derived by initializing the hypsometric equation using flight-level measurements (see section 2.2.2), and integrating downward using each individual CRL thermodynamic profile for each leg. These individual vertical pressure profiles were then averaged together within each leg to create the leg-averaged vertical pressure profile. These ten derived vertical pressure profiles of the boundary layer were on average ~2.5 mb higher than the pressure measured by the proximity Gilbert sounding (see section 2.3). From leg to leg, the leg-averaged profiles only varied on the order of 0.5 mb. A random test of thermodynamic calculations using a leg-averaged vertical pressure profile and using the vertical pressure profile measured by the sounding revealed the effect of this ~2.5 mb shift to be negligible (Table 4).

In addition to measured air temperature and water vapor mixing ratio, other thermodynamic variables including potential temperature, virtual potential temperature, dewpoint temperature, and relative humidity were derived from the relationships established in Bolton (1980). These derivations revealed large regions of unmasked data where relative humidity was well in excess of 100% (at times even exceeding 130%, where clouds were not present). It is hypothesized that these non-physical water supersaturations may be the result of low-bias errors within the temperature profile (Zhang Wang, personal communication, 2021). A function was introduced to mask all data gates with non-physical relative humidity, defined by a non-linear function in the boundary layer with a threshold of 90% in the lowest 100 m and 100% at 1 km MSL. While crude, this function enabled us to remove all data gates with unusually cold temperatures that were also suspected as having notable cold temperature errors. Further exploration into the cause of these non-physical relative humidity values or attempts to correct erroneous data was outside the scope of this project.

The CRL provided high resolution near-storm 2-D thermodynamic profile measurements of the inflow boundary layer facing the storm. Although the "proximity" Gilbert sounding was a reasonable approximation of the deep-tropospheric regional-scale thermodynamic environment of the Monroe supercell (see section 4.1), the CRL results enabled slight modifications to the boundary layer thermodynamic profile used in the initialization of air parcels in the diabatic Lagrangian analysis (DLA) that yielded potentially more accurate low-level retrieved fields (see section 2.7).

2.3. Research and operational soundings

Four nearby research soundings were launched by the VORTEXSE-2018 project, including two at Monroe, LA (2030 UTC and 2231 UTC) and two at Gilbert, LA at 2033 UTC and 2234 UTC (Figure 2, Figure 4). These soundings recorded data every 5 seconds (roughly ~30 m vertical spacing within the boundary layer). The 2234 UTC Gilbert sounding was used as the primary proximity sounding for the Monroe supercell due to its location to the southeast of the storm within the broad warm sector, the 2231 UTC Monroe sounding terminating just above 9 km AGL, and Monroe experiencing a likely convective outflow prior to 2231 UTC (see section 4.1) (Figure 4). Data from the Gilbert sounding was linearly interpolated to match the vertical resolution of the CRL measurements (see section 2.2.3), and also used to initialize air parcel thermodynamic variables in the diabatic Lagrangian analysis (DLA, see section 2.7). The lowest 1.5 km AGL of the Gilbert sounding was adjusted for the DLA input to reflect the measurements of the CRL and the Monroe soundings, which featured stronger low-level temperature lapse rates and a higher concentration of water vapor mixing ratio at the surface (see section 4.2). In addition to these four research soundings, operational soundings were launched from the nearby network sites at Shreveport, LA, Little Rock, AK, and Jackson, MS. Table 5 displays the times and locations of the different soundings in this analysis.

2.4. In Situ surface observations

Surface observational data were collected from nine surface stations across central and northern Louisiana and western Mississippi (Figure 2). An Automated Surface Observing System (ASOS) site at Monroe Regional Airport recorded wind speed, wind direction, pressure, air temperature, and dewpoint temperature at 5-minute increments. The other eight stations were Weather-Bureau-Army-Navy (WBAN) sties that recorded air temperature, dewpoint temperature, pressure, and relative humidity at irregular intervals ranging from as short as seven minutes to as long as 50 minutes. For the majority of the analysis period, most stations collected data at approximately 20-minute intervals (Table 7). Potential temperature and virtual potential temperature (along with relative humidity for the ASOS site) were derived using the thermodynamic relationships from Bolton (1980). Water vapor mixing ratio was derived using the official AMS glossary definition.

The surface stations were clustered into two groupings based on latitude, the five stations along or just north of I-20 being classified as “Northern” and the four stations approximately 110 km to the south being classified as “Southern” (Figure 2, Table 10). While some of the Northern stations were close to the Monroe supercell (as close as 10 km in the case of KMLU), these stations were not observing the same open warm sector airmass through which the Monroe supercell moved, due to earlier convection and a cold front moving southward as will be discussed in sections 3 and 4.1. However, analysis of these surface observations still provided useful characterization for the open warm sector on the meso-β scale (20-200 km wavelength).

2.5. Radar Analysis

2.5.1 Radar data editing

A heavily customized Python ARM Radar Toolkit (Py-ART) script was used to perform the bulk of radar editing for all five radars (Biggerstaff et al. 2021; Daniel Stechman, personal communication, 2021). The editing procedure for the three ground-based radars (KULM, SR2, and SR3) was different from the procedure for the two airborne radars (TAFT and TFOR) due to the different technical specifications and scanning techniques of the two radar types. After the conclusion of bulk editing via the Py-ART script, all radar data were manually inspected and additional dealiasing, noise filtering, and ground clutter removal (for the airborne radars only) was performed as necessary in the National Center for Atmospheric Research (NCAR) SOLOII software.

A 3-D spatial statistical clutter detection map was generated for each of the three ground-based radars using a series of pre-storm clear-air scans, and applied prior to the automated Py-ART editing to mask complex patterns of ground echoes near the radar sites. The two mobile radars SR2 and SR3 also had a rotation correction applied using SOLOII of 0.4 degrees and -4.5 degrees respectively (i.e., positive representing a clockwise rotation angle in SOLOII). The radar data were then fed into the Py-ART script, which performed noise filtering, despeckling, and dealiasing using a 4DD region-based algorithm and the Gilbert sounding wind profile (see section 2.3).

Prior to bulk editing of the TDR data, aircraft motion was removed from velocity data using SOLOII. The Py-ART script then performed noise filtering, de-spoking, and detection and correction of dual-PRF errors in the TDR sweeps. Dealiasing was not necessary for the airborne radars in the present storm case due to their large effective Nyquist velocity value. Particular care was taken in both the automated and manual editing procedures to remove main- and sidelobe ground clutter contamination, while also preserving near-surface meteorological observations.

2.5.2. Single-radar objective analysis and grid domains

A spatial single-radar analysis based on a one-pass application of a 3-dimensional Barnes interpolation scheme (Barnes 1964; Majcen et al. 2008; Ziegler 2013b) was employed to map all single-radar data to the analysis grid domains in northeastern Louisiana. The spatial Barnes weighting function takes the form (Majcen et al. 2008)

$$\omega_{jk,n} = exp\left(-\frac{{r_{jk}}^2}{\kappa_0 \gamma^{n-1}}\right), \qquad (1)$$

where r_{jk} (km) is the distance from the *j*th grid point to the *k*th radar gate measurement, *n* is the pass number ($n = 1, N$), κ_0 (km^2) is the smoothing parameter of the first pass, and $\gamma = 0.3$ is the convergence parameter (Koch et al. 1983). All analysis domains have a spatial grid separation of 250 m x 250 m x 250 m. This grid spacing corresponds to a longest unresolvable wavelength (i.e., Nyquist wavelength) of 500 m.

A novel feature of the present thesis is the application of three different analysis grid domains (i.e., the "Big Grid", "Nested Grid", and "Fine Grid") under the principle that employing progressively smaller, nested domains with lateral boundaries closer to the networked radars allows a commensurately decreasing κ value that maintains effective resolution of the coarsest (longest-range) radar observations in each nested domain (Table 8). The "Big Grid" one-pass smoothing parameter $\kappa_0 = \kappa_{BG}$ (km^2) has been chosen to produce the smallest degree of smoothing necessary to fully resolve the farthest (i.e., coarsest) radar data in that domain (i.e., SR2). The “Nested Grid” analysis effectively assumes $\kappa_{NG} = \kappa_{BG}\gamma$ (km^2), while the “Fine Grid” analysis assumes $\kappa_{FG} \approx \kappa_{NG}\gamma = \kappa_{BG}\gamma^2$ (km^2). The latter κ_{FG} value has been slightly increased to guarantee smoothly varying fields spanning the “Fine Grid” analysis domain (Table 8). Thus relative to the "Big Grid" analysis with $\kappa_0 = \kappa_{BG} = 0.44$ (Table 8), the "Nested-Grid" one-pass analysis approximates a 2-pass Barnes analysis while the "Fine-Grid" analysis approximates a 3-

pass Barnes analysis. Due to SR2 and SR3 being located at greater range from the Monroe supercell (i.e., on the order of ~ 40 km), only the relatively close-range (i.e., ~ 20 km) TAFT, TFOR, and KULM data were objectively analyzed on the “Fine Grid”. Within each radar volume, a temporal adjustment algorithm linearly shifted the radar data in time-to-space relative to the analysis time, defined as the nearest minute to the 0.8 degree scan, according to an estimated storm motion vector and assumed inter-scan steady-state morphology as described in Ziegler (2013b).

A second novel feature of the present thesis is to expand the overall single-radar analysis areal and volume coverage of the broader mesoscale storm environment by merging the “Fine Grid” analysis within the “Nested Grid” analysis to produce a “Merged Nested Grid” analysis. By analogy to conventional nested-grid cloud-mesoscale models, this nested radar analysis procedure takes advantage of the finescale tornadic Monroe supercell analysis within the broader coverage of the less well resolved field of non-severe mesoscale convection in the Monroe supercell's meso-β scale environment. The KULM, TAFT, and TFOR “Fine Grid” objective analyses have been inserted within their respective “Nested Grid” analyses at each analysis time, with a "sponge zone" smoothing function applied along and near the fine grid lateral boundaries to locally preserve spatial continuity.

2.5.3. Multiple-Doppler velocity and reflectivity synthesis

An “over-determined dual-Doppler" radar synthesis algorithm was applied to synthesize the gridded single-radar objective analyses from the multiple radars for the domains defined in Table 8 (Ray et al. 1980; Ray and Sangren 1983; Kessinger et al. 1987; Ziegler 2013b). The radar synthesis follows a multi-step algorithm:

(1) A set of two linear normal equations (relating the variable u, v, and w Cartesian vector wind components to input multi-radar radial velocities and a derived precipitation fallspeed V_t) and the anelastic mass continuity equation are integrated downward from w = 0 at storm top in each column using an iterative procedure at each level to derive the u, v, and w components at all gridpoints in each column where horizontal divergence can be calculated (Kessinger et al. 1987; Ziegler 2013b);

(2) Gridpoints with missing wind components are hole-filled employing a horizontal filling-smoothing procedure, in which missing u and v components are initially filled from a gridded environmental sounding, missing gridpoint w component values are initially set to zero, and multiple passes of a 2-D horizontal filter are applied to the missing data points using the fixed radar-synthesized vector wind components as lateral boundary conditions;

(3) An O'Brien (1970) adjustment via anelastic mass continuity is applied to the w-component (i.e., via vertical mass flux) in each column by constraining the integrated divergence to vanish applying w = 0 kinematic lower and upper boundary conditions at the surface and 14 km AGL, after which the adjusted 3-D w-component field is lightly filtered horizontally;

(4) A 3-D variational adjustment of the u, v, and w Cartesian wind components is performed by applying anelastic mass continuity as a strong constraint following Eqs. (16)-(19) of Ray et al. (1978), where it is noted that the 3-D adjustment acts over the full 3-D domain proceeding from steps (1)-(3) above.

The reflectivity field analysis is determined from the maximum individual reflectivity value at each grid point drawn from the contributing single-radar objective analyses. Availability of objectively analyzed S-band gridded reflectivity mitigates potential attenuation effects on the reflectivity field from the X and C band radars. The bulk fallspeed V_t in step #1 is derived from an empirical function of reflectivity.

The above step #1 of the radar synthesis algorithm automatically excludes any specified input dual- or triple-Doppler pairings at a given analysis time if any given pairing is either judged to have poor geometry (e.g., two radars separated by a very long baseline, or three radars aligned around common baselines) or is found to produce non-physical velocity artifacts (Table 9). The occurrence of significantly different vertical beamwidths and corresponding vertical gate spacings of different radars (Table 1) at a given grid point was particularly problematic in combinations of one of the SRs with either KULM or one of the TDRs at far range within the developing mesoscale convective system (MCS). The latter issue was frequently exacerbated for low elevation radar sweeps where there was significant ambient vertical wind shear (see section 3), which is unsurprising given the prevalence of high-shear environments in Southeast severe weather cases. In the latter instances, either the SR's or TDR's coarse beam at far range would beam-average the radial component of the wind shear over a deeper layer than the characteristic shear depth. Since the narrower KULM pencil beam would more accurately measure the low-level winds at range, dual-Doppler radial velocity combinations at range from radars with these differing beamwidths could often lead to non-physical results.

In summary, the optimal synthesis for analyzing the small-scale features of the Monroe supercell was the combination of the “Fine Grid” analyses of KULM, TAFT, and TFOR nested within the “Nested Grid” analyses of KULM, TAFT, TFOR, SR2, and SR3 via the merged fields stored in the "Merged Nested Grid" analyses. A range and elevation restriction was placed on SR2 and SR3 such that their coarser radar data was not synthesized below 2km AGL in the vicinity of the Monroe Supercell, in order to preserve the highly-detailed synthesis of the low-level mesocyclone (Tables 10-11). Above 2 km, the range effects of the SR's coarse beam width discussed previously were minimized by the reduced middle level vertical wind shears (Figure 4). Derived kinematic fields such as vertical vorticity, horizontal streamwise and anti-streamwise vorticity, asymptotic contraction and fluid trapping (Cohen and Schultz 2005), and 3-D deformation were calculated from the 3-dimensional wind fields.

2.6. Radar-derived hodographs

Hodographs of the multi-radar synthesized storm-inflow wind field were derived at each analysis height for each analysis time in the vicinity of the Monroe supercell. A 15 km x 15 km domain within the Merged Nested Grid domain (see section 2.5) was centered on the southward-extending anvil of the Monroe supercell, positioned so as to exclude the mesocyclone, the FFD, and the RFD. Within this domain, all wind vectors derived from the synthesis of two or more radars and co-located with reflectivity between 15 and 30 dBZ were averaged together at each analysis height to approximate the near-environmental wind profile. The reflectivity threshold was chosen to preclude the assimilation of winds within the core of the storm that are significantly altered by storm-scale processes. Both 0—1 km and 0—3 km Storm Relative Helicity (SRH) were calculated from each of these derived hodographs. Table 6 shows statistics calculated from the differences between the P-3 measured wind at 1 km AGL (see section 2.2.2) with both the 1 km Gilbert sounding measured wind and the 1 km radar-derived wind. The wind profiles were derived on 15 km x 15 km and 30 km x 30 km meshes within the Fine Grid domain (see section 2.5) The larger mesh included the Monroe supercell mesocyclone, while the smaller mesh intentionally did not and was centered on the Monroe supercell anvil.

2.7. Diabatic Lagrangian analysis

Diabatic Lagrangian analysis (DLA) is a kinematic thermal-microphysical continuity retrieval of heat and water substance based on integration along Lagrangian trajectories that proceeds from a series of input time-varying 3-dimensional wind and reflectivity analyses (Ziegler 2013a,b). The DLA builds upon an earlier thermal-microphysical continuity retrieval method based on a solution of a parabolic system of conservation equations for heat and water substance (e.g., Ziegler 1985; Ziegler 1988) as well as previous iterations of the DLA itself (DiGangi et al. 2016; Miller 2018; Chmielewski et al. 2020; Miller et al. 2020). Diagnosed fields include the mixing ratios of rain, graupel/hail, and ice. Output fields include potential temperature, water vapor mixing ratio, cloud water, cloud ice, and derived variables such as temperature and virtual potential temperature, along with others.

The DLA grid domain was nested within the "Merged Grid" radar analysis domain (see section 2.5) and centered on the Monroe supercell inflow and mesocyclone. Airflow, reflectivity, vertical vorticity, and a bulk mixing coefficient based on the 3-D airflow deformation were linearly interpolated in time and space from the 5-minute interval "Merged Grid" analyses to the Lagrangian point following each trajectory. Backward 3-dimensional trajectories were computed with a 20 s timestep from all gridpoints within the DLA domain back into their remote inflow environments. All trajectories found to originate within the convection-free inflow environment were then initialized with the thermodynamics of a parcel at that particular height. Above 1.5 km, the environmental thermodynamic profile was prescribed directly from the Gilbert sounding (see section 2.3). From 0 – 1 km, a nonlinear parametric thermodynamic profile was constructed for water vapor mixing ratio and potential temperature and fit to the boundary layer thermodynamic profiles measured by the proximity sounding, the 2234 UTC Monroe sounding, the CRL measurements, and in-situ measurements from surface stations and the P-3 (see section 2.2, 2.4). The thermodynamic variables at the 1.25 km level were derived by averaging the 1 km CRL-derived value and the 1.5 km Gilbert sounding value. This hybrid thermodynamic profile was used to thermodynamically initialize the DLA trajectories. From these two conserved quantities and the vertical pressure profile measured in the Gilbert sounding, parametrically-derived boundary layer profiles were calculated for temperature, dewpoint temperature, virtual potential temperature, and relative humidity for comparison with the CRL (see section 4.2).

Following trajectory initialization, a system of ordinary differential heat and water substance continuity equations were integrated forward in time along each trajectory path. Using airflow and reflectivity, calculations using bulk parameterized microphysical terms diagnose snow, graupel/hail, and rain mixing ratios as well as parameterized rates of collection/riming, freezing/melting, and deposition/sublimation at every Lagrangian point along each trajectory. Forward integration of all trajectories back to their originating gridpoint followed by a gather operation yields the 3-dimensional thermodynamic fields at each analysis time (Ziegler 2013a,b). These trajectories and some of their intrinsic values (i.e., position, vertical velocity, etc.) at each 20 s increment are output by the DLA for analysis.

Chapter 3: Case Overview

The 6-7 April 2018 VORTEX-SE deployment (IOP 4) was a mission to sample a MCS that was expected to develop over northeastern Louisiana in the late evening, with the possibility of also sampling supercells south of this developing linear convection in the late afternoon should they develop. Multiple supercells formed in the late afternoon in the open warm sector in northeastern Louisiana, including one tornadic supercell (the “Monroe supercell”) which will be the focus of this thesis. Later, a southward-moving MCS formed in the early evening along a weak cold front and supercell cold pools near the Louisiana-Arkansas border.

A deep upper-level trough was located over the Great Lakes region, with its associated surface low dropping a cold front across the lower Midwest and into Oklahoma and the Texas panhandle (Figure 5). A subtle shortwave passed over the TX-LA-AR region at 500mb, providing modest upper-level support for convection as per Quasi-Geostrophic theory. A lee cyclone was present in north central Texas with its attendant dryline extending into central/south Texas. The warm front associated with the lee cyclone moved through Louisiana during the morning of 6 April 2018 before stalling into a stationary front along the Louisiana-Arkansas border. Southerly surface winds south of this front enabled moisture advection from the Gulf of Mexico. A modest Elevated Mixed Layer (EML) (see Figure 4, Figure 6, and Figure 7) advected from the west/southwest at 700mb brought a short layer of steep mid-level lapse rates which helped prime the atmosphere with ~2000 JKg^{-1} of Mixed Layer (ML) CAPE by the afternoon in the open warm sector in east Texas and Louisiana. While this event features more than double the MLCAPE of a HSLC event (e.g., Wade and Parker 2021), the vertical thermodynamic profile was markedly different from classic central plains supercell events due to the entire profile being well saturated and featuring weak temperature lapse rates aside from the short EML (Figure 4,

Figure 6, and Figure 7). The hodographs from both the 2234 UTC Gilbert sounding and the 2231 UTC Monroe sounding depict veering winds in the low levels, albeit with minimal curvature below 1 km (Figure 4). The Gilbert sounding in particular depicts a long low-level hodograph and strong north-northwesterly upper-level winds. These upper-level winds are reflected by the south-southeastward extending anvils from the Monroe Supercell and other isolated storms in the area (Figure 9). This environmental profile will affect how our supercell evolves (see section 4.4), and it is unique from most other traditional supercell studies, both observational and modeled, which often feature characteristics common to the Central Plains such as strong low-level curvature, west-southwesterly winds aloft, steep temperature lapse rates above the boundary layer, and dry mid and upper levels.

The Storm Prediction Center (SPC) issued an Enhanced risk (level 3 of 5) for severe thunderstorms from east Texas through north Louisiana and into western Mississippi for this event (Figure 8). The primary anticipated risks were severe winds associated with the MCS that would develop along the southward-moving convectively-reinforced cold front in the early overnight hours and significant severe hail associated with strong supercell updrafts along the dryline in central/east Texas, though the forecast noted a conditional tornado threat associated with any semi-discrete storms due to strong low-level shear and sufficient hodograph curvature in northern Louisiana.

Throughout the day, surface heating and continual moisture advection enabled a moist boundary layer to mix and, by late afternoon, break through the cap associated with the EML. Our storm of interest, the Monroe supercell, initiated at approximately 2220 UTC ~20 km south of Ruston, LA, just to the south of another mature supercell. At 2230 UTC, numerous supercells were evident in northeastern Louisiana (Figure 9a). While there were numerous tornadoes during this event, the Monroe supercell was the only supercell in this region to produce a tornado. At 2236 UTC, the P-3, which had been sampling a weak line of convection over southern Arkansas, began its traverse towards these supercells south of Monroe.

By 2300 UTC, the Monroe supercell was the dominant storm in the region and its inflow had uninhibited access to the open warm sector. The other supercells present thirty minutes prior had either merged together in the initial forming of the developing MCS, or were weakening likely due to their warm inflow being cut off by the outflow of nearby storms (such as the weakening supercell to the north of the Monroe supercell) (Figure 9b).

At 2330 UTC, The Monroe supercell remained a fully mature, isolated supercell (Figure 9c). Ten minutes later, at 2340 UTC (Figure 9d), it produced an EF-0 tornado to the southeast of Monroe, LA that lasted 13 minutes and traveled 12.63km with a maximum path width of 50 yards (NOAA NCEI Storm Events Database) (Figure 10). Due to this area being forested and lightly-populated, the NWS survey team noted only four EF-0 damage points assessed along the track. In addition, at 2355 UTC, two minutes after the end of the surveyed EF-0 tornado, the survey team assessed an EF-1 damage point slightly off-track from the EF-0 tornado.

By 0000 UTC, the structure of the Monroe supercell had degraded as it began to interact with convection to its north and east (Figure 9e). By 0030 UTC, the Monroe supercell was completely absorbed and the MCS had matured as it pushed southward (Figure 9f).

Chapter 4: Results

4.1. Surface observations

Both the northern and southern suite of surface stations were within the warm sector during the afternoon of 6 April 2018 prior to 2100 UTC (with the exception of KBQP, the furthest-north station), as indicated by their temperature timeseries (Figure 11). There was notable temperature consistency between the northern and southern suite of stations, despite the southern stations being approximately 110 km to the south. Water vapor mixing ratio observed by the southern stations were up to 2 g kg^{-1} higher than the northern stations, likely a result of their proximity to the Gulf of Mexico – the source of boundary layer moisture (see section 3).

Evident throughout the timeseries of the northern suite were a number of changes in airmass characteristics (Figure 11). KMLU, the station closest to the Monroe supercell, experienced three distinct airmasses throughout the afternoon. Just after 2100 UTC, KMLU observed a ~2 °C drop in temperature associated with a 1 g kg^{-1} *increase* in water vapor mixing ratio. The other northern stations (aside from KBQP) experienced similar, yet less notable, changes slightly earlier in the afternoon from KMLU. Wind data from KMLU reveals no change in speed or direction at this time (Figure 12), suggesting that this airmass may have been remnant convective outflows advected to the station by storms to the south-southeast of these stations. A second airmass passage at KMLU took place just after 2130 UTC, featuring a sudden drop in both temperature (~2 °C in five minutes) and water vapor mixing ratio (~2 g kg^{-1} in five minutes) (Figure 11). The KMLU wind data revealed no significant changes in magnitude or direction at that time (Figure 12), again suggesting that convective outflows may be responsible. None of the other northern stations experienced a similar airmass passage until the cold front passed later in the afternoon.

Although lacking a distinct change in temperature or water vapor mixing ratio, a shift from southerly to northeasterly wind and a gradual increase in wind magnitude afterwards at KMLU suggests the cold front arrived at Monroe at 2250 UTC (Figure 12). Based on temperature and water vapor mixing ratio drops at the other northern stations down to similar values as KMLU, KRSN and KTVR saw the passage of the cold front between 2300 UTC and 2315 UTC, and KVKS, the furthest east in the northern suite, saw the cold front pass around 2345 UTC (Figure 11). The southern suite of stations, while seeing a gradual decrease in temperature consistent with the diurnal cycle, did not experience the passage of the cold front during the period analyzed.

The additional measured and derived thermodynamic variables for the northern and southern suite of surface stations are shown in Figure 13. These display similar patterns as those described above. While the southern suite of surface stations remained within the open warm sector throughout the Monroe supercell analysis period, these stations were at least 80—100 km from the storm, and therefore we did not consider their measurements as an accurate representation of the near-storm inflow environment (although they do indicate broad homogeneity in the warm sector). The northern suite of surface stations, despite being closer to the supercell, experienced not only the passage of advected convective outflows throughout the afternoon but also the passage of the southward-sagging cold front during the early portion of the Monroe supercell analysis period. Therefore, these stations were unable to provide us an independent measurement of the near-storm inflow environment. However, despite the limitations of the surface observation network, these observations, along with the Gilbert and Monroe soundings, were able to provide us with a basis for evaluating the accuracy of the CRL measurements of the near-storm inflow environment (see section 4.2)

4.2. CRL profile measurements

Figure 14 presents the CRL measurements for the first ten legs, with red hatching indicating regions of non-physical relative humidity which were masked (see section 2.2.3). The majority of masking relating to excessive non-physical water supersaturation was in the lowest 400 m AGL, although large regions at higher elevations also required masking, particularly in the latter legs. Leg-averaged vertical profiles were not calculated for legs 9 and 10 due to the large amount of masking throughout them.

The temperature and water vapor mixing ratio measurements show broad homogeneity above 500 m AGL spatially and temporally (Figure 15). Below 500 m AGL, however, the profiles demonstrated considerable fluctuations both between adjacent legs and within individual legs, on the order of 5 °C in temperature and 2 g kg^{-1} in water vapor mixing ratio. Some of these fluctuations may be the result of either evolutions of the boundary layer through time or the CRL sampling a different portion of the non-homogeneous boundary layer as the P-3 tracks along the moving storm. Within an individual leg, fluctuations may be the result of the CRL fully transecting the inflow region and crossing into a region of the boundary layer which was either less affected by storm-scale processes or influenced by the supercell's outflow. We hypothesize that the high-magnitude fluctuations seen in Figure 15 were the result a combination of heterogeneities within the lower boundary layer and storm-scale processes influencing the inflow sector. Determining how much of a role these two factors played in modifying the lower boundary layer was outside the scope of this project.

The boundary layer measured by the CRL was broadly stable, with virtual potential temperature (θ_v) increasing with height (Figure 15). However for seven of the ten legs, warm pockets of θ_v matching or exceeding the values seen at the top of the profiles were present in the lowest 500 m AGL. These warm pockets represent absolutely unstable air, and thus potentially small updrafts, within the boundary layer. The lack of a consistent warm θ_v pocket despite the CRL transecting roughly similar regions of the storm-relative inflow on each leg suggest that these features may be small and fast-evolving, or they may be a function of the local boundary layer rather than a storm-scale process. However, it is notable that the most intense pockets of low-level boundary layer updraft were from 2320 UTC through 2345 UTC. This time range coincided with the Monroe Supercell intensifying leading up to it producing an EF-0 tornado beginning at 2340 UTC (see section 4.4.3). Whether the intensification of the Monroe supercell was the cause or result of these lower boundary layer updrafts in the inflow region or vice versa is unclear, and outside the scope of this project.

The CRL profiles created from averaging together each of the first eight legs were compared to the Gilbert proximity sounding, two Monroe soundings, surface station observations (see section 4.1), and measurements from in situ instruments aboard the P-3 (Figure 16). The effects of the shallow surface outflow, seen in the KMLU surface observations (Figure 11), were seen in the lowest 100 m AGL of the 2231 UTC Monroe sounding. In the upper boundary layer, the CRL profiles were similar in both magnitude and lapse rate to both the 2231 UTC Monroe sounding and 2234 UTC Gilbert sounding. However, both the CRL profiles and the Monroe soundings, the 2234 UTC sounding in particular, diverge significantly from the Gilbert sounding in the lowest 400 m AGL. The CRL profiles and Monroe soundings depict steep lapse rates in both temperature and water vapor mixing ratio in the lowest 400 m, similar to a superadiabatic surface contact layer. This results in the near-surface CRL-measured temperature and water vapor mixing ratio being ~2 °C warmer and 1 g kg^{-1} higher, respectively, than the Gilbert sounding, but very similar to the 2231 UTC Monroe sounding, the shallow surface cold pool notwithstanding. The consistency between the CRL measurements and both Monroe soundings, both in terms of magnitudes and lapse rates, and excluding the shallow surface cold pool at 2231 UTC, provide confidence that while the Gilbert sounding may our proximity sounding, the CRL measurements of the inflow boundary layer were accurate.

A modified single CRL profile has been created utilizing a qualitative non-linear best-fit function which incorporates the multi-leg CRL profiles and P-3 in situ measurements while converging with the Gilbert sounding above 1 km AGL. The equation for modeling the vertical profile of thermodynamic variable $\phi(z)$ in the lowest 1 km takes the form

$$\phi(z) = \phi_{sfc} + \left(\frac{\Delta\phi}{\Delta z}\right)_{1\,km} z + \Delta\phi_{sfc} e^{-(z/z_0)}, \tag{2}$$

where z is height (m AGL), ϕ_{sfc} is the linear profile function value at the surface, $\left(\frac{\Delta\phi}{\Delta z}\right)_{1\,km}$ is the vertical gradient of the linear profile function between the surface and 1 km AGL, $\Delta\phi_{sfc}$ is the excess surface value relative to ϕ_{sfc}, z_0 (m) is the e-folding vertical scale of the asymptotic inverse-exponential deviation from the linear profile, and Δz = 1000 m. The modified boundary layer profiles (i.e., the thick red dashed curves in Figure 15) obtained by applying Eq. (2) to θ (K) and q_v (g kg^{-1}) are used in the DLA's environmental sounding (see section 2.7). Of particular note with this CRL-modified profile is the ~2 K increase of θ_v (K) near the surface within the dry convectively-unstable near-surface layer, which was observed in the 2030 UTC Monroe sounding and many of the CRL leg profiles but not evident in the Gilbert sounding.

4.3. Radar-analyzed near-inflow environmental hodographs

Radar-analyzed hodographs were produced at every analysis time during the Monroe Supercell Analysis Period. Each hodograph was similar, and so only one example, the 2340 UTC hodograph, is shown compared to the hodographs from the Gilbert proximity sounding and two

Monroe soundings (Figure 17). The general hodograph shape and intensity – southerly low-level winds which turn westerly in the mid-levels (2—5km AGL) and northwesterly aloft – were similar among all hodographs, and there was remarkable agreement in mid-level speed and direction. However, notable differences, both between the three observed hodographs and compared to the radar-analyzed hodograph, were evident in the low and upper levels.

The most significant difference among the hodographs was in the lowest 1 km AGL. Both Monroe soundings depict relatively weak southwesterly winds at the surface which increase in speed with height before eventually veering above 2 km AGL. Their measured surface wind is consistent with the measured wind at KESF at 2340 UTC (~130 km south of Monroe), but they are 5—10 m s^{-1} slower and more westerly than the P-3 in situ measured wind at 1 km AGL at 2340 UTC. Meanwhile, both the Gilbert sounding and radar-analyzed sounding match well with the P-3 measured wind, but their surface wind was significantly faster and more southerly than the KESF measurement and the Monroe soundings. Of all three measured hodographs and the radar-analyzed hodograph at each analysis time, the radar-analyzed hodographs on average had the lowest mean difference and standard deviation of difference compared to the P-3 measurements at ~1 km AGL. This result is unsurprising considering that the radar-analyzed hodographs evolve as the wind field measured by the P-3 evolves, while the measured hodographs are only representative of conditions at the launch location and time. However, the consistency between the radar-analyzed hodographs and the independent P-3 measurement at 1 km AGL provide confidence in the methodology used to create the radar-analyzed hodographs.

The radar-analyzed hodograph in the lowest 1 km AGL was significantly shorter than the measured soundings. This may be an artificial result of the radar analysis under-sampling surface winds: Since there were no true surface winds measured by any of the radars, the analysis used an extrapolation function to provide the surface wind analysis. This necessary procedure may therefore have resulted in a wind field which understates the significant low-level wind shear present in this environment. The effects of the decreased low-level shear in the radar-analyzed hodographs were evident in lowered 0—1 km and 0—3 km Storm-Relative Helicity (SRH) derived from the radar-analyzed hodographs (Figure 18). While calculated 0—1 km SRH was ~100 $m^2 s^{-2}$ lower than that from the Gilbert sounding, the amount of SRH was still sufficient for a supercell and tornado to develop within this environment even if the radar-analyzed hodographs could be validated as perfectly accurate at the surface.

While all hodographs matched well in the mid-levels, above 6 km AGL the hodographs diverged (Figure 17). The 2030 UTC Monroe hodograph depicted primarily west-southwesterly winds aloft, which did not align with the southward-pointing anvil of the Monroe Supercell (see section 4.4). The 2231 UTC Monroe hodograph maintained a west-northwesterly component aloft, but featured relatively weak winds (it is noted again that this sounding terminated around 10 km AGL). The 2234 UTC Gilbert hodograph most closely aligned with all of the radar-analyzed hodographs, featuring strong northwesterly wind aloft. On average, the radar-analyzed hodographs tended to have a stronger northerly component to them, particularly from 2320 UTC onward. Broadly speaking, the Gilbert hodograph provided a reasonable approximation of the radar-analyzed hodographs and compared much more favorably to it than either of the Monroe hodographs did. Although the boundary layer thermodynamics of the Monroe soundings were more closely aligned with the CRL measurements than the Gilbert sounding (see section 4.2), the Monroe hodographs are hypothesized to have been perturbed by the proximate upstream supercell storms (i.e., the Monroe supercell and the neighboring supercell to its north).

4.4. Radar and DLA results

This section contains the results of the Merged Nested grid radar analysis and DLA of the Monroe tornadic supercell during the period 2255 UTC – 0005 UTC. Three particularly interesting sub-periods of the Monroe supercell’s evolution will be focused on as defined by their prominent feature: The Early Transient Mesovortex (2305 UTC – 2320 UTC), Tornadogenesis (2335 UTC – 2345 UTC), and Supercell Decay (2350 UTC – 0000 UTC). Following a brief overview of storm-scale DLA-retrieved thermal and hydrometeor fields at 2340 UTC, subsections 4.4.2 – 4.4.4 will detail the supercell's kinematic and thermodynamic structure for the three periods of interest. Finally, subsection 4.4.5 will focus on results pertaining to the identification and classification of storm-scale boundaries and their potential role in vorticity generation.

4.4.1. Storm-scale thermal and hydrometeor fields at 2340 UTC

The suite of DLA-retrieved hydrometeor mixing ratios through the full depth of the Monroe supercell at 2340 UTC (Figure 19) show meager amounts of graupel/hail aloft in the storm, with nearly complete mass melting and minimal amounts reaching the surface in the FFD. This limited graupel/hail growth ultimately led to lesser rainfall rates, as indicated by the rainwater mixing ratio (Figure 19e). Cloud water mixing ratio and perturbation virtual potential temperature $\theta_v{}'$ (Figure 19a and 19g) show strong alignment to the main supercell updraft in location, width, and depth. The warm bubble of $\theta_v{}'$ in the updraft is the result of rising air cooling at the moist adiabatic lapse rate, and remaining positively buoyant as water is condensed out of these parcels (as evidenced by the high cloud water mixing ratio). The warmer $\theta_v{}'$ ends at a height of ~5.5 km AGL, coincident with the weakening of the updraft with height. Further discussion of the updraft structure is in section 6.2.

4.4.2. Early transient mesovortex (2305 – 2320 UTC)

The Early Transient Mesovortex was a short-lived low-level mesovortex which developed ~2 km south of the Monroe supercell's hook echo. It likely reached its peak intensity, in terms of vertical vorticity, low-level vertical velocity, and low-level reflectivity, between 2310 UTC and 2315 UTC. The feature would quickly dissipate and, despite a brief corridor exceeding 15 dBZ extending from the feature into the mid-level reflectivity of the Monroe supercell's Bounded Weak Echo Region (BWER), would never appear to fully connect with the Monroe supercell updraft. During the leg of the P-3 which coincided with the time between the 2310 UTC and 2315 UTC analysis times, the pilots of the P-3 reported seeing a tornado. Since the Early Transient Mesovortex peaked in intensity during that time range, and it featured the only mesocyclone-strength low-level vertical vorticity, we hypothesize that the feature that the pilots reported was associated with the Early Transient Mesovortex. Since no damage report, survey, or other visual evidence exists to support their report, we will have to assume that there was no tornado (hence why we term it "Early Transient Mesovortex"). While this feature will not be discussed as a tornado, we acknowledge that it was possible that the Early Transient Mesovortex produced a brief, weak tornado that did not produce enough noticeable damage to be reported, or only produced damage in an isolated portion of forest that no one noticed.

At 2305 UTC, the Monroe supercell had the reflectivity appearance of a classic supercell (Figure 20), with a moderately high-reflectivity hook echo at (49.5 km E, 40 km N) extending to the south of the narrow westward extension from the high-reflectivity precipitation core (Figure 20). The supercell's anvil extended to the far south edge of the domain due to strong N-NE winds aloft, indicated by both the Gilbert proximity sounding hodograph and a hodograph calculated from the multi-radar derived wind field (see section 4.3). Despite the relatively classic reflectivity appearance, the Monroe supercell at this time did not feature a well-organized low-level updraft or low-level mesocyclone. Along the northern edge of the inflow notch (53 km E, 42 km N on Figure 20) was a notable downdraft in a location typically most associated with updraft, and the hook echo itself featured minimal updraft. Low-level streamwise vorticity in the vicinity of the hook echo was minimal, aside from a small patch of enhanced streamwise vorticity co-located with the previously noted downdraft, although crosswise vorticity was enhanced throughout the near-storm inflow sector.

At 2310 UTC (Figure 21), the Monroe supercell maintained its organized reflectivity appearance despite the continued absence of an organized low-level updraft or low-level mesocyclone noted previously at 2305 UTC. A DLA run at this time enabled the identification of a weak, developing RFGF around the hook echo and a FFCB extending from the northern edge of the inflow notch to the southeast along the edge of the anvil. The cold pool of the supercell, as represented by θ_v', was focused on the eastern portion of the storm and extended south down the anvil. This cold pool was closely associated with relatively high concentrations of surface rainwater (see section 4.4.5) Southeasterly storm-relative winds advected this diabatically-cooled air to the northwest, away from the hook echo.

The supercell hook echo continued to lack a low-level updraft or low-level mesocyclone, and the inflow notch was, similar to 2305 UTC, dominated by a low-level downdraft. The thermodynamic effect of this downdraft can be seen in the extensive warm pocket in the 500 m θ_v' field in the inflow notch and hook echo region. Two kilometers south of the hook (54 km E, 38 km N on Figure 21), evidence of the Early Transient Mesovortex was in the form of a weak near-surface reflectivity echo collocated with weak vertical vorticity and a small, but notable, low-level updraft.

By 2315 UTC (Figure 22), the reflectivity presentation of the Monroe supercell had degraded significantly. The southward-extending hook echo had retreated to just a stub-like appendage on the western edge of the storm. There continued to be no evidence of a low-level mesocyclone. However, there were some indications of weak low-level updrafts (~5 m s^{-1}) in the (much less pronounced) inflow notch, where a low-level downdraft had previously dominated (see Figure 21).

The Early Transient Mesovortex feature identified at 2310 UTC developed near-surface vertical vorticity exceeding mesocyclone strength, coupled anticyclonic vertical vorticity and an isolated surface reflectivity blob of 30 dBZ. However, the Early Transient Mesovortex no longer featured a low-level updraft (and two weak *downdrafts* were present adjacent to its reflectivity enhancement). Without low-level updraft support, lessening of vertical vorticity and decreasing of reflectivity would be expected, and indeed that is what was seen at 2320 UTC (Figure 23). Therefore, we conclude that the Early Transient Mesovortex achieved its peak intensity during the five-minutes between the 2310 UTC and 2315 UTC analysis times.

The overall reflectivity presentation of the Monroe Supercell remained unimpressive at 2320 UTC (Figure 23), with its short southern stub of a “hook echo” and negligible low-level mesocyclone. The modest updraft within the inflow notch expanded marginally from the previous analysis time, but more notable was the expansion of weak (2.5 m s^{-1}) updraft throughout the near-storm inflow sector. A region of enhanced streamwise vorticity was noted within this inflow sector (63 km E, 42 km N on Figure 23), a feature that was not present at the earlier analysis times.

The Early Transient Mesovortex, despite featuring a notably strong, but small, low-level updraft, had its reflectivity shrink in magnitude and size and it no longer featured notable low-level vertical vorticity. The Early Transient Mesovortex was also located ~4 km from the supercell hook echo due to its deviant eastward motion as the supercell moved to the east-northeast. We hypothesize that its low-level updraft enhancement was likely the result of the broader ascent induced by the supercell within the inflow. The updraft enhancement was not enough to sustain the feature, as reflectivity evidence of it disappeared entirely by 2325 UTC (not shown).

4.4.3. Tornadogenesis (2335 – 2345 UTC)

The Tornadogenesis analysis period is centered around the approximate time of tornadogenesis of the Monroe supercell's EF-0 tornado – 2340 UTC – as indicated by both the damage survey and the radar analyses. The tornado developed rapidly, with significant storm-scale evolutions between the 5-minute spaced analyses. Although our temporal and spatial resolution is insufficient to capture the finer details of tornadogenesis, we are able to observe the storm-scale processes associated with it and the evolution of the horizontal and vertical vorticity fields.

The radar presentation of the Monroe supercell had improved by 2335 UTC (Figure 24) compared to the latter half of the Early Transient Mesovortex period. A west-southwestward extending reflectivity hook echo was present along a notable northward deflection of storm relative winds. While low-level vertical vorticity was minimal, a broad low-level updraft was present within the inflow notch and in the inflow sector. Immediately adjacent to the main supercell updraft, a secondary updraft located at (70.5 km E, 44 km N) on Figure 24 was co-located with a small reflectivity enhancement of 15 dBZ at 1 km AGL. And although reflectivity was weak, at 1 km AGL a clear corridor of 10 dBZ reflectivity appeared to connect this feature with the hook echo at this time. This feature, along the southern dotted line representing the backwards and forwards interpolation of storm-motion on the 2340 UTC tornado-cyclone, likely represents the early formative stages of the tornado-cyclone.

In contrast to the Early Transient Mesovortex period (see section 4.4.2), a broad signal of enhanced streamwise vorticity that maximized within the inflow notch was located within the inflow sector. Based on its location within the open warm inflow sector, we hypothesize that this streamwise vorticity was either a pre-existing enhanced pocket being ingested by the storm or represented streamwise vorticity barotropically-enhanced by storm-scale horizontal accelerations into the strengthening low-level updraft.

The $\theta_v{}'$ surface analysis confirmed a modest thermodynamic gradient associated with the northerly wind near and east of the hook echo. The DLA also revealed a colder pocket of air immediately west-northwest of the hook echo. Since this cold air was not associated with a notable wind shift, we hypothesize that this colder air was associated with an RFD surge at 2330 UTC, which had since advected along storm-relative outflow winds to the northwest. Interestingly, the thermodynamic boundary consisting of the RFGF and FFCB was continuous along the storm, and, aside from the colder portion to the northwest of the hook echo possibly associated with an earlier RFD surge, the magnitude of the thermodynamic gradient appeared similar between the FFCB and RFGF. The boundary delineation point separating these two named boundaries was arbitrarily chosen as the approximate location the boundary crossed from "forward-flank" to "rear-flank" based on storm motion and the location of the low-level updraft, but the continuous nature of this boundary suggests that the physical differences between the portion of the boundary labeled as "RFGF" may not have been much different from that labeled "FFCB".

The 500 m θ_v' analysis (Figure 24f) depicts a small RFD located just west of the hook echo indicated by compressional warming effects right along the analyzed surface boundary. This downdraft was the only notable low-level RFD at this analysis time. Based on its storm-relative position, it likely represents the early stages of the downdraft closely associated with the development of the hook echo and tornadogenesis at 2340 UTC. The 500 m θ_v' analysis (Figure 24f) also revealed the shallowness of the supercell's cold pool. While the surface analysis shows an extensive area of the storm core and anvil region with –2 K θ_v' perturbations, the areal extent of those perturbations at 500 m was significantly reduced and reserved to the coldest portion of the surface cold pool at the far northern edge of the storm. The axis of the thermodynamic gradient along the FFCB between the surface and 500 m was consistent.

The Monroe supercell's hook echo region intensified significantly between the 2335 UTC and 2340 UTC analysis times (Figure 25). The reflectivity hook echo developed southward approximately 2 km from the previous analysis time along strong surface northerly winds associated with an RFD surge. At the southern tip of the hook echo at (45.5 km E, 74.5 km N) in Figure 25, aligned just west of the start of the surveyed tornado damage track, was an intense low-level mesocyclone. Although our analysis lacks the temporal and spatial resolution to explicitly resolve this tornado (note that it was surveyed as having a maximum width of 50 yards (~ 46 m) – much narrower than our 250 m grid spacing), the tornado's parent circulation was observed. This parent circulation feature is termed the "tornado-cyclone" in subsequent discussion. A secondary circulation of low-level mesocyclonic strength was located approximately two kilometers north of the tornado-cyclone, along the boundary between the RFD and the inflow (74.5 km E, 47.5 km N on Figure 25). We will term this feature the "Northern low-level mesocyclone".

A broad low-level updraft was present within the BWER and extending into the inflow with two distinct maxima at 1 km AGL: One vertically aligned with the low-level tornado-cyclone (termed the “tornado-cyclone updraft”), and the other to the northeast of the Northern low-level mesocyclone, near the intersection point of the RFGF, LFCB, and FFCB (76 km E, 48.5 km N on Figure 25; termed the “main supercell updraft”). The Northern low-level mesocyclone did not have a low-level updraft aligned vertically with it like the tornado-cyclone did – it was immediately adjacent to a strong low-level downdraft which likely played a significant role in the development of the RFGF and RFIS at this time.

A notable elongated patch of vertical vorticity was located along the eastward-extending FFCB (“eastward—FFCB”) at the northern edge of the inflow notch, most notably before a triple point with the southern-extending FFCB (“southward—FFCB”). It was located along a confluence boundary between southeasterly inflow and northeasterly winds from the core of the supercell, and a branch of enhanced low-level updraft also extended along this portion of the boundary. These features were all co-located with an elongated enhancement of streamwise vorticity leading into the main supercell updraft, and constitute an SVC (see section 4.4.5). Two other notable regions of enhanced streamwise vorticity were observed – a small patch at (79 km E, 46.5 km N) in Figure 25 associated with the baroclinic southward—FFCB, and a larger patch to the east-northeast of the tornado-cyclone within the inflow notch. This latter streamwise vorticity enhancement, not dissimilar to that seen at 2335 UTC (see Figure 24), likely had a large contribution from barotropic effects as inflow air was accelerated into the main updraft and around the tornado-cyclone, but may have also had a non-negligible baroclinic component with the weakly-baroclinic RFGF (see section 5) or from baroclinity associated with non-diabatic forcing (see section 6.6).

The combination of well-defined RFGF/RFIS, FFCB, and LFCB was first analyzed at 2340 UTC (Figure 25; see section 4.4.5). Two distinct FFCB boundaries were present: the eastward—FFCB extending from the main supercell updraft into the anvil region and featuring an SVC, and the southward—FFCB extending along the weak baroclinic boundary separating air diabatically cooled by anvil precipitation from the warm inflow. Whereas previously the axis of the θ' gradient was oriented northwest to southeast, a significant portion of that axis was oriented west to east due to strong northeasterly flow within the core of the cold pool, bringing the diabatically-cooled air to the northern edge of the inflow notch at this analysis time. Two distinct low-level RFD's were also evident via compressional warming effects in the 500 m AGL $\theta_v{}'$ field: one immediately northwest of the tornado-cyclone, and another, more diffuse region on the northwest side of the supercell (74 km E, 51 km N on Figure 25). Although these were two distinct regions of downward motion, they both were considered RFD's by their location and physical characteristics. Low-level divergence by the northern RFD provided low-level confluence along the LFCB and for the main supercell updraft as a whole. Although not evident at the surface or 500 m, $\theta_v{}'$ at 250 m (Figure 26) depicted weak baroclinity associated with the strong kinematic RFGF, particularly in the inflow notch and southeast extent of the RFGF. These boundaries will be discussed further in section 4.4.5.

At 2345 UTC, the Monroe supercell maintained an impressive reflectivity structure, low-level updraft, and surface boundary structure (Figure 27). The vertical vorticity of the tornado-cyclone decreased dramatically in strength and areal extent, leading us to term it a "remnant tornado-cyclone". While the damage survey track of the EF-0 tornado was continuous, and continued until 2253 UTC, the dramatic weakening of the vertical vorticity of the tornado-cyclone, the decrease in wind gusts associated with the RFGF it was located along, and long distance between damage points “2” and “3” lead us to hypothesize that the tornado may have lifted off the ground at this time (and, therefore, the later damage points would be associated with a separate surface circulation). However, as discussed in section 2.5, our grid spacing of 250 m was insufficient to directly resolve the tornado, and given how narrow the surface damage track was surveyed to be, it is plausible that the associated tornado-cyclone had narrowed significantly by this analysis time and our grid was unable to properly resolve it. However, due to the analyzed weakening and propagation of the low-level circulation at 2350 UTC (see section 4.4.4), we will treat it as a “remnant tornado-cyclone” and assume that there was no surface circulation until damage point “3”.

The northern low-level mesocyclone identified at 2340 UTC was no longer present at 2345 UTC, despite the strong low-level updraft centered along its projected position based on storm motion (Figure 27). The bifurcated low-level updraft structure observed at 2340 UTC was also replaced with a single elongated main supercell updraft, with extensions from the triple point of several surface boundaries along the RFGF south to the remnant tornado cyclone, north along the LFCB, and east along the eastward—FFCB.

The enhanced streamwise vorticity of the SVC, and its associated vertical vorticity, was still apparent along the north side off the eastward—FFCB. The northeast tilt to the eastward—FFCB was apparent along the east half of the SVC. Although not non-zero, streamwise vorticity south of the eastward—FFCB within the inflow had decreased from its maximum at 2340 UTC, coinciding with the rapid weakening of both low-level mesocyclones.

The northeasterly surface winds observed at 2340 UTC had become increasingly northerly by 2345 UTC, and at 500 m AGL had also turned to northeasterly (Figure 27). The result of these winds rotating towards the low-level updraft was the southward transport of the cold pool, most notably at the surface but also at 500 m AGL. As indicated by the eastward—FFCB location, cold air had surged south of the northern edge of the inflow notch, where the winds were the most northerly, while the eastern flank of this axis of cold air remained in the same storm-relative location. This gave the appearance that the eastward—FFCB was beginning to rotate counter-clockwise. The depth of the cold pool had also grown, with the areal extent of –2 K $\theta_v{}'$ at 500 m AGL expanding significantly. In contrast with 2340 UTC, where the coldest air at 500 m AGL was displaced northward of the surface boundary, at 2345 UTC the surface and 500 m AGL cold pool had better vertical alignment, particularly in the western portion.

The magnitude of the low-level RFDs had also decreased at 2345 UTC. However, divergence in the wind field and the effects of compressional warming from downdrafts further aloft were evident throughout the rear of the storm. Advection of compressionally-warmed air may explain the connection of the warm bubbles from the southern tip of the RFGF through the northern RFD, which provided a well-defined mid-boundary layer thermodynamic boundary along which the LFCB was analyzed.

4.4.4. Supercell decay (2350 – 0000 UTC)

Although the NWS-surveyed tornado continued until 2353 UTC, and an additional, separate EF-1 tornado damage point was assessed at 2355 UTC, the Monroe supercell began to undergo significant degradation in structure and intensity by 2350 UTC. This analysis period will focus on the evolution of low-level features and boundaries as the supercell's updraft was undercut by its surging cold pool and the storm began to merge with a developing MCS segment. By 0000 UTC, the storm could no longer be classified as a surface-based supercell.

The Monroe supercell underwent significant evolution between 2345 UTC and 2350 UTC, akin to the rapid evolution between 2335 UTC and 2340 UTC. The reflectivity structure degraded significantly by 2350 UTC (Figure 28). While the 45 dBZ contour line had an appearance of a classic supercell featuring a stub-like hook extending to the west/southwest at (81 km E, 53 km N), the southern hook echo extension seen at the previous two analysis times was an amorphous reflectivity blob that tenuously connected the stub-like hook echo to its north to the eastern anvil via a narrow corridor of 30 dBZ (Figure 28). The previously well-defined clear-air inflow notch was surrounded at the surface by these 30 dBZ bridges, and was beginning to get filled in with 15+ dBZ reflectivity as northerly winds, carrying the cold pool, surged through it. This southward surge of cold air is reflected in the placement of the eastward—FFCB, which has shifted south from previous analysis times and increasingly has a southwest-to-northeast axis, as well as the southward push of the RFIS. Interestingly, similar to 2335 UTC (see Figure 24), the southward—FFCB and RFGF appear to as a nearly-continuous single boundary. Although, unlike 2335 UTC, the RFGF was a mostly-kinematic boundary, and did not share the same baroclinity as the southward—FFCB.

Despite the southward surge of cold air through the inflow notch evident at both the surface and 500 m AGL, the Monroe supercell's low-level updraft remained moderately intense and was located atop this cold near-surface air. At 1 km AGL, the inflow notch remained precipitation-free and maintained south-southeasterly inflow to the main supercell updraft. The 500 m $\theta_v{}'$ plot (Figure 28) showed that nearly the entire main updraft had been undercut by cold air.

There remained several pockets of enhanced streamwise vorticity of interest at 2350 UTC. Most notably, several patches were located along the southward—FFCB and into the new, smaller inflow notch located at (83.5 km E, 47.5 km N) in Figure 28. These may be the result of baroclinically-induced rotor-like circulations along that boundary. A second, larger and more intense enhancement of streamwise vorticity was located primarily north of the eastward-extending FFCB (86 km E, 50 km N on Figure 28). While this enhancement does appear to be at least somewhat related to the baroclinic FFCB, it lacks the “river-like” appearance of concentrated streamwise vorticity along the eastward—FFCB seen at 2340 UTC and 2345 UTC (see Figures 25 and 27). Instead, it appeared over a broad area of the wind field extending deep into the storm core associated with the acceleration of the wind field associated with the sharpest $\theta_v{}'$ gradient above the surface, as seen by $\theta_v{}'$ at 500 m AGL (Figure 28e). While much of this streamwise vorticity enhancement may be due to the baroclinic mechanism associated with the elevated baroclinic boundary, the wide areal extent of the enhancement and lack of a singular boundary it was focused along lead us to determine that this feature should no longer be defined as an SVC.

Low-level vertical vorticity analysis reveals a disorganized region of weak vertical vorticity along the western flank of the anvil and a smaller concentrated area of mesocyclone-strength vertical vorticity co-located with damage point “3” (Figure 28). The latter strong mesocyclone was located near the intersection of mildly cooler air behind the southward—FFCB and the surging cold pool behind the eastward—FFCB. We hypothesize that the surface circulation associated with damage point “3” was from this low-level mesocyclone, representing a forward propagation of the low-level mesocyclone of more than double the speed by which the tornado-cyclone (and reflectivity hook echo) traversed from 2340 UTC to 2345 UTC. This accelerated propagation was likely the result of the occlusion process of the inflow.

The 2355 UTC analysis (Figure 29) depicts a continuation of the degradation process described at 2350 UTC. Although the storm maintains a modest semblance of a west-southwest hook echo following the 45 dBZ contour, the open inflow notch from the Tornadogenesis period had completely filled in with precipitation and cold air streaming in along strong north-northeasterly winds. Notable separate convective cells exceeding 30 dBZ had sprung up along the RFGF and RFIS as a strong surface anticyclone at (83 km E, 50.5 km N on Figure 29), the result of a strong low-level RFD, helped drive the southern push of cold air as well as the westward movement of it along the RFIS. Even as low-level updrafts began to initiate convective cells south of the RFGF, the main supercell low-level updraft remained present at (87 km E, 51 km N) on Figure 29, even with minimal low-level inflow feeding into it at 1 km. Based on the extensive cold pool evident at the surface and 500 m AGL, this updraft, and the Monroe supercell as a whole, could be described at this time as elevated.

Despite the overall degradation of the supercell, multiple regions of enhanced low-level streamwise vorticity persisted at 2355 UTC (Figure 29). A notable pocket of enhanced streamwise vorticity was located within the inflow sector, south of the cold pool and between the southward—FFCB and RFGF. This likely represents barotropic enhancement through accelerations in the wind field. A wide extent of enhanced streamwise vorticity, with multiple narrow appendages, was present within the western half of the anvil region of the supercell. Similar to 2350 UTC, while this enhanced vorticity was not associated with a surface baroclinic boundary, the portion of it extending northward does align with the axis of greatest $\theta_v{}'$ gradient at 500 m AGL, indicating a baroclinic component to its generation. However, it still lacked the concentrated “river-like” appearance of an SVC. Additional streamwise vorticity enhancements, appearing in a much more elongated and concentrated form, were present to the southeast of the eastward—FFCB. Most notable of these was the streamwise vorticity enhancement extending several kilometers to the southeast of damage point “5” (see also Figure 10), aligned well with the tightest portion of the baroclinic boundary of the southward—FFCB (as well as weak low-level updraft), and thus likely containing a significant baroclinic contribution. While this particular current of enhanced streamwise vorticity was deemed too transient to be called an SVC, its baroclinically-generated streamwise vorticity may have played a significant role in the concentrated low-level vorticity enhancement associated with damage point “5” (Figure 10), an EF-1 damage point assessed that was distinct from the primary EF-0 tornado the Monroe supercell produced. This low-level mesocyclone, co-located with damage point “5” at this analysis time, was located near the triple point of the southward—FFCB and eastward—FFCB, and still featured primarily southeasterly storm-relative surface inflow, although this inflow did pass through an extensive region of the anvil of the Monroe supercell. Interestingly, the surface ground-relative radar-analyzed winds at damage point "5" reveals northwesterly flow from the storm's rear flank entering the strong low-level mesocyclone and rotating counterclockwise around the surface damage point (not shown). Despite lacking the support of a notable low and mid-level updraft, the low-level mesocyclone intensified between 2350 UTC and 2355 UTC and produced EF-1 damage, possibly a result of favorable baroclinically-enhanced streamwise vorticity momentarily aligned in its inflow.

The convective storm featured at the 0000 UTC analysis time could hardly be described as a supercell (Figure 30). The reflectivity structure showed no semblance of a hook echo. Although there was no DLA run at this analysis time, based on the extent of northerly winds in the analysis we can conclude that the extensive cold pool continued to surge southward. Despite the lack of surface inflow, a low-level updraft continued to persist near the old storm-relative location of the clear inflow notch (91 km E, 53 km N on Figure 30).

A new broad updraft was located far to the south, along the new likely triple point of surface boundaries at (91 km E, 46 km N) on Figure 30. It was co-located with a weak low-level vertical vorticity enhancement and a small, but notable, reflectivity weakness which may have been an attempt of a re-development of an inflow notch. However, it is unclear whether the supercell would have been able to re-establish a balanced inflow and cold pool due to the storm colliding with developing MCS segments to its north and east at this time.

There was a broad region of enhanced streamwise vorticity extending from the new low-level updraft to the south to as far north as the old low-level updraft. Without a thermodynamic retrieval, it is impossible to definitively declare the role of the baroclinic mechanism in that vorticity enhancement, although based on the orientation of baroclinic boundaries at 2355 UTC (see Figure 29) and the wind field evolution, it is likely that a portion, and perhaps a significant portion, of that streamwise vorticity was baroclinically generated. Similar again to 2355 UTC, this streamwise vorticity enhancement was not concentrated enough to be termed an SVC.

4.4.5. Storm-scale surface boundaries

Storm-scale kinematic and thermodynamic boundaries were defined at the surface, with the exception of the LFCB which was primarily identified at 500 m AGL. The structure of the identified boundaries are explored in vertical cross sections of ${\theta_v}'$ at 2340 UTC in Figure 31.

Two distinct rear-flank downdrafts are seen in Figure 31a. The northern downdraft was the stronger and deeper of the two, featuring a taller column of compressionally-warmed air. The origin height of this northern RFD extended beyond the domain of Figure 31a, up to approximately 6 km AGL. The southern downdraft was by contrast much shorter, narrower, and weaker. The RFIS evident at 2340 UTC was directly related to this southern RFD. The cross section also reveals the depth of the cold pool of the RFD at only ~500 m. Directly under the downdrafts themselves, the cold air gradient was squeezed even closer to the surface due to the effects of compressional warming. The RFGF was evident at the surface at 0.5 km horizontal distance on Figure 31a as an entirely kinematic boundary. This boundary curved northward with height, and when the boundary was at 1 km AGL it was located at 2 km horizontal distance. The base of an elevated updraft coupled with the southern RFD was located along the gust front at 2 km horizontal distance, 1 km AGL. Although the eastern portion of the RFGF, near the tornado-cyclone and northern low-level mesocyclone, did feature some weak baroclinity at 2340 UTC, the primary baroclinity of the RFD was associated with the RFIS.

The eastward—FFCB, and its associated SVC, are represented in Figure 31b. The FFCB featured a relatively sharp $\theta_v{}'$ gradient of ~1.5 K over 750 m horizontal distance. The northward slant of the cold pool and its ultimate depth of around 1 km AGL deeper in the storm core were evident. The stacked warm $\theta_v{}'$ perturbations within the main updraft above 1 km AGL represent parcels cooling at their moist adiabatic lapse rate, and thus remaining unstable relative to the surrounding environment (see section 4.4.1). The low-level rotor-like circulation induced by this baroclinic boundary was evident at 6 km horizontal distance, 500 m AGL, characterized by stronger updraft on the south (warm) side of the boundary, and slight downward motion on the north (cool) side of the boundary. Although it was not a perfect rotor, the difference in vertical motion across the boundary was more than sufficient to produce notable streamwise vorticity as parcels travelling along the FFCB at this location were flowing to the main low-level updraft to the west (i.e., into the page). The inset Figure 31e focuses in on the SVC, showing streamwise vorticity contoured against $\theta_v{}'$. A distinct maxima of streamwise vorticity was present at 3 km horizontal distance, 750 m AGL, right atop the surface baroclinic boundary and within the rotor-like circulation. Although maximized at 750 m AGL, baroclinically-generated streamwise vorticity was present extending down to at least 250 m AGL. This streamwise vorticity, generated as parcels traveled along the eastward—FFCB, grew over time as parcels remained within the SVC (as seen in Figure 25; see section 5.1.3), before being tilted into vertical vorticity and stretched by the main supercell updraft. The presence of notable near-surface vertical vorticity along this boundary (see Figure 25) likely was the result of the tilting of baroclinically-generated vorticity by the updraft along this boundary.

The southward—FFCB (Figure 31c) featured a much more diffuse $\theta_v{}'$ gradient than the eastward—FFCB. Near the surface, $\theta_v{}'$ varied only on the order of 0.5 K per kilometer, although higher up at 250 m and 500 m AGL the gradient was ~1 K per kilometer. There were subtle indications in the low-level wind field of an updraft gradient from left to right, specifically with slightly stronger updrafts around 2.5 km horizontal distance, 500 m AGL, right along where the surface boundary was located, and weaker updrafts at 500 m AGL between 3 km and 4 km horizontal distance (Figure 31c). Unlike the eastward—FFCB, the rate of baroclinically-generated streamwise vorticity along this weak rotor-like circulation would be minor, and not reach the thresholds for an SVC. However, the southward—FFCB was longer than the eastward—FFCB, particularly prior to 2340 UTC, so parcels travelling along it would have spent more time within the region slowly accumulating streamwise vorticity, thus potentially enabling the small enhancement we observed on the cool side of the northern edge of the southward—FFCB at 2340 UTC (see Figure 25).

Unlike the previous boundaries discussed, the LFCB (Figure 31d) was not surface-based thermodynamically. While a surface confluence zone was present along it at 2340 UTC, the thermodynamic gradient associated with it was primarily between 500 m—1000 m AGL. The LFCB was bounded by compressionally-warmed air from the northern RFD to its northwest, and diabatically-cooled air of the supercell cold pool to its southeast. The presence of the highly-tilted main updraft in mid-levels above the cold pool helped to expand the cold pool vertically up to 1 km AGL, as at least a portion of it appears to be in the process of being transported upward by the updraft. At low-levels, this updraft was developed by low-level confluence, and aided by the dynamical low-pressure above it by the strong main supercell updraft. Unlike the FFCB's, which thermodynamically induced a rotor-like circulation which generated streamwise vorticity, the rotor-like circulation present at the LFCB (at 2 km horizontal distance, 500 m AGL on Figure 31d) appeared to be dynamically induced by the RFD to the northwest and updraft to the southeast. While this still generates streamwise vorticity for parcels travelling towards the main low-level updraft along the LFCB, the streamwise vorticity they generate was not generated baroclinically. The orientation of the thermodynamic gradient at the LFCB would induce a rotor circulation in the *opposite* direction, producing anti-streamwise vorticity instead and thus limiting, or even negating entirely, the dynamically-generated streamwise vorticity.

Surface rainwater mixing ratio, another output field of the DLA, was used to compare changes in the Monroe supercell's structure with the evolution of its storm-scale boundaries discussed above. Surface rainwater mixing ratio was used as a proxy measure for diabatic cooling. Surface Graupel/hail mixing ratio was not considered due to exceptionally low values, consistent with the lack of hail reports with the Monroe supercell and low values of graupel/hail aloft (see Figure 19). While the DLA did explicitly retrieve the amount of cooling along parcel trajectories, and partition the cooling into separate grapuel/hail melting and rainwater evaporation categories, a deeper exploration of diabatic cooling as it relates to storm structure was outside the scope of this project. The rainwater mixing ratio proxy will enable us to draw broad hypotheses about the evolution of the supercell which can be explored in a future project.

Figure 32 contains the surface rainwater mixing ratio for early in the supercell's evolution (2310 UTC), during the tornadic phase (2340 UTC and 2345 UTC), and during the beginning of the decay phase (2350 UTC). 2310 UTC featured the greatest rainwater mixing ratio rates, with nearly all of the rainwater concentrated along the long FFCB. At 2340 UTC, the areal extent of elevated rainwater mixing ratios had expanded, but the high magnitude peak seen at 2310 UTC was not present. The majority of the rainwater was concentrated north of the eastward—FFCB, with lesser rainwater present down the southern anvil. At 2340 UTC and 2345 UTC, the southward—FFCB was at its shortest. This contraction of the southward—FFCB was correlated to the weakening of rainwater mixing ratio present southward along the hook. By 2350 UTC, although not matching the magnitude or extent from 2310 UTC, rainwater mixing ratio along the southern anvil had increased compared to 2340 UTC, coinciding with an elongation of the southward—FFCB observed at this analysis time. Throughout all four analysis times, the amount of rainwater mixing ratio within the hook echo was minimal. The amount and areal extent of rainwater in the northern half of the storm (i.e., not trailing south along the anvil) was increased for the latter analysis times when the LFCB, eastward—FFCB, and RFGF/RFIS were well-defined. These brief results merely scratch the surface of the type of analysis capable with the DLA, and pose interesting avenues for further study of this supercell and others.

Chapter 5: Trajectory Analysis

Selected DLA trajectories and their environments are analyzed and reported in the following discussion. Trajectories are calculated backward in time from analysis gridpoints as described in Chapter 2.

5.1. The early transient mesovortex (2310 UTC)

An ensemble of storm-relative 10-minute long trajectories entering the Early Transient Mesovortex feature at 2310 UTC were run at all locations of the feature ending at 250 m and 750 m AGL (Figure 33a,c). Timeseries depicting the height, vertical velocity, and vertical vorticity of each individual trajectory within the ensemble were also presented (Figure 33b,d). Although, as noted in section 4.4.2., the evolution of the Early Transient Mesovortex was too rapid for us to accurately capture with our temporal resolution of 5-minute analyses, these trajectories reveal the character of parcels entering the feature during its development. Nearly all trajectories, both those ending at 250 m AGL and those ending at 750 m AGL, originated below 250 m within the open inflow sector. The parcels ending at 250 m AGL demonstrated only slight vertical motion during their approach to the Early Transient Mesovortex, while most ending at 750m AGL within the feature had at least modest vertical motion. All parcels begin with little-to-no vertical vorticity, and that did not change for the majority of their approach to the Early Transient Mesovortex. Within the last 2-3 minutes of the timeseries, when trajectories were gaining modest vertical velocity and many, particularly those within the 750 m AGL envelope, were deflected off of their southeasterly storm-relative flow, vertical vorticity magnitudes did increase, but it did so in both the positive and negative direction. The presence of both positive and negative vertical vorticity within these trajectories was likely a result of the small size of the eventual low-level mesovortex that would be seen at 2315 UTC – this spread of parcels likely encapsulates both the mesocyclone and meso-anticyclone associated with the feature. The lack of notable vertical vorticity prior to immediately prior to these parcels entering the Early Transient Mesovortex, combined with their origin points within the storm inflow region and far from the observed baroclinic boundaries at this time, lead us to hypothesize that the vorticity associated with the Early Transient Mesovortex was primarily the result of the tilting and stretching of ambient horizontal vorticity, with perhaps a local boundary layer vorticity enhancement not associated with the Monroe supercell.

5.2. The tornado-cyclone and northern low-level mesocyclone (2340 – 2345 UTC)

An ensemble of nine 10-minute long trajectories with endpoints within the tornado-cyclone at 2340 UTC at 250 m AGL were run (Figure 34). All trajectories originated within the open inflow sector of the supercell, and all but two of these trajectories originated within the lowest 60 m AGL. There were three distinct pathways parcels took to get to the tornado-cyclone: First, five of the nine parcels took a wide arcing loop through the inflow notch and approached the tornado-cyclone from the north and west via the RFGF. Two of these five parcels had notably a long residence time within the RFGF, traveling to the tornado-cyclone from 2—3 km north of it. Second, two of nine approached from the southeast, crossing the tornado-cyclone before sharply wrapping around it. Third, the final two parcels approached from the inflow to the southeast, directly entering the tornado-cyclone and originating at 120 m AGL, an order of magnitude higher than the other seven parcels.

Timeseries following each trajectory showed that all but two of the nine parcels only rose up and into the tornado-cyclone. Two trajectories experienced brief downward motion 2-3 minutes prior to 2340 UTC, but the magnitude of this descent was only on the order of 10s of meters. While all parcels did not start gaining significant magnitudes of vertical vorticity until the final 2 minutes, the parcels maintained a slightly-positive vertical vorticity for the entirety of their path to the tornado-cyclone. This vertical vorticity was available to be immediately stretched by the low-level tornado-cyclone updraft.

Ambient streamwise vorticity analyzed at and below 250 m was minimal, although, as noted in section 4.3, the radar analyses may have underestimated the very low-level wind shear. None of the parcels, not even the two most northern ones, travelled close enough to the SVC (seen as the slight 5 s^{-1} enhancement of streamwise vorticity in the upper right quadrant of Figure 34) to transport that baroclinically-generated streamwise vorticity to the tornado-cyclone. While weak baroclinity was evident between the RFGF and inflow notch at 250 m AGL (see Figure 26), there did not appear to be robust generation of streamwise vorticity along this boundary. We hypothesize that a notable amount of low-level vertical vorticity was developed barotropically by the horizontal shear zone at the interface between the southeasterly inflow and north-northwesterly RFGF surge (see section 6.5). Baroclinically-generated vorticity did not appear prevalent in the tornado-cyclone during tornadogenesis.

An ensemble of six 10-minute parcel trajectories ending at 250 m within the northern low-level mesocyclone at 2340 UTC showed some similarity, but also some distinct differences, to the tornado-cyclone trajectory ensemble (Figure 35). All trajectories originated under 100 m AGL and within the open inflow sector, but these trajectories originated along the eastern edge of the inflow sector and travelled along long arcing paths across the north edge of the inflow notch. While two trajectories did feature a sharp turn at their end within the northern low-level mesocyclone, most trajectory paths were dominated by gradual turning. Unlike the trajectories of the low-level tornado-cyclone, which featured multiple distinct origin point clusters, these trajectories all originated within the same region and travelled along similar pathways in a single envelope. The northern edge of this envelope did near the SVC, and may have experienced some modest vorticity enhancement, but it does not appear that the core of the SVC was feeding the northern low-level mesocyclone at 250 m.

The trajectory timeseries for the northern low-level mesocyclone (Figure 35) unsurprisingly was similar to that of the tornado-cyclone (see Figure 34). The significant difference between the two was the presence of a notable downdraft within the mesocyclone itself, a result of the overlapping of the northern low-level mesocyclone with the southern RFD just above a portion of it. The magnitude of positive vertical vorticity, and its rate of increase over time, was less than that for parcels entering the tornado-cyclone. Several trajectories also featured *negative* vertical vorticity within the mesocyclone. It is worth noting, however, that the trajectories with negative vertical vorticity also (i.e., the brown and green trajectories from Figure 35) simultaneously featured the strongest updrafts, perhaps indicating that these parcels contained anti-streamwise vorticity which was being tilted and stretched into negative vertical vorticity. Although streamwise vorticity magnitudes at 250 m were small, these parcels did originate within an expansive region of weak anti-streamwise vorticity, and the northern end of the trajectory envelope did pass through a region with enhanced anti-streamwise vorticity just north of the northern low-level mesocyclone. Conversely, the parcels with the strongest positive vertical vorticity within the northern low-level mesocyclone (i.e., the red, orange, and blue trajectories from Figure 35) featured *downward* vertical motion within the mesocyclone.

An ensemble of six 15-minute parcel trajectories ending at 250 m AGL were run for the smaller remnant tornado-cyclone at 2345 UTC (Figure 36). The characteristics of these trajectories were significantly different than most of those for the tornado-cyclone at 2340 UTC (see Figure 34). All trajectories, while originating within the inflow sector, traveled along a long arcing path within the inflow notch, entering the northerly RFGF along the hook echo near the location of the northern low-level mesocyclone at 2340 UTC (see Figure 35) and traveling to the remnant tornado-cyclone from the north through the RFGF. Unlike at 2340 UTC, no parcels entered the (now-remnant) tornado-cyclone directly from the southeasterly inflow. All but one of the trajectories featured notable downward motion (for some parcels on the order of 250 m of descent) five minutes prior to entering the remnant tornado-cyclone, likely when they entered the RFGF near the northern low-level mesocyclone. All of the parcels descended below 250 m AGL and rose within mild updrafts for the final three minutes.

Unlike the 2340 UTC trajectory runs, a correlation was evident within the 2345 UTC remnant tornado-cyclone envelope of increased vertical vorticity associated with downward motion (Figure 36). Two distinct examples of this exist within the 15-minute timeseries. At –660s, the two northern trajectories of the envelope (the blue and orange trajectories from Figure 36) experience a brief ~1 m s^{-1} downdraft. Coincident with this downdraft, both parcels feature a modest peak in positive vertical vorticity. A similar scenario occurs at –360s, where all six parcels experience a downdraft on the order of ~3 m s^{-1}, and a peak in positive vertical vorticity occurs for all parcels at the same time. There was not a significant low-level updraft present at the remnant tornado-cyclone at 2345 UTC, yet all parcels already had significant low-level positive vertical vorticity when they enter the remnant tornado-cyclone. The mechanism for this positive vertical vorticity appears to be the baroclinically-generated streamwise vorticity developed along the parcels being reoriented into positive vertical vorticity, a mechanism hypothesized to be crucial in tornadogenesis (see section 1.1). However, it should be noted that at 2345 UTC, the tornado has already been ongoing for up to five minutes and may have even lifted entirely.

An ensemble of ten 15-minute deep-storm trajectories were run at 2345 UTC (Figure 37). These trajectories were selected via the threshold that they pass through x-coordinates 74.0—75.75, y-coordinates 45.0—46.5, z-coordinates 0.25 km—1.0 km (i.e., a volume around the tornado-cyclone at 2340 UTC) and were required to have a vertical vorticity exceeding 20 x 10^{-3} s^{-1} and vertical velocity exceeding 10 m s^{-1} while they were within the low-level tornado-cyclone. The primary objective of this ensemble was to see where parcels which were ingested by the tornado-cyclone and its associated updraft ultimately went during the five minutes after they entered the low-level tornado-cyclone. Note that while the criteria for the parcels were based on the 2340 UTC position of the tornado-cyclone, Figure 37 depicts the radar analysis at their ending time, 2345 UTC, so the tornado-cyclone location and intensity depicted in Figure 37 is not representative of the tornado-cyclone these trajectories entered. Parcels which fulfilled this set of criteria universally came from the inflow sector and entered the tornado-cyclone directly from the southeast. The majority of them also originated at a higher elevation than the parcels which consisted of the 250 m AGL 2340 UTC tornado-cyclone (Figure 34), although all trajectories still originated at or below 350 m AGL. After entering the low-level tornado-cyclone, parcels rose rapidly in its associated updraft over the inflow notch to the northeast. This trajectory pathway represents the strong tilt of the low-level updraft. Parcel vertical motion began to stagnate around 3.5 km AGL before parcels encountered an updraft pulse which accelerated them upwards. As of 2345 UTC, parcels which were ingested by the low-level tornado-cyclone had not yet fully exited the mid-level supercell updraft.

The timeseries of this ensemble of trajectories (Figure 37) depicts these parcels entering the low-level tornado-cyclone between seven minutes (–420 s) and five minutes (–300 s) before 2345 UTC. Parcel vertical vorticity began to increase from small, but positive, values at least

60—120s prior to entering the tornado-cyclone updraft. It is also notable that at least two of the parcels in this ensemble contained slightly negative vertical vorticity at –900 s, although it had changed into positive vertical vorticity within the first minute of the trajectory. Although parcels entered the tornado-cyclone at a range of times, all parcels achieved a peak vertical vorticity between 20 x 10^{-3} and 35 x 10^{-3} s^{-1} around the –320 s point, and the majority of parcels achieved a similar maximum vertical velocity on the order of 15 m s^{-1}. From –300 s on, vertical velocity and vertical vorticity began to decrease in all of the parcels gradually, before significant drops in both were common at the –180 s mark, representing the temporary stagnation of these parcels at the "top" of the associated tornado-cyclone updraft at 3.5 km AGL. Many parcels entered an enhanced pulse of the mid-level supercell updraft which exceeded the updraft speeds of the tornado-cyclone within the final two minutes leading up to 2345 UTC. Parcel vertical vorticity during this time was consistent and clustered between 5 x 10^{-3} and 10 x 10^{-3} s^{-1}.

5.3. The Streamwise Vorticity Current (2340 – 2345 UTC)

Ensembles of trajectories were run for the SVC at 2340 UTC and 2345 UTC to determine both the source region of parcels entering the SVC and also to determine how the parcels with baroclinically-enhanced streamwise vorticity may have influenced the supercell.

Figure 36 shows an ensemble of eight 10-minute trajectories which were deemed to have been within the SVC at 2340 UTC. In a similar manner to Figure 37, while these trajectories were thresholded based on their 2340 UTC location, they were plotted at 2345 UTC, and so the intensity of the SVC and low-level wind field do not reflect the exact conditions these parcels experienced at 2340 UTC. While the broad reflectivity structure and SVC location was relatively unchanged from 2340 UTC to 2345 UTC, the most notable difference at 2345 UTC was the presence of north-northeasterly winds gusting through the SVC and into the northern inflow notch, which was not occurring at 2340 UTC when these parcels were along the SVC (see Figure 25). The shown trajectories all traversed through the x-coordinates 75.5—77.5, y-coordinates 47.75—48.75, and z-coordinates 0.25—1.0 km AGL, and within that volume had to attain a vertical vorticity of at least 10 x 10^{-3} s^{-1} (a proxy used to identify parcels within the SVC, as full 3-D vorticity dynamics (e.g., Dahl et al. 2014; Markowski et al. 2014) along trajectories are not yet a feature of the DLA but are in preparation (Conrad Ziegler, personal communication, 2022) and vertical velocity of at least 10 m s^{-1}.

The trajectories which entered the SVC originated five minutes previously to the southeast, on the cool side of the southward—FFCB (see Figure 25). These parcels originated below 500 m AGL, and many passed through the region of enhanced streamwise vorticity associated with baroclinically-generated vorticity along the southward—FFCB. The parcels then traveled along a substantial length of the eastward—FFCB where the SVC was positioned at the north edge of the inflow notch, rising gradually but remaining below 750 m AGL. The parcels then reached the low-level main supercell updraft along the northwest corner of the inflow notch and rose rapidly. As parcels reached the mid-levels of the supercell updraft, they began to drift back to the east, but demonstrated that the main supercell updraft had less tilt than the tornado-cyclone updraft (see Figure 37). By 2345 UTC, most parcels were still within the main updraft at 6-7 km AGL. Although trajectories ending at 2350 UTC were not run, we hypothesize that, based off of the streamlines present within the cross section of Figure 38, these parcels would exit the main updraft at approximately 9 km AGL. The timeseries of this trajectory ensemble (Figure 38) show the parcels with modest updraft and slowly growing vertical vorticity (although at least two parcels demonstrated decreasing vertical vorticity) from –480s to –360s, when these parcels were within the SVC. Upon reaching the main updraft, parcels rapidly attained a peak updraft speed of ~20 m s^{-1} and all maintained nearly identical updraft speeds which gradual decreased towards 15 ms^{-1} by 2345 UTC. Vertical vorticity, which grew gradually for most parcels within the SVC, remained consistent around 10 x 10^{-3} s^{-1} for the majority of the time the parcels were within the main supercell updraft, aside from a brief peak up to nearly 20 x 10^{-3} s^{-1} just after most parcels attained their maximum vertical velocity around 2-3 km AGL, likely a result of the tilting and stretching of streamwise vorticity developed in the parcels while they travelled along the SVC. Vertical vorticity decreased to below mesocyclone strength in the final two minutes leading up to 2345 UTC, but remained positive. These trajectory pathways demonstrate clearly that the SVC fed enhanced streamwise vorticity to the main supercell updraft, but did not contribute directly to the tornado-cyclone.

Figure 39 shows a wide ensemble of seventeen 10-minute trajectories ending within the SVC at 500 m AGL at 2345 UTC. Trajectory endpoints were selected within a wide array of enhanced streamwise vorticity, both along the eastward—FFCB at the north edge of the inflow notch, where the SVC had been located at 2340 UTC, as well as the region extending north-northeast from there, where enhanced streamwise vorticity was associated with the axis of the θ' gradient at 500 m (see Figure 27). All trajectories originated below 350 m AGL ten minutes prior to their end. A cluster of five trajectories originating in the bottom right quadrant of Figure 39 follow a similar path to those entering the SVC in Figure 38. However, crucially, these parcels were originating within the anvil region, farther east of the southward—FFCB and likely affected by precipitation within the anvil. These five parcels entered the eastern end of the SVC, at the northeast edge of the inflow notch. The six parcels which comprised the western extent of the SVC, where streamwise vorticity was most enhanced prior to being ingested by the main supercell updraft, did not originate in the southeasterly inflow region. Three of these six parcels originated due east of the SVC, arcing through the low-level cold pool. The other three parcels explicitly originated within the cold pool of the supercell and traveled southwesterly along it to reach the SVC. This stands in stark contrast to parcels which entered the SVC at 2340 UTC, which travelled along a substantial length of the eastward—FFCB. At 2345 UTC, SVC parcels in proximity to the main supercell updraft were embedded within flow oriented more perpendicular to the baroclinic boundary, resulting in them attaining less baroclinically-developed streamwise vorticity. The lack of residence time travelling along the eastward—FFCB was likely the reason why the SVC diminished in strength at 2345 UTC and was not present by 2350 UTC. The eastern and northeastern branches of the SVC at 2345 UTC also feature parcels with shorter residence times compared to the SVC at 2340 UTC.

Chapter 6: Discussion

6.1. Comparing the early transient mesovortex to the tornadogenesis event

The evolution of the Early Transient Mesovortex and tornadogenesis at 2340 UTC were different, but had distinct similarities. Both features developed rapidly in similar storm-relative positions ~2 km south of the previous southern extent of the reflectivity hook echo. Two natural questions arise from this: First, did these two features develop by the same mechanism, with the Early Transient Mesovortex representing a tornadogenesis "failure" and the 2340 UTC tornadogenesis representing the same process succeeding? And second, did the Early Transient Mesovortex modify the environment in such a way to facilitate tornadogenesis at 2340 UTC directly or influence the re-strengthening of the Monroe supercell more broadly? This subsection will contend more with the former, as the latter was deemed too far outside the scope of this thesis.

Figure 40 shows the low and lower-mid level vertical vorticity and wind field of the tornado-cyclone at 2340 UTC and the Early Transient Mesovortex at 2315 UTC. The cross section angle of 60 degrees was chosen as it best follows the low-level tilting observed in both features. Both the Early Transient Mesovortex and tornado-cyclone feature a mesocyclone which was maximized below 1 km AGL and vertically-aligned through 1 km AGL. Above 1 km AGL, both vortices tilted to the northeast. However, while the tornado-cyclone was supported by a strong mid-level mesocyclone above the BWER at 1.5 km AGL, the Early Transient Mesovotex had no such support from the Monroe supercell. Vertical vorticity above 1 km AGL of the Early Transient Mesovortex gradually diminished as it tilted to the northeast, with only a very modest updraft present at 5 km horizontal distance, 2 km AGL (Figure 40a). Without the support of a mid-level mesocyclone, the low pressure dynamically induced in low-levels by the Early

Transient Mesovortex may have induced a downdraft (potentially the downdraft seen at 3.5 km horizontal distance, 2 km AGL in Figure 40A) which subsequently resulted in both the weakening of the low-level updraft previously associated with the Early Transient Mesovortex (see Figure 21) and also the low-level vertical vorticity.

Another significant difference evident in Figure 40 was the reflectivity structure of both features. The Early Transient Mesovortex had a 30 dBZ reflectivity maximum at the surface which decreased with height, with only a tenuous 15 dBZ reflectivity echo connecting the feature to the supercell. While the tornado-cyclone had a similar reflectivity magnitude at the surface, reflectivity was maximized aloft. A wide corridor of 30+ dBZ extended above the surface, widening substantially with height. And although the vortex tilted to the northeast, a reflectivity column was vertically aligned with the tornado-cyclone through at least 3 km AGL, unlike in the Early Transient Mesovortex where the reflectivity contours closely followed the northeast tilt of the vertical vorticity.

Figures 41 and 42 show a sequence of full-storm-depth cross sections through the Early Transient Mesovortex at four analysis times covering its development and decay across 15 minutes. While there were signs of weak reflectivity on the order of 10—15 dBZ extending down the mid-levels at 2305 UTC, the Early Transient Mesovortex developed primarily as a surface-based feature 2310 UTC beneath a strong mid and upper-level updraft pulse of the supercell (Figure 41). It is unclear how influential this supercell updraft was to the development of the Early Transient Mesovortex, and further exploration of that is outside the scope of this thesis. By 2315 UTC, the supercell updraft atop the Early Transient Mesovortex had weakened significantly. If the mid-level updraft was a crucial component to the Early Transient Mesovortex, the weakening of it may have played a role in its quick demise. By 2320 UTC, the

Early Transient Mesovortex was little more than a remnant reflectivity echo even further disconnected from the supercell, even as there was some rebound of vertical velocity atop the feature and in the mid-levels above it (Figure 42).

Figures 43 and 44 shows the same sequence of plots but for the development of the tornado-cyclone. While the temporal resolution of our analyses was too poor to capture the small-scale details, it appeared that the tornado-cyclone developed as part of downward descending reflectivity, unlike the Early Transient Mesovortex which appeared to be a boundary layer-based feature. At 2330 UTC, a strong mid-level updraft was positioned over the eventual location of the tornado-cyclone. Weak reflectivity on the order of 20 dBZ was present within this updraft between 1 km and 3 km AGL before it reached the higher reflectivity of the supercell. At 2335 UTC, a mid-level downdraft, possibly the beginning stages of the southern RFD (see Figure 25) was present within a broad expanse of ~20 dBZ over the eventual tornado-cyclone location (Figure 43). We hypothesize that it was this downdraft which brought the reflectivity from aloft down to the surface that was seen at 2340 UTC. At 2340 UTC, the tornado-cyclone's reflectivity had descended to the surface along with the southern RFD. A strong updraft associated with the tornado-cyclone extended up to ~3.5 km AGL, and the main supercell updraft was evident further to the northeast. A well-defined BWER was present in the inflow notch. At 2345 UTC, the reflectivity of the tornado-cyclone (now remnant tornado-cyclone) expanded in aerial extent (Figure 44). The distinct tornado-cyclone updraft was no longer present, replaced with a wider main supercell updraft above the BWER, which was contracting due to cold air surging down from the supercell cold pool to the north combined with the gradual expansion of the reflectivity extent of the hook echo.

Despite the initial appearance of similarities between the development of the tornado-cyclone at 2340 UTC and the Early Transient Mesovortex, the Early Transient Mesovortex developed primarily as a boundary-layer feature confined to the lowest 1 km AGL, with the tornado-cyclone (and reflectivity hook echo at 2340 UTC generally) developed via downward descending reflectivity likely directly associated with the southern RFD. We hypothesize that the large-scale weakening of the supercell at 2315 UTC likely played a role in the demise of the Early Transient Mesovortex, but it is unknown whether the feature would have become part of the supercell or produced a tornado had the supercell not weakened.

6.2. Deep updraft characteristics

While much of the previous results were focused on specific low-level features of the Monroe Supercell, this subsection will briefly discuss the broad structure of the mid and upper level updraft.

As discussed previously (section 4.4.3), the Monroe supercell featured a bifurcated, comma-shaped updraft at 2340 UTC with two distinct maxima's, one along the southern end of the hook echo directly associated with the tornado-cyclone and the other approximately 2 km north, the main supercell updraft, which was fed enhanced streamwise vorticity from the SVC (see section 5.1.3) (Figure 45). These two maxima were connected via a comma-shaped broader updraft. By 1.5 km AGL, the two distinct updrafts were in closer proximity and the intensity difference between them and along the updraft corridor connecting them was minimizing. The separation of the two updrafts was most notable in the low-levels (see Figure 25). By 2345 UTC, the mid-level updraft became a singular north-south elongated updraft, with its peak updraft speeds located between the location of the tornado-cyclone updraft and main supercell updraft at 2345 UTC (Figure 45).

Deep full-storm vertical cross section cuts along storm-motion and through the main supercell updraft at 2340 UTC, and shifted along storm-motion to the same storm relative position at 2345 UTC, reveal the vertical structure of these updrafts (Figure 45). At 2340 UTC, the main supercell updraft was maximized between 2 and 3 km AGL, with a broad column of 15+ m s^{-1} updraft extending up a vertical column above the northern edge of the BWER up to 6 km AGL (Figure 45a). To the east-northeast of the main updraft was a broad mid and upper level 10+ m s^{-1} updraft. A small column of 45 dBZ extending above 7 km AGL at 2340 UTC – the maximum height of 45 dBz within the rest of the storm at this analysis time (Figure 45c) – was located directly above the strongest, and deepest, portion of the main updraft, representing consistency between the reflectivity and radar-analyzed wind field.

At 2345 UTC, the strongest portion of the main supercell updraft was to the east-northeast of the low-level updraft position, and located between 5 and 9 km AGL (Figure 45d). An extensive upward expansion of reflectivity was associated with this elevated updraft pulse, which appears to be the low to mid-level updraft pulse at 2340 UTC advected east-northeast along storm motion and up along the updraft. A broad low and mid-level updraft was still present above the BWER, but the most intense vertical motion, associated with a brief pulse in updraft strength at 2340 UTC, was being advected away. This evolution demonstrates that the Monroe supercell updraft was not a traditional steady-state supercell updraft, but rather it featured distinct pulses. While notably weaker than the 2340 UTC updraft pulse, a small region of 15 m s^{-1} updraft contour was located to the east-northeast of the main low and mid level updraft at 2340 UTC (6.5 km horizontal distance, 5.5 km AGL on Figure 45c). The updraft depth associated with that slight, disconnected enhanced updraft was ~1 km higher than the region of updraft separating the it from the main updraft pulse at this time. Although minor compared to the effects of the 2340 UTC main updraft pulse, as seen at 2345 UTC, this smaller feature evident at 2340 UTC likely represented an earlier updraft pulse being advected up and away from the surface, similar to how the 2340 UTC updraft pulse was.

The elevated updraft pulse at 2345 UTC, and its associated reflectivity, extended up to 11 km AGL, ~3 km higher than the height of the storm at 2340 UTC (Figure 45c). The magnitude of this growth demonstrates the strength of the updraft pulse at 2340 UTC, and also showed that parcels would traverse the depth of the storm on the timescale of 5-10 minutes. The structure and morphology of the Monroe supercell updraft is discussed in relation to other HSLC supercells in section 6.7.

6.3. Surface boundaries

Surface boundaries in the Monroe supercell were assigned using the definitions set forth by BW13. At 2340 UTC (Figure 31) and following analysis times, two separate baroclinic boundaries classified as FFCBs – an eastward—FFCB, along which an SVC developed, and a southward—FFCB. Both boundaries were characterized by a degree confluence along them and θ' gradients across them caused by differential diabatic cooling of low-level air by the supercell (BW2013). While the eastward—FFCB was notably stronger than the southward—FFCB in both thermal gradient and confluence, both boundaries, at 2340 UTC at least, featured streamwise vorticity enhancements along their cool side in line with baroclinic vorticity generation seen in both simulations and observations (BW2013; Schueth et al. 2021). The southward—FFCB intersected the eastward—FFCB at the northeast corner of the inflow region of the supercell. This boundary was between the warm southerly inflow and diabatically cooled inflow underneath the southern anvil of the supercell, although the baroclinity may have been enhanced by non-diabatic mechanisms (see section 6.6). The eastward—FFCB could be broken into two segments: A western segment, from the southern—FFCB intersection point to the low-level updraft, where the boundary separated warm inflow within the inflow notch from diabatically-cooled air from the forward-flank, and an eastern segment, east of the southern—FFCB intersection point, where the boundary separated air cooled diabatically from anvil precipitation from air with significantly more diabatic cooling in the forward flank. This dual FFCB structure at 2340 UTC was the result of a combination of a significant precipitation gradient between the forward-flank and the southern anvil (Figure 32) and the orientation of the anvil extending southward due to northerly upper-level flow (Figure 17). This dual structure was not present in the BW13 simulation due to their more “classic” Central Plains-type hodograph featuring strong west-southwesterly winds aloft. The implied motion of their simulated supercell was to the east-northeast, similar to the observed motion of the Monroe Supercell. But the upper level wind profile for the Monroe supercell placed the forward anvil to the south, in a region typically associated with open, unaffected inflow for most classic supercells and simulations.

At 2310 UTC, when a wide expanse of precipitation, and resulting diabatic cooling, was more equitably distributed along the forward-flank and southern anvil (Figure 32) only a single FFCB extended to the southeast, roughly parallel to the precipitation gradient between the supercell and inflow region (Figure 21). This not only supports our hypothesis regarding the cause for the dual-FFCB structure at 2340 UTC, but the continuous interface between the FFCB and RFGF also validates the structure of these boundaries during the (relatively) early evolution phase (Schueth et al. 2021; BW13). By 2350 UTC, rainwater mixing ratio had increased in the anvil region, south of the eastward—FFCB, and correspondingly we saw an increase in θ_v' gradient extending south-southeast along the southern anvil, leading to the lengthening of the southward—FFCB from its 2340 UTC length (see Figure 25) to a length closer to what we saw at 2310 UTC (see Figure 21) by 2355 UTC (see Figure 29).

Unlike the previous simulation work, an LFCB was not present at 2310 UTC (Figure 21), and when it was observed at 2340 UTC and onward (Figure 25, 27—29), the baroclinity associated with it was not surface based, but rather evident between 500 m—1000 m AGL, atop a broad surface cold pool (Figure 31). While the DLA was not run between 2310 UTC and 2335 UTC, and therefore baroclinic boundaries were not identifiable during that span, at 2335 UTC no LFCB was present (see Figure 24). Therefore, the presence of an LFCB at 2340 UTC leads us to conclude that it developed along the boundary between the compressionally-warmed air descending down the RFD and the diabatically-cooled air of the FFD, rather than evolve in the forward-flank and then rotate counter-clockwise to this final steady-state position (BW13; Schueth et al. 2021). The Monroe supercell's LFCB also featured warmer θ_v' on its rear side at 500 m AGL, as opposed to simulations which, at the surface, depict *colder* air on the rearward side. One hypothesis for this discrepancy may be the result of the weak RFD of the Monroe supercell and its comparatively weak cold pool (discussed more in section 6.7). Another speculative hypothesis is that the lack of hail within the Monroe supercell compared to a typical Central Plains supercell (like that BW13 simulated) precluded the development of a surface LFCB which behaved like that in BW13. With minimal surface cooling as a result of melting graupel/hail (not shown), there was no significant diabatic cooling gradient within the Monroe Supercell's precipitation region, leading to a rather uniform cold pool. While the LFCB was not explicitly related to hail production, that may have been overlooked due to the fact that the overwhelming majority of Central Plains supercells capable of producing tornadoes (and demonstrating the structure seen in simulations) produce a notable concentration of hail, if not at the surface then at the very least aloft.

Once the LFCB developed at 2340 UTC, the triple point between the LFCB, eastward—FFCB, and RFGF was located underneath the main low-level supercell updraft, consistent with simulations (BW13; Schueth et al. 2021). As the main low-level updraft occluded due to surging cold air from the forward flank, the eastward—FFCB began rotating counter-clockwise and maintained its connection to the RFGF even after the main low-level updraft at 2340 UTC fully occluded by 2355 UTC, consistent with both simulations and observations (BW13; Betten et al., 2018; Schueth et al., 2021).

6.4. The Streamwise Vorticity Current

Enhanced regions of streamwise vorticity were observed in the Monroe supercell from as early as 2315 UTC through the end of the Monroe Supercell Analysis Period (0005 UTC). Only at 2340 UTC and 2345 UTC (Figures 25 and 27, respectively) did the enhanced streamwise vorticity appear as a “persistent tube” of an SVC along the cool side of the eastward—FFCB (Orf et al. 2017). Unlike the simulations (Orf et al. 2017; Schueth et al. 2021) and observations of SVC’s in Central Plains supercells (Schueth et al. 2021; Murdzek et al. 2020), where the SVC persisted for at least 30 minutes, the SVC of the Monroe Supercell by contrast only lasted a maximum of 15 minutes, and a minimum of five minutes. However, the mechanisms by which the Monroe supercell's SVC developed, and how it influenced the storm, appear to be aligned previously modeled and observed SVC behavior.

A well-defined rotor-like circulation was apparent along the eastward—FFCB at 500 m—750 m AGL, co-located with both horizontal confluence and an intense and compact low-level maximum of streamwise vorticity (Figure 31e). The main supercell low-level updraft extends eastward along the west—east oriented FFCB at 2340 UTC (Figure 25b), likely a result of cross-FFCB horizontal convergence and the baroclinically-induced rotor-like circulation. This aligns with the horizontal stretching that also plays a role in the enhancement of streamwise vorticity along the SVC (Schueth et al. 2021). While both horizontal stretching and baroclinic-generation via the solenoidal mechanism were apparent, the relative importance of each remained undetermined, as a vector vorticity budget calculation (being outside the scope of this project) was not performed.

The SVC tracked along the eastward—FFCB directly into the main supercell updraft (Figure 25b at 75.5 km E, 48.5 km N), where it was then tilted into vertical vorticity, intensifying the low and mid-level mesocyclones. The intensification of the storm at 2340 UTC was correlated with the establishment of an SVC feeding the main low-level updraft at that time, consistent with the observed importance of baroclinically-generated vorticity in the forward-flank for low-level mesocyclone development (Markowski et al. 2012a,b). While it was shown that none of the air which traversed the SVC was ingested by the low-level tornado-cyclone (Figure 38), tornadogenesis at 2340 UTC was coincident with the SVC's development and the related intensification of the Monroe supercell, consistent with Orf et al. (2017). We hypothesize that the intensification of the main low-level supercell updraft, a direct result of its ingestion of and tilting of enhanced low-level streamwise vorticity from the SVC, led directly to the intensification of the southern RFD, which we believe played a critical role in tornadogenesis (see section 6.8).

As cold air from the forward-flank undercut the SVC and occluded the main low-level updraft, both the SVC and the Monroe supercell weakened. The alignment of the eastward—FFCB, and SVC, feeding parcels into the main low-level updraft was driven by storm-relative northeasterly winds in the forward-flank cold pool advecting the cold pool southward to create the sharp baroclinic boundary. Unlike the previous SVC simulations and observations, which featured a quasi-steady state boundary, the SVC for the Monroe supercell was transient as it was along the leading edge of the southward-gusting cold pool. The Monroe supercell SVC also featured a consistent enhancement of low-level vertical vorticity leading into the main low-level updraft. While our temporal and spatial resolution is insufficient to directly compare this to the "parade of vortices" seen in high resolution simulations (Orf et al. 2017; Schueth et al. 2021), the broad expanse of consistently positive vertical vorticity does differ from previous observed SVC's in a few select cases, where the SVC showed little tendency for positive vertical vorticity (Murdzek et al. 2020). Some of this difference may be due the differences in analysis techniques or spatial resolution of available data, as well as physical differences between SVC characteristics of different storms. A larger inventory of observed SVC's will be necessary to determine different modes of SVC, or if the Monroe supercell SVC would classify as "unusual" compared to other supercells.

6.5. Sources of low-level vorticity for the tornado-cyclone

Trajectories into the low-level tornado-cyclone at 2340 UTC revealed two main pathways: An arc through the inflow notch and RFGF, approaching the tornado-cyclone from the north and west (2/3^{rds} of trajectories), and direct ingestion from the southeasterly inflow region (1/3rd of trajectories) (Figure 34). This was consistent with two of the three parcel pathways to the low-level mesocyclone described in BW13, with the only missing pathway being parcels which originate higher aloft and descend down through the RFD. The importance of the RFD in tornadogenesis in literature has been tied to baroclinically-generated streamwise vorticity tilting into vertical vorticity due to parcel descent, but at 2340 UTC only two of the nine tornado-cyclone parcels experienced descent behind the RFGF, and the descent they experienced was only on the order of –1ms^{-1} over roughly two minutes (Figure 34). Combined with the RFGF featuring only weak baroclinity (only ~1 K over a few hundred meters near the surface, Figures 25e and 26), and the lack of enhanced streamwise vorticity analyzed along it, we concluded that the RFD was not contributing significant near-surface vertical vorticity to the tornado-cyclone.

The non-tornadic Northern low-level mesocyclone at 2340 UTC trajectory ensemble included multiple parcels that simultaneously grew positive vertical vorticity while undergoing descent (Figure 35). These parcels, particularly the northern most one of the envelope, appeared to generate intense low-level anti-streamwise vorticity near its time of descent near the triple point of the RFGF, eastward—FFCB, and LFCB, in a process consistent with simulations, observations, and theory (BW13; Markowski et al. 2008). And yet, the Northern low-level mesocyclone was not tornadic. Trajectories for the remnant tornado-cyclone at 2345 UTC do show this downdraft mechanism along the RFGF generating positive low-level vertical vorticity prior to the parcels arriving at the remnant tornado-cyclone (Figure 36, time –360s to –300s). However, at this time, the tornado had already been ongoing for several minutes, and, due to the wide spacing of damage indicators and weaker analyzed low-level vertical vorticity, may have dissipated by this time. As discussed previously, however, (see section 4.4.3) the apparent weakening of the tornado-cyclone may have been a result of our spatial grid resolution and the tightening of the circulation after tornadogenesis. Regardless, the baroclinic-generation of horizontal vorticity and its tilting by descent within the RFD did not appear to be a major contributor to the process of tornadogenesis seen at 2340 UTC.

The wind field and low-level tornado-cyclone trajectories at 2340 UTC (Figure 34) indicate that tornadogenesis occurred at a convergent horizontal shear zone between the south-

southeasterly inflow and north-northwesterly RFGF. This bares many similarities to the barotropic non-supercell tornadogenesis mechanism described by Wakimoto and Wilson (1989), where low-level vertical vorticity is generated by horizontal shear zones and then stretched under an updraft to tornado intensity. Interestingly, however, it is evident in Figure 34 that the full envelope of trajectories entering the convergent horizontal shear zone already possessed vertical vorticity on the order of 5—10 x 10^{-3} s^{-1} at least 10 minutes prior while they were in the open inflow sector. This closely resembles the 1994 Newcastle, TX F3 tornado observed during VORTEX, where ambient vertical vorticity values in a similar range were found to be in that supercell's inflow and were immediately stretched into the low-level mesocyclone once it reached the updraft (Ziegler et al. 2001; Wakimoto and Atkins 1996). In that particular case, analysis showed that the source of that inflow vertical vorticity was the outflow of the nearby Graham supercell, and therefore may have been resulting of baroclinity associated with that storm (Ziegler et al. 2001). No such neighboring convection was located to the south of the Monroe supercell during any analysis time before or after tornadogenesis.

Based on the storm-relative wind field and positioning of the trajectory origin points (Figure 35) we deemed it unlikely that these parcels traversed along the southward—FFCB or any significant portion of the southern anvil. With no potential baroclinic source available, we are left to conclude that the ambient vertical vorticity seen in the inflow developed barotropically within the broader mesoscale environment. This leaves us with two primary and one minor source of low-level vertical vorticity for tornadogenesis: Ambient barotropically-generated vertical vorticity in the mesoscale environment, vertical vorticity developed barotropically by the horizontal shear zone between the RFGF and inflow, and perhaps additionally a minor contribution by horizontal vorticity tilted into the vertical by the RFD.

While it may seem paradoxical for the non-supercell tornadogenesis process to generate a tornado for a supercell, barotropic processes may play a role in *some* supercellular tornadoes. In their discussion of non-supercell tornadogenesis, Wakimoto and Wilson (1989) speculated that the same barotropic processes they described may generate surface circulations along the flanking lines of supercells (e.g., as seen in Brandes 1977). The Monroe tornado developed at the far southern end of the hook echo, not at the triple point of the RFGF, eastward—FFCB, and LFCB where the main supercell updraft was, but rather at the "secondary" tornadogenesis point along the forward point of the gusting RFGF (Davies-Jones 2015), likely where the circulations noted by Wakimoto and Wilson (1989) would be most likely to develop. Once the tornado develops, its associated strong updraft may be sufficient to tilt and stretch streamwise vorticity close to the surface enough for it to be maintained. And in the case of supercells, where storm-scale processes, both baroclinic and barotropic, provide significant enhancements to streamwise vorticity, the horizontal vorticity necessary for tornado maintenance may then come from these storm-scale processes (Ziegler et al. 2001; Marquis et al. 2016). After the contraction of the tornado-cyclone at 2345 UTC (Figure 27, consistent with the contraction of non-supercell tornadoes (Wakimoto and Wilson 1989)), the later damage indicators (2—5), and in particular damage point "5" at 2355 UTC (Figure 29), were associated with enhanced streamwise vorticity leading into the disorganized low-level vortex. The association of enhanced streamwise vorticity in the inflow to the low-level mesocyclone with the known tornadic damage points supports the hypothesis that, once at least a weakly tornadic circulation develops, by either supercellular or non-supercellular mechanisms, streamwise vorticity enhanced by a combination of both baroclinic and barotropic storm-scale processes may be all that is necessary to maintain it. Notably, there was a relative lack of enhanced streamwise vorticity near the tornado-cyclone at

2345 UTC (Figure 27) compared to the latter times (Figure 29), and it was also from 2345 UTC through at least 2350 UTC where we hypothesized that, from the weaker, more compact tornado-cyclone to the wide spacing of damage points, that the Monroe tornado may have briefly lifted off the ground.

6.6. Non-diabatic sources of baroclinity

Although much of the discussion on baroclinically-generated horizontal vorticity in this thesis is centered on baroclinic boundaries which form as a result of diabatic cooling (i.e., the SVC – see section 6.4), a secondary, non-diabatic baroclinic boundary was evident in the mid-levels of the inflow boundary layer, most notably seen in the $\theta_v{}'$ fields at 2340 UTC at 250 m AGL (Figure 26) and 500 m AGL (Figure 25f). Surface $\theta_v{}'$ fields (Figure 25e) show minimal thermodynamic difference between the inflow and the surrounding environment unaffected by the storm. However, at 250 m and 500 m AGL, a broad region extending from the inflow notch to the south (to ~40 km y-distance on Figures 25f and 26) had $\theta_v{}'$ on the order of 0.5—1 K warmer than surrounding base environment (0 K $\theta_v{}'$ at 250 m AGL, -0.5 K $\theta_v{}'$ at 500 m AGL). This warm perturbation in the inflow is the result of the extensive weak low-level updrafts present along the inflow core (on the order of up to 1 m s^{-1}) gradually elevating warm $\theta_v{}'$ parcels following gently rising trajectories in the very low-level superadiabatic layer seen in the CRL measurements and Monroe soundings (see section 4.2). Although the low-level inflow updraft was weak, it was acting on these parcels for an extended period of time (on the order of ~10+ minutes) as they approached the supercell updraft, enabling a non-negligible ~1 K θ_v difference between the inflow core and base environment (i.e., the far southeast corner of Figure 25f). The low-level inflow updraft gradient between the inflow and southern anvil (e.g., Figure 23b) may represent the solenoidal circulation along which horizontal vorticity was generated, and this updraft may have been forced by a combination of storm-scale pressure perturbation forces and the thermodynamic forcing of the thermodynamic gradient itself.

Although weak when compared to the baroclinic boundary along which the SVC formed (see section 6.4), this inflow updraft-induced baroclinic boundary extended southward roughly along the southward—FFCB and anvil for upwards of 10 km, enabling potentially long parcel residence times along it which would result in notable streamwise vorticity generation via the baroclinic mechanism. Based on low-level parcel trajectories (see section 5), parcels entering both the tornado-cyclone and the northern low-level mesocyclone at 2340 UTC traveled along this inflow sector for a significant time period, and thus may have supported these features with low-level streamwise vorticity generated baroclinically along this non-diabatic baroclinic boundary. While the eastward—FFCB and FFCB at 2310 UTC were largely associated with regions of high surface rainwater mixing ratio (i.e., large amounts of diabatic cooling), the southward—FFCB, and south of it, at 2340 UTC and 2345 UTC were further removed from large amounts of inferred diabatic cooling (Figure 32). While it is likely that diabatic cooling contributed to the southward—FFCB, it, and the longer, broader baroclinic boundary along the eastern edge of the inflow region, likely were enhanced by the gradual rising of near-surface warm air and possibly also differential shading along the anvil edge (Markowski et al 1998).

6.7. Comparison to other Southeastern supercells

As discussed in section 1.3, multi-radar analyses of supercells in the Southeast US are rare, and simulations of storms within southeast-like environments are similarly uncommon. While the focus of this thesis is on the hypothesized origins of low-level rotation, this thesis also provides a unique set of observations of a southeastern supercell which will be detailed in the present subsection.

The Monroe supercell featured a forward-flank surface cold pool on the order 3.5 °C cooler than the background environment at 2340 UTC (not shown, but similar in magnitude and structure to the surface θ' field in Figure 25e). This overall weak cold pool is a consistent feature of supercells in the southeast, even non-tornadic storms (Wade and Parker 2021). In the context of Central Plains supercells, it has long been demonstrated that supercells with forward-flank cold pool deficits greater than 5 °C were less likely to produce tornadoes (Markowski et al. 2012a,b; Shabbott and Markowski 2006). The Monroe supercell's RFIS only featured a surface θ' gradient of ~1 K compared to the inflow, but this also was consistent with findings in Central Plains tornadic supercells that they featured θ values only slightly lower than their inflows, compared to nontornadic supercells which featured a greater RFD θ_v gradient (Markowski et al. 2002; Grzych et al. 2007; Hirth et al. 2008; Weiss et al. 2015; Markowski et al. 2018). While baroclinity in the Monroe supercell and within Southeastern supercells generally appeared to be weaker than their Central Plains counterparts, it does not appear to necessarily be an inhibiting factor to supercell tornadogenesis.

The mesoscale environment the Monroe supercell evolved in was not considered a High-Shear/Low-CAPE environment – From the Gilbert sounding, there was 1900 J kg^{-1} MLCAPE and ~40 kts 0—6 km shear, while most HSLC definitions use thresholds of ~1000 J kg^{-1} MLCAPE maximum and ~35 kts 0—6 km shear (Wade and Parker 2021). However, the thermodynamic profile of the Gilbert and other regional soundings demonstrated a Southeast-like environment, with a moist boundary layer, short/minimal EML, and a mid and upper level profile that was moist with meager lapse rates compared to classic Central Plains supercells (Figures 4, 6 and 7).

The Monroe supercell main updraft at 2340 UTC and 2345 UTC (Figure 45) featured a broad region of 10—15 m s^{-1} updraft extending 7—8 km AGL, modest and short compared to a typical Central Plains supercell. Based on the Gilbert sounding, the Equilibrium Level (EL) for the environment was 12.5 km AGL, and while high-CAPE storms typically carry intense updrafts up to their EL, the Monroe supercell updraft was nowhere near as deep as its EL, consistent with low-CAPE simulations (Wade and Parker 2021). The deepening of the updraft between 2340 UTCand 2345 UTC appears to be the result of an intense updraft pulse at 2340 UTC being carried upward by the updraft, which was also consistent with Wade and Parker (2021) and resembled the "weak evolution" described by Foote and Frank (1983). It should also be noted that the aforementioned updraft pulse was coincident with tornadogenesis and a general increase in intensity of the supercell, as well as with the development of an SVC (see section 6.4). The peak updraft speed at 2340 UTC and 2345 UTC was between 2—4 km AGL (the deep updraft pulse notwithstanding), consistent with both simulations and observations of low-CAPE supercells (Wade and Parker 2021; Murphy and Knupp 2013). Despite the relatively large amount of CAPE present in the environment, the Monroe supercell behaved more similarly to other low-CAPE southeastern supercells than to a typical Central Plains supercell due to the weak temperature lapse rates throughout the vertical profile consistent with typical southeast environments.

The tornado-cyclone of the Monroe supercell also behaved similarly to the low-CAPE simulations of Wade and Parker (2021). Parcels ingested by the tornado-cyclone at 2340 UTC rose to ~3 km AGL, and then their vertical motion slowed considerably (Figure 37). This is unlike high-CAPE storms, where parcels continue to accelerate up towards the EL due to positive buoyancy exceeding the downward dynamical pressure perturbation force above an intense low and mid-level mesocyclone (Wade and Parker 2021). However, the behavior of the Monroe tornado-cyclone trajectories did not perfectly match the low-CAPE simulations. After stagnating around 3.25 km AGL, parcel updraft speeds began to increase again in the final three minutes of the trajectory, with some parcels even increasing to updraft speeds greater than what they experienced in the low-level tornado-cyclone (Figure 37). We attributed this behavior to the tornado-cyclone trajectories entering the main supercell updraft aloft, as can be seen when comparing the position of these parcels towards the end of their trajectory to the deep-storm trajectories of parcels which passed through the SVC at 2340 UTC, and then were ingested by the main supercell updraft (Figure 38). The initial separation of the main supercell updraft and the updraft associated with the tornado-cyclone (as seen in Figure 25) had been noted in other radar-based supercell studies, even in the Central Plains (Betten et al. 2018; Dowell and Bluestein 2002; Ziegler et al. 2001; Brandes 1978). As discussed in section 6.4., the SVC likely enhanced the main supercell updraft by providing large values of streamwise vorticity that could be tilted and stretched. This enhancement may have enabled the main supercell updraft to at least partially overcome the downward pressure perturbation forces which would otherwise slow the updraft in the mid-levels, and ultimately enable it to capture the parcels ejecting from the top of the tornado-cyclone and continue to carry them upward. It is interesting to note that, while trajectories in both the high-CAPE and low-CAPE simulations of Wade and Parker (2021) arrived at their tornado-like vortices from the outflow sector (implying a baroclinic contribution to low-level vorticity), the high-CAPE simulation specifically produced a low-level feature bearing many similarities to an SVC, while the low-CAPE simulations did not (Wade and Parker 2021).

The Monroe supercell, while not technically within a HSLC environment, displayed many characteristics of a HSLC supercell due to its classic southeastern-type vertical thermodynamic profile. The differences noted above may be due to a lack of observational studies in the southeast or fundamental limitations of a simulation, but the larger CAPE and the presence of an SVC also provide a plausible physical explanation of the differences.

6.8. Comparison of the 2340 UTC hook echo to a Descending Reflectivity Core (DRC)

The downward-descending reflectivity feature which evolves into the southern tip of the hook echo and tornado-cyclone at 2340 UTC (see section 6.1) bears many similarities to the Descending Reflectivity Core (DRC) described by Rasmussen et al. (2006) in a few Central Plains supercell examples. The key difference between the feature which develops into the hook echo and tornado-cyclone and a DRC was the reflectivity threshold – Rasmussen et al. (2006) state that the core of the DRC must be at least 4 dB higher than the reflectivity corridor that connects it to the supercell. As evident in Figure 44a however, the reflectivity core of the DRC (~30 dBZ) gradually expanded and increased to the north before it reconnected with the main storm echo, seemingly contradicting this DRC requirement. Despite this difference, it might still be appropriate to describe this evolution as a DRC, or at least, functionally equivalent to a DRC, for a variety of physical and non-physical reasons.

The first consideration is semantic. As acknowledged by Rasmussen et al. (2006), their 4 dB threshold was chosen arbitrarily, with no particular physical process tied to that degree of reflectivity difference being a cutoff point for all DRC-like features. However, some degree of enhanced reflectivity in the core of the DRC is still necessary to separate it from other types of reflectivity appendages that may appear associated with a supercell. While the feature at 2340 UTC shows no such enhanced reflectivity, this may be a result of the limitations (and features) of this analysis. Unlike Rasmussen et al. (2006), which utilized single-radar, unsmoothed PPI scans, this analysis uses a multi-radar synthesis with a Barnes-interpolation smoothing scheme (see section 2.5). The smoothing process may have damped a short reflectivity minima of ~4 dB between possible DRC and the storm core, thereby artificially removing the DRC classification from this feature. It is also possible that our temporal resolution was insufficient to capture the DRC before further development of the hook echo increased its reflectivity between it and the DRC-like feature. As we have noted in our analysis of the Early Transient Mesovortex and the evolution of Monroe supercell surrounding tornadogenesis (see section 6.1), the storm occasionally undergoes significant evolution between the 5-minute analyses. Given that the tornado-cyclone develops in its entirety within the five minutes from 2335 UTC to 2340 UTC, it is not inconceivable that a DRC fulfilling the criteria set by Rasmussen et al. (2006) might have been present at, say, 2337 UTC, but no longer present at 2340 UTC due to the rapid evolution of the hook echo.

There may also be a physical explanation as to why the DRC-like feature did not meet the reflectivity criteria. In the cross section of the developing DRC-like feature at 2330 UTC (Figure 43c), a tail of 15—20 dBZ reflectivity extends down from the main supercell echo following the updraft down through low levels (with a distinct 10 dBZ echo associated with the low-level updraft below 1 km). This reflectivity pattern likely indicates the growth of raindrop-sized particles through the warm rain collision-coalescence process, which in turn is suggestive of a relatively low Cloud Condensation Nuclei (CCN) concentration (Ziegler 1988; Mansell and Ziegler 2013). Low CCN concentrations are typically associated with marine environments, and while northeastern Louisiana is not near the Gulf of Mexico, strong southerly low-level flow was present over the region, as seen in both the wind fields and observed moisture advection occurring (see section 3). It is therefore not out of the question that the environment that the Monroe supercell developed within could be characterized by somewhat marine-like low CCN concentrations. As this is an unusual environment for the Central Plains, most supercell observation and simulation studies occur within higher CCN concentration environments, and therefore do not feature as accelerated droplet growth via the warm rain processes in the lowest few kilometers AGL, and studies involving the DRC are no exception. While exploring the implications of the warm rain process on the evolution of the Monroe supercell was outside the scope of this thesis, we have deemed it plausible that it could influence the subtleties of a structure like a DRC. More research, both observational and simulation-based, on this topic is necessary.

Even though the hook echo structure at 2340 UTC did not exactly fit the DRC criteria set by Rasmussen et al. (2006), we hypothesize that the downward-development of reflectivity leading up to tornadogenesis and the development of the hook echo was functionally similar enough to a DRC to term it “DRC-like”. The effect of the Monroe supercell’s DRC-like feature (or, at least, the supercell evolution associated with the development of the DRC-like feature) appeared very similar to that of the 12 May 2010 Clinton, Oklahoma supercell observed during VORTEX2 – coincident with the rapid intensification and tornadogenesis of the tornado-cyclone at 2340 UTC, there was a notable updraft pulse to the north of the DRC-like feature (see section 6.2) as well as an initial separation from the tornado-cyclone from the main updraft before merging within five minutes after tornadogenesis (see section 6.7) (Markowski et al. 2018). While uncertainty remains about the exact role of the DRC in tornadogenesis, we found it intriguing how the DRC was closely coupled to tornadogenesis in a classic Central Plains supercell as well as the Monroe supercell, especially given our findings that ambient or horizontal-shear induced vertical vorticity may have been the most significant contributors to the low-level tornado-cyclone (see section 6.5).

6.9. DLA sensitivity analysis

The sensitivity of minor changes to the boundary layer thermodynamic profile was tested by running the DLA using only the Gilbert proximity sounding as the thermodynamic input (i.e., the Test DLA). The resulting θ_v' fields at the surface and 500 m AGL were compared to the Control DLA run with the boundary layer thermodynamic profile modified using the CRL results (Figure 46). The greatest departure of the CRL-modified thermodynamic profile from the Gilbert proximity sounding was in the lowest 400 m, so it was unsurprising that the greatest θ_v' magnitude changes were at the surface compared to the 500 m AGL analysis.

The overall structure of the Monroe supercell's cold pool at the surface was unchanged, and the surface boundaries determined via the Control DLA remained aligned with the θ_v' gradients of the Test DLA, with the only exception being a slight eastward shift in the southward—FFCB and slightly weaker cooling in the anvil region south of the eastward—FFCB. Of greater note, however, is the change in magnitude of the θ_v' gradient along the eastward—FFCB, particularly at the location of the SVC at the northern edge of the inflow notch. In the Control DLA, this θ_v' gradient was –2.5 K over 1 km, while in the Test DLA that same gradient was only –1.5 K over 1 km. The overall magnitude of the θ_v' within the cold pool in the Control DLA run nearly was twice that of the Test DLA (–4 K vs –2.5 K, respectively). This magnitude difference was tied closely to the ~2 K increase in θ for the CRL-modified profile versus the Gilbert sounding (see Figure 16). Although this change was at least partially driven by increasing the surface θ of the profile that the cold pool was being compared to, the end result of the strength of the baroclinic boundary along which the SVC developed is notable.

At 500 m AGL, where differences between the θ profile of the Gilbert proximity sounding and CRL-modified profile were minimal (see Figure 16), the magnitude of $\theta_v{}'$ within the cold pool and compressionally-warmed downdrafts was very similar across both versions of the DLA (Figure 46). Of particular note, however, was the neutral-to-warm $\theta_v{}'$ within the inflow sector of the Control DLA. In the test DLA, the inflow sector at both the surface and 500 m was neutral-to-cold, and the surface Control DLA had the same characteristics as well, contrasting the neutral-to-warm $\theta_v{}'$ at 500 m AGL in the Control DLA. This warming at 500 m AGL was likely the result of broad updrafts within the inflow sector carrying the high θ from the surface CRL-modified profile up in the boundary layer (see section 6.6). The warmer $\theta_v{}'$ not only indicates stronger baroclinity along the analyzed boundaries, but it may also represent unstable air feeding and reinforcing the supercell updraft in a way that was not seen in the test DLA.

Unsurprisingly, using only the Gilbert proximity sounding to initialize the thermodynamics of parcels in the DLA did not significantly change the overall structure of the $\theta_v{}'$field (Figure 46). However, the doubling of the surface $\theta_v{}'$ gradient across the eastward—FFCB and SVC as well as the increased gradient across the RFIS were notable, as these were two boundaries which, in our observations and in previous supercell studies, are regions where the baroclinic generation of vorticity is thought to be important for the development and maintenance of low-level mesocyclones and tornadoes. This thesis has demonstrated the usefulness of the DLA in identifying and characterizing these hard-to-sample boundaries, and future work can use the DLA to directly compute the amount of baroclinic vorticity generation in observed supercells. But this qualitative sensitivity analysis also demonstrated the importance of accurate near-storm inflow thermodynamic measurements within the boundary layer, and the importance of instruments like the CRL, which, as we have shown (see section 4.2), can accurately measure the thermodynamics of the boundary layer.

6.10. Limitations of the analyses presented

There were several limitations in both the data and the analysis procedures that should be emphasized, the most significant pertaining to the radar-analyzed wind field. For purposes of this analysis, the wind field was treated as "truth" in the absence of independent validating vector wind field observations. Although random radial velocity errors are strongly suppressed by the single-radar objective analysis which acts as a low-pass filter, any systematic or bias errors in the objectively analyzed radial velocities (e.g., radar beam effects in shear) would propagate through the analysis into the vertical velocity fields and to a much lesser extent the horizontal velocities. These propagated bias errors could in turn introduce errors in the vorticity fields, and ultimately the evolving finescale air trajectories and DLA fields.

Previous theoretical calculations of the velocity error standard deviation from synthesized dual-Doppler airborne radars have shown that vertical velocity errors decrease with decreasing distance to the radar target, and increase monotonically with height above ground during upward integration of the anelastic mass continuity equation (Wakimoto et al. 1998; Ziegler et al. 2001). During upward integration at a distance of 18 km from the target, the standard deviation of vertical velocity error increased from 2.5—3.0 m s^{-1} at 2 km AGL, to 6.1 m s^{-1} at 6 km AGL, and finally to 17.6 m s^{-1} at 14 km AGL. While the small standard deviation at 2 km AGL provides confidence in our low-level vertical velocity synthesis, the larger errors in the mid-levels are notable due to the relatively weak updraft of the Monroe supercell (~15—20 ms^{-1}). Although both Wakimoto et al. (1998) and Ziegler et al. (2001) assume a distance of 18 km from the radar for their error calculations, the magnitude of synthesized vertical velocity error in the Monroe supercell case would be considerably smaller since the P-3 flew notably closer (~10 km) to the storm.

Of greater significance, Ray et al. (1980) have shown that vertical velocity errors decrease during downward integration of anelastic mass continuity, the latter downward integration having been employed in the present study as described in section 2.5.3. Kessinger et al. (1987) showed that combinations of three or more radar storm observations via the over-determined dual-Doppler method (section 2.5.3) reduce the theoretical mid-storm maximum vertical velocity standard error deviation to roughly ~ 7 m s^{-1}, which compared to the maximum Monroe supercell updraft speed of ~ 30 m s^{-1} would correspond to an error to peak updraft ratio of ~ 23%. Additionally as described in section 2.5.3, the combination of the O'Brien (1970) column adjustment of vertical velocity (which imposes the ground and upper kinematic boundary conditions on vertical velocity) with the 3-D variational adjustment of vector velocity further reduces vertical velocity errors particularly at lower and middle levels. Our detailed analyses of vorticity, trajectories, and retrieved quantities were concentrated below 2 km AGL, where expected wind analysis errors due to random measurement error propagation are smallest.

A similar theoretical approach for the standard deviation of error for the horizontal wind components by Ziegler et al. (2001) showed that these were only ~1 m s^{-1}, and increased very slightly with height. The updraft speed errors of a ground-based 4-radar over-determined synthesis with downward integration were observed in a mountain thunderstorm using a sailplane flying at mid-levels (Ziegler et al. 1991). They found that the time-averaged difference between the radar-analyzed and sailplane-observed point updraft speed was ~2-3 m s^{-1} compared to a maximum ~ 18 m s^{-1} updraft magnitude (i.e., error to maximum updraft ratio of ~ 17%).

Ziegler et al. (1991) also found that the time-average difference between the microphysically retrieved and sailplane-measured cloud liquid water content was only ~ 0.2 g m^{-3} compared to the maximum cloud content of ~ 2 g m^{-3} (i.e., ~ 10% error). Attaining retrieval errors this small requires globally and locally accurate time-varying 3-D wind field analyses to accurately calculate the 3-D transport of heat and water substance, thus providing further inferential evidence of the accuracy of the multi-Doppler, over-determined radar wind synthesis method presented in section 2.5.3. While not insignificant, these calculations and observations provide confidence in our low and mid-level radar-analyzed updraft fields to have accurately captured the characteristics of the Monroe supercell most important for this analysis.

Another potential deficiency of the radar analysis is the lack of near-surface radial velocity measurements. While the TDRs and close range to KULM provide a substantial amount of radar observations as low as ~ 250 m AGL, no measurements are available in the range of 10-100 meters AGL. As a result, the surface radar-analyzed wind field has been determined from downward extrapolation of the smoothed, storm-scale horizontal wind profile below ~ 2 km AGL. The present radar-derived wind field therefore lacks the effects of both surface friction and vertically varying horizontal perturbation pressure forces on the surface level wind field, which in some simulations have been shown to potentially play a significant role in low-level mesocyclones and tornadogenesis (Schenkman et al. 2014; Roberts et al. 2020). Flournoy and Rasmussen (2021) hypothesize that the friction layer horizontal wind profile is strongly dominated by speed rather than directional shear, thus implying that the radar-derived near-surface winds in areas removed from strong horizontal perturbation pressure gradients (e.g., low-level mesocyclone inflow) may have somewhat high-biased wind speeds but relatively accurate wind direction.

However, there is still much uncertainty about the magnitude of the role played by surface friction compared to other tornadogenesis ingredients (Dahl 2015; Parker and Dahl 2015). Perhaps more crucially, this lack of very-low-level radar data may have prevented us from fully capturing the magnitude of low-level shear. Low-level shear on 6 April 2018, like many southeastern severe outbreak days, was significant as seen in both the Monroe soundings and Gilbert sounding hodographs (Figure 17). However, the radar-analyzed hodograph was consistently shorter in the lowest 1 km than these three measured hodographs at all analysis times (see section 4.3). The faster, more southwesterly surface wind in the radar analysis may be an indication that radar-analyzed surface winds were too similar to those at 250 m AGL. This not only drastically decreases the SRH of the radar-analyzed hodograph versus the soundings (Figure 18), but it may play a crucial role in the vertical and horizontal vorticity calculated, especially in the lowest 250 m AGL. This is particularly important because many of the trajectories we showed to interact with key storm features such as the tornado-cyclone spent considerable time within the lowest ~100 m AGL, and much of our analysis was predicated on accurate representations of horizontal and vertical vorticity along those trajectories (see section 6.5). As such, results and discussion centered on interpretations of trajectories below 250 m AGL should be considered more as hypotheses than conclusions. This limitation is fundamental to all radar observational studies (assuming comparable ranges from the networked radars to the storm) with the present-generation of observing technology and analysis techniques.

A final set of limitations, which have been referenced throughout this thesis but are reiterated here, are the analysis temporal and spatial resolutions. As we have demonstrated, the Monroe tornado-cyclone (and likely also the embedded tornado) developed rapidly, with the hook echo going from negligible reflectivity to 30+ dBZ with an associated intense low-level vortex within our five-minute analysis window. In addition, our analyses were unable to directly resolve the Monroe tornado due to our relatively large spatial grid spacing of 250 m compared to the narrow tornado (~50 yards). These limitations are especially evident from 2335 UTC to 2345 UTC, where we observe a DRC-like feature potentially serving as an instigator to tornadogenesis (see section 6.8) as well as a hypothesized lifting of the tornado by 2345 UTC due to a lack of damage assessment points and weak analyzed low-level vorticity (see section 6.5). And while we are confident that our trajectories accurately depict the different source regions for parcels which entered the low-level tornado-cyclone, due to the rapid evolution of the tornado-cyclone and DRC-like feature it is possible that the baroclinic mechanism for low-level vertical vorticity – the tilting of baroclinically-generated horizontal vorticity into vertical by the RFD – was understated (see section 6.5) Regardless, however, we are still confident in our result that barotropically-developed low-level vertical vorticity played a significant role in tornadogenesis.

Chapter 7: Conclusions

This thesis presents the first study to the author's knowledge that features time-dependent, 3-D multi-radar analyses and diabatic Lagrangian analysis (DLA) thermodynamic retrievals of a tornadic supercell in the Southeast US. An array of five radars – three ground-based and two airborne – sampled the tornadic Monroe supercell at close range for over an hour on 6—7 April 2018 during VORTEX-SE during the supercell's mature phase, the rapid tornadogenesis of an EF-0 tornado, and the supercell's eventual dissipation and merging with a developing MCS. Additionally, the triangularly-arrayed ground-based radars provided optimal triple-Doppler coverage of a supercell cluster and several bowing MCS segments at lower spatial resolution spanning the two hour period that contained the tornadic supercell. Research sounding teams in Gilbert and Monroe, along with measurements from the airborne CRL, combined with the radar-synthesized 3-D wind field and DLA to enable 4-D kinematic and thermodynamic analysis of the tornadic supercell.

The first and second main findings from this thesis are the apparent minimal role played by baroclinically-generated vorticity relative to barotropically generated vertical vorticity in tornadogenesis. Although as yet unconfirmed by vorticity-dynamical calculations, these are considered to be strong hypotheses due to the comprehensive combined evidence provided by airflow, thermodynamic, and microphysical histories of the storm-relative inflow trajectories. The first two findings are stated as follows:

1. Baroclinically generated horizontal vorticity only weakly contributed to the tilting-stretching generation of vertical vorticity by the low-level tornado-cyclonic updraft. Although some trajectories entering the base of the tornado-cyclone traversed along the weakly-baroclinic RFGF boundary, they were somewhat atypical of the general inflow

trajectories. Any baroclinically-generated vorticity entering the low-level tornado-cyclone during tornadogenesis was horizontal, as no parcels experienced a downdraft which could tilt their horizontal vorticity into the vertical prior to ingestion by the tornado-cyclone.

2. Barotropically-generated vertical vorticity at low levels likely contributed significantly to the stretching generation of vertical vorticity within the tornado-cyclonic updraft. The low-level vertical vorticity generated by the horizontal shear of the horizontal wind is hypothesized to be forced by a combination of: (1) the RFD impinging on the surface, generating strong perturbation pressure excess, divergence, accelerated northerly RFD outflow, and large vertical vorticies along the RFGF; and/or (2) differential perturbation pressure accelerations of the horizontal storm inflow, which produced relatively weak vertical vorticity in the inflow that could hypothetically provide sufficient initial circulation to be stretched to tornado-cyclonic intensity via the non-supercell tornadogenesis process.

While a baroclinic horizontal vorticity source was evident at low levels, low-level vertical vorticity generated barotropically by horizontal shears along the RFGF and spanning the ambient inflow environmental vertical vorticity were featured more prominently in low-level trajectories originating near the surface and entering the tornado-cyclone below ~250 m AGL during tornadogenesis (e.g., Wakimoto and Wilson 1989). This demonstrates an intriguing combination of both non-supercell and supercell tornadogenesis mechanisms. Robust along-trajectory vector vorticity-dynamical calculations can be used to explore this result further in follow-on research. Additional high-resolution observations of southeast supercells will be necessary to understand how the Monroe tornado fits within the mix of typical southeast tornadogenesis processes. For example, is the mix of classical and non-classical tornadogenesis mechanisms hypothesized for the Monroe supercell common in southeast storms? Or, in contrast, does this hypothesized hybrid mechanism only present in a small subset of southeastern storms of which the 6-7 April 2018 Monroe supercell was a member?

The third main finding relates to the observation of a transient streamwise vorticity current (SVC) in the Monroe supercell. The third main finding is as follows:

3. A streamwise vorticity current (SVC) was documented on the margins of the storm-scale cold pool, where the thermal gradient was aligned approximately parallel to the low-level forward-flank outflow that itself was directed towards the base of the main supercell updraft. The SVC was observed in the radar-analyzed wind field as a maximum of streamwise vorticity located along the DLA-retrieved thermodynamic FFCB, important evidence of a physical correlation between the radar-observed airflow and DLA-retrieved fields.

The SVC was located along southward-surging cold air from the storm core, and was only aligned to feed enhanced streamwise vorticity into the main supercell low-level updraft base for approximately 10 minutes. However, this transient phasing of the SVC with the main updraft coincided with a significant strengthening of the Monroe supercell, evident in the contemporaneous strong vertical motion pulse which deepened the storm's main updraft by nearly 4 km. While trajectories from the SVC remained ~2 km north of the tornado-cyclone, the development of the SVC coincided in time with tornadogenesis, consistent with previous model simulations (e.g., Orf et al. 2017). To the author's knowledge, this demonstration of an internal consistency between the radar-derived kinematic, thermodynamic, and vorticity-dynamical fields represents a unique new finding.

The fourth main finding of this thesis relates to the unanticipated impact of the dry-convectively unstable inflow boundary layer on baroclinic generation of horizontal low-level vorticity. The fourth finding is stated as follows:

4. Inflow trajectories entering the upper low-levels of the tornado-cyclone and northern low-level mesocyclone originated from above ~250 m AGL in the inflow sector, which contained non-diabatic baroclinity favorable for solenoidal generation of streamwise horizontal vorticity that could be subsequently tilted and stretched. The baroclinity was generated by a localized inflow plume of weak rising motion that vertically advected the unstable stratification of the CRL-profiled inflow boundary layer.

These first four findings together imply that some combination of barotropic and baroclinic forcing of vortex rotation acted in the Monroe supercell, with different relative magnitudes for the tornado-cyclone and the main supercell updraft. Baroclinity arose from a combination of classical diabatically-cooled air in the surface cold pool with a non-diabatic horizontally varying mesoscale vertical heat and water vapor fluxes in the storm's inflow (Pielke et al. 1991).

The fifth and final main finding of this thesis relates to the Monroe supercell's airflow morphology relative to other southeastern supercells in High-Shear/Low-CAPE (HSLC) environments. The fifth finding is stated as follows:

5. The Monroe supercell exhibited a more "pulse-like" multicellular (rather than steady-state unicellular) mesocyclone and updraft morphology. This morphological character is similar to a variant of the "Weak Evolution" storm scenario, distinct from the supercell scenario, as described by Foote and Frank (1983), and also bears resemblance to HSLC supercell simulations and (rather scarce) radar analyses in the southeast.

Despite a mesoscale environment featuring double the amount of MLCAPE of a classic HSLC environment, the Monroe supercell had a comparatively short and modest updraft which only briefly approached the deeper environmental equilibrium level. The pulse-like Monroe supercell's updraft included a distinct low- and mid-level core whose inflow air parcels processed vertically through the tornado-cyclone before losing all upward motion by 3 km AGL. This relatively shallow tornado-cyclonic updraft core was likely constrained by downward-directed pressure perturbation forces that dominated relatively weak mid-level buoyancy. In contrast, parcels passing from the SVC into the distinct main updraft core rose to the upper troposphere. The broad consistency between the Monroe supercell and simulated HSLC supercells was attributed to the meager mid- and upper-level lapse rates common in the majority of southeastern severe convective events, regardless of the fact that the Monroe supercell developed in an environment containing MLCAPE exceeding the conventionally acknowledged thresholds for HSLC environments.

This thesis has demonstrated the considerable potential of the diabatic Lagrangian analysis (DLA) and combined airborne and ground-based radar syntheses in observing supercell features such as the SVC and intensification of the tornado-cyclone leading to tornadogenesis. Additional observations of these features, both in the southeast and elsewhere, will provide a useful context through which to view the results presented herein. It is hoped that this thesis represents the first of many high-resolution, multi-radar analyses of southeastern severe convection, and that the present study will help lead to improved process understanding and forecast skill of severe convection within the unique southeastern environment.

References

Adlerman, E. J., K. K. Droegemeier, and R. P. Davies-Jones, 1999: A Numerical Simulation of Cyclic Mesocyclogenesis. *J. Atmos. Sci.*, **56**, 2045–2069. https://doi.org/10.1175/1520-0469(1999)056<2045:ANSOCM>2.0.CO;2

Anderson-Frey, A. K., Y. P. Richardson, A. R. Dean, R. L. Thompson, and B. T. Smith, 2019: Characteristics of Tornado Events and Warnings in the Southeastern United States. *Wea. Forecasting*, **34**, 1017–1034. https://doi.org/10.1175/WAF-D-18-0211.1

Ashley, W. S., 2007: Spatial and Temporal Analysis of Tornado Fatalities in the United States: 1880–2005. *Wea. Forecasting,* **22**, 1214–1228. https://doi.org/10.1175/2007WAF2007004.1

Barnes, S. L., 1964: A technique for maximizing details in numerical weather map analysis. *J. Appl. Meteor.*, **3**, 396–409.

Barnes, S. L., 1970: Some aspects of a severe, right-moving thunderstorm deduced from mesonetwork rawinsonde observations. *J. Atmos. Sci.*, **27**, 634–648, https://doi.org/10.1175/1520-0469(1970)027<0634:SAOASR>2.0.CO;2.

Beck, J., and C. Weiss, 2013: An Assessment of Low-Level Baroclinity and Vorticity within a Simulated Supercell. *Mon. Wea. Rev.*, **141**, 649–669. https://doi.org/10.1175/MWR-D-11-00115.1

Betten, D. P., M. I. Biggerstaff, and C. L. Ziegler, 2018: Three-Dimensional Storm Structure and Low-Level Boundaries at Different Stages of Cyclic Mesocyclone Evolution in a High-Precipitation Tornadic Supercell. *Advances in Meteorology*, *2018*, 1–24. https://doi.org/10.1155/2018/9432670

Biggerstaff, M. I., A. A. Alford, G. D. Carrie, and J. A, Stevenson, 2021: Hurricane Florence (2018): Long Duration Single- and Dual-Doppler Observations and Wind Retrievals During Landfall. *Geoscience Data Journal,* **00**, 1-15. https://doi.org/10.1002/gdj3.137

Bluestein, H. B., W. P. Unruh, D. C. Dowell, T. A. Hutchinson, T. M. Crawford, A. C. Wood, and H. Stein, 1997: Doppler Radar Analysis of the Northfield, Texas, Tornado of 25 May 1994. *Mon. Wea. Rev.*, **125**, 212–230. https://doi.org/10.1175/1520-0493(1997)125<0212:DRAOTN>2.0.CO;2

Bolton, D., 1980: The computation of equivalent potential temperature. *Mon. Wea. Rev.*, **108**, 1046–1053, https://doi.org/10.1175/1520-0493(1980)108<1046:TCOEPT>2.0.CO;2.

Brandes, E. A., 1977: Gust front evolution and tornado genesis as viewed by Doppler radar. *J. Appl. Meteor.*, **16**, 333–338, https://doi.org/10.1175/1520-0450(1977)016<0333:GFEATG>2.0.CO;2.

Brandes, E. A., 1978: Mesocyclone evolution and tornadogenesis: Some observations. *Mon. Wea. Rev.*, 106, 995–1011, https://doi.org/10.1175/1520-0493(1978)106<0995:MEATSO>2.0.CO;2.

Brandes, E. A., 1984: Relationships between radar-derived thermodynamic variables and tornadogenesis. *Mon. Wea. Rev.*, **112**, 1033–1052.

Buban, M., and C. Ziegler, 2016a: The formation of small-scale atmospheric vortices via horizontal shearing instability. J. Atmos. Sci., 73, 2061-2084, doi:10.1175/JAS-D-14-0355.1.

Buban, M., and C. Ziegler, 2016b: The formation of small-scale atmospheric vortices via baroclinic horizontal shearing instability. J. Atmos. Sci., 73, 2085-2104, doi:10.1175/JAS-D-14-0385.1.

Chmielewski, V. C., D. R. MacGorman, C. L. Ziegler, E. DiGangi, D. Betten, M. Biggerstaff, 2020: Microphysical and transportive contributions to normal and anomalous polarity subregions in the 29-30 May 2012 Kingfisher storm. Journal of Geophysical Research, 125, doi:10.1029/2020JD032384.

Cohen, R. A., and D. M. Schultz, 2005: Contraction rate and its relationship to frontogenesis, the Lyapunov exponent, fluid trapping, and airstream boundaries. *Mon. Wea. Rev.*, **133**, 1353–1369.

Dahl, J. M. L., 2015: Near-Ground Rotation in Simulated Supercells: On the Robustness of the Baroclinic Mechanism. *Mon. Wea. Rev.*, **143**, 4929–4942. https://doi.org/10.1175/MWR-D-15-0115.1

Dahl, J. M. L., M. D. Parker, and L. J. Wicker, 2014: Imported and Storm-Generated Near-Ground Vertical Vorticity in a Simulated Supercell. *J. Atmos. Sci.*, **71**, 3027–3051. https://doi.org/10.1175/JAS-D-13-0123.1

Davies-Jones, R. P., 1984: Streamwise vorticity: The origin of updraft rotation in supercell storms. *J. Atmos. Sci.*, **41**, 2991–3006, https://doi.org/10.1175/1520-0469(1984)041<2991:SVTOOU>2.0.CO;2.

Davies-Jones R. P., 1982: Observational and Theoretical Aspects of Tornadogenesis. *Intense Atmospheric Vortices*, Bengtsson L., Lighthill J., 175-189 https://doi.org/10.1007/978-3-642-81866-0

Davies-Jones, R. P., 2000: A Lagrangian Model for Baroclinic Genesis of Mesoscale Vortices. Part I: Theory. *J. Atmos. Sci.*, **57**, 715–736. https://doi.org/10.1175/1520-0469(2000)057<0715:ALMFBG>2.0.CO;2

Davies-Jones, R. P., 2015: A review of supercell and tornado dynamics. *Atmospheric Research*, **158–159**, 274–291. https://doi.org/10.1016/j.atmosres.2014.04.007

Davies-Jones, R. P., and H. Brooks, 1993: Mesocyclogenesis From a Theoretical Perspective. In C. Church, D. Burgess, C. Doswell, and R. Davies-Jones (Eds.), *Geophysical Monograph Series*, **79**, 105–114. American Geophysical Union. https://doi.org/10.1029/GM079p0105

Davies-Jones, R. P., and P. Markowski, 2013:. Lifting of Ambient Air by Density Currents in Sheared Environments. *J. Atmos. Sci.*, **70**, 1204–1215. https://doi.org/10.1175/JAS-D-12-0149.1

DiGangi, E., D. MacGorman, C. Ziegler, D. Betten, M. Biggerstaff, and C. Potvin, 2016: An overview of the 29 May 2012 Kingfisher supercell during DC3. *J. Geophys. Res.*, 14,316-14,343, doi: 10.1002/2016JD025690.

Dowell, D. C., and H. B. Bluestein, 2002: The 8 June 1995 McLean, Texas, Storm. Part I: Observations of Cyclic Tornadogenesis. *Mon. Wea. Rev.*, **130**, 2626–2648. https://doi.org/10.1175/1520-0493(2002)130<2626:TJMTSP>2.0.CO;2

Dowell, D. C., F. Zhang, L. J. Wicker, C. Snyder, and N. A. Crook, 2004: Wind and Temperature Retrievals in the 17 May 1981 Arcadia, Oklahoma, Supercell: Ensemble Kalman Filter Experiments. *Mon. Wea. Rev.*, **132**, 1982–2005. https://doi.org/10.1175/1520-0493(2004)132<1982:WATRIT>2.0.CO;2

Foote, G. B., and H. W. Frank, 1983: Case study of a hailstorm in Colorado. Part III: Airflow from triple-Doppler measurements. *J. Atmos. Sci.*, **40**, 686–707, https://doi.org/10.1175/1520-0469(1983)040,0686:CSOAHI.2.0.CO;2.

Flournoy, M. D., and E. N. Rasmussen, 2021: The influence of ground-relative flow and friction on near-surface storm-relative helicity. J. Atmos. Sci., 78, 2135-2142, doi: 10.1175/JAS-D-20-0320.1.

Gal-Chen, T., 1978: A method for the initialization of the anelastic equations: Implications for matching models with observations. *Mon. Wea. Rev.*, **106**, 587–606.

Grzych, M. L., B. D. Lee, and C. A. Finley, 2007: Thermodynamic Analysis of Supercell Rear-Flank Downdrafts from Project ANSWERS. *Mon. Wea. Rev.*, **135**, 240–246. https://doi.org/10.1175/MWR3288.1

Hane, C. E., and B. C. Scott, 1978: Temperature and pressure perturbations within convective clouds derived from detailed air motion information: Preliminary testing. *Mon. Wea. Rev.*, **106**, 654–661.

Hane, C., R. B. Wilhelmson, and T. Gal-Chen, 1981: Retrieval of thermodynamic variables within deep convective clouds: Experiments in three dimensions. *Mon. Wea. Rev.*, **109**, 564–576.

Hane, C. E., and P. S. Ray, 1985: Pressure and buoyancy fields derived from Doppler radar data in a tornadic thunderstorm. *J. Atmos. Sci.*, **42**, 18–35.

Hirth, B. D., J. L. Schroeder, and C. C. Weiss, 2008: Surface Analysis of the Rear-Flank Downdraft Outflow in Two Tornadic Supercells. *Mon. Wea. Rev.*, **136**, 2344–2363. https://doi.org/10.1175/2007MWR2285.1

Jorgensen, D. P., B. F. and Smull, 1993: Mesovortex circulations seen by airborne Doppler radar within a bow-echo mesoscale convective system. *Bull. Amer. Meteor. Soc.*, **74**, 2146–2157.

Jorgensen, D. P., C. L. Ziegler, E. N. Rasmussen, A. S. Goldstein, and A. A. Alford, 2017: Improvements to the NOAA P-3 airborne Doppler tail-mounted radar: Supercell observations from VORTEX-Southeast. Session 6A.2 (recorded presentation), 38th AMS Conference on Radar Meteorology, Chicago, IL.

Kessinger, C., P. Ray, and C. Hane, 1987: The Oklahoma squall line of 19 May 1977. Part I: A multiple Doppler analysis of con- vective and stratiform structure. *J. Atmos. Sci.*, **44**, 2840–2864.

Klemp, J. B., and R. Rotunno, 1983: A study of the tornadic region within a supercell thunderstorm. J. Atmos. Sci., **40**, 359–377.

Knupp, K. R., and Coauthors, 2014: Meteorological overview of the devastating 27 April 2011 tornado outbreak. ***Bull. Amer. Meteor. Soc.***, **95**, 1041–1062, https://doi.org/10.1175/BAMS-D-11-00229.1.

Koch, S. E., M. desJardins, and P. J. Kocin, 1983: An interactive Barnes objective map analysis scheme for use with satellite and conventional data. J. Appl. Meteor., 22, 1487–1503.

Lee, B. D., and R. B. Wilhelmson, 1997a: The numerical simulation of non- supercell tornadogenesis. Part I: Initiation and evolution of pretornadic misocyclone circulations along a dry outflow boundary. J. Atmos. Sci., 54, 32–60.

Lee, B. D., and R. B. Wilhelmson, 1997b: The numerical simulation of non- supercell tornadogenesis. Part II: Evolution of a family of tornadoes along a weak outflow boundary. *J. Atmos. Sci.*, **54**, 2387-2415.

Lemon, L. R., and C. A. Doswell, 1979: Severe thunderstorm evolution and mesocyclone structure as related to tornadogenesis. ***Mon. Wea. Rev.***, 107, 1184–1197, https://doi.org/10.1175/1520-0493(1979)107<1184:STEAMS>2.0.CO;2.

Lilly, D. K., 1986: The structure, energetics and propagation of rotating convective storms. Part II: Helicity and storm stabilization. *J. Atmos. Sci.*, **43**, 126–140

Majcen, M., P. M. Markowski, and Y. P. Richardson, 2008: Multipass objective analysis of Doppler radar data. *J. Atmos. Ocean. Tech.*, **25**, 1845–1858. https://doi.org/ 10.1175/2008JTECHA1089.1.

Mansell, E. R., and C. L. Ziegler, 2013: Aerosol Effects on Simulated Storm Electrification and Precipitation in a Two-Moment Bulk Microphysics Model. *J. Atmos. Sci.*, **70**, 2032–2050. https://doi.org/10.1175/JAS-D-12-0264.1

Marecal, V., D. Hauser, and F. Roux, 1993: The 12/13 January 1988 narrow cold-frontal rainband observed during MFDP/ FRONTS 87. Part II: Microphysics. J. Atmos. Sci., 50, 975– 998.

Markowski, P. M., J. M. Straka, and E. N. Rasmussen, 1998: Observations of low-level baroclinicity generated by anvil shadows. *Mon. Wea. Rev.*, **126**, 2942–2958.

Markowski, P. M., J. M. Straka, and E. N. Rasmussen, 2002: Direct surface thermodynamic observations within the rear-flank downdrafts of nontornadic and tornadic supercells. *Mon. Wea. Rev.*, **130**, 1692–1721. https://doi.org/10.1175/1520-0493(2002)130<1692:DSTOWT>2.0.CO;2

Markowski, P., Y. P. Richardson, and G. Bryan, 2014: The Origins of Vortex Sheets in a Simulated Supercell Thunderstorm. *Mon. Wea. Rev.*, **142**, 3944–3954. https://doi.org/10.1175/MWR-D-14-00162.1

Markowski, P., Y. P. Richardson, J. Marquis, R. Davies-Jones, J. Wurman, K. Kosiba, P. Robinson, E. N. Rasmussen, and D. Dowell, 2012b: The Pretornadic Phase of the Goshen County, Wyoming, Supercell of 5 June 2009 Intercepted by VORTEX2. Part II: Intensification of Low-Level Rotation. *Mon. Wea. Rev.*, **140**, 2916–2938. https://doi.org/10.1175/MWR-D-11-00337.1

Markowski, P., Y. P. Richardson, J. Marquis, J. Wurman, K. Kosiba, P. Robinson, D. Dowell, E. N. Rasmussen, and R. Davies-Jones, 2012a: The Pretornadic Phase of the Goshen County, Wyoming, Supercell of 5 June 2009 Intercepted by VORTEX2. Part I: Evolution of Kinematic and Surface Thermodynamic Fields. *Mon. Wea. Rev.*, **140**, 2887–2915. https://doi.org/10.1175/MWR-D-11-00336.1

Markowski, P., Y. P. Richardson, E. N. Rasmussen, J. Straka, R. Davies-Jones, and R. J. Trapp, 2008: Vortex Lines within Low-Level Mesocyclones Obtained from Pseudo-Dual-Doppler Radar Observations. *Mon. Wea. Rev.*, **136**, 3513–3535. https://doi.org/10.1175/2008MWR2315.1

Marquis, J., Y. P. Richardson, P. Markowski, D. Dowell, and J. Wurman, 2012: Tornado Maintenance Investigated with High-Resolution Dual-Doppler and EnKF Analysis. *Mon. Wea. Rev.*, **140**, 3–27. https://doi.org/10.1175/MWR-D-11-00025.1

Marquis, J., Y. P. Richardson, P. Markowski, D. Dowell, J. Wurman, K. Kosiba, P. Robinson, and G. Romine, 2014: An Investigation of the Goshen County, Wyoming, Tornadic Supercell of 5 June 2009 Using EnKF Assimilation of Mobile Mesonet and Radar Observations Collected during VORTEX2. Part I: Experiment Design and Verification of the EnKF Analyses. *Mon. Wea. Rev.*, **142**, 530–554. https://doi.org/10.1175/MWR-D-13-00007.1

Marquis, J., Y. P. Richardson, P. Markowski, J. Wurman, K. Kosiba, and P. Robinson, 2016: An Investigation of the Goshen County, Wyoming, Tornadic Supercell of 5 June 2009 Using EnKF Assimilation of Mobile Mesonet and Radar Observations Collected during VORTEX2. Part II: Mesocyclone-Scale Processes Affecting Tornado Formation, Maintenance, and Decay. *Mon. Wea. Rev.*, **144**, 3441–3463. https://doi.org/10.1175/MWR-D-15-0411.1

Markowski, P. M., T. P. Hatlee, and Y. P. Richardson, 2018: Tornadogenesis in the 12 May 2010 Supercell Thunderstorm Intercepted by VORTEX2 near Clinton, Oklahoma. *Mon. Wea. Rev.*, **146**, 3623–3650. https://doi.org/10.1175/MWR-D-18-0196.1

Mashiko, W., 2016: A Numerical Study of the 6 May 2012 Tsukuba City Supercell Tornado. Part I: Vorticity Sources of Low-Level and Midlevel Mesocyclones. *Mon. Wea. Rev.*, **144**, 1069–1092. https://doi.org/10.1175/MWR-D-15-0123.1

Miller, R. L., 2018: Kinematics, thermodynamics, and microphysics of the 25-26 June 2015 Kansas MCS during PECAN. M.S. thesis, University of Oklahoma, 154 pp., https://shareok.org/ handle/11244/299940.

Miller, R. L., Ziegler, C. L., and Biggerstaff, M. I., 2020: Seven-Doppler Radar and In Situ Analysis of the 25–26 June 2015 Kansas MCS during PECAN. *Mon. Wea. Rev.*, **148**, 211–240. https://doi.org/10.1175/MWR-D-19-0151.1

Murdzek, S. S., P. M. Markowski, and Y. P. Richardson, 2020: Simultaneous Dual-Doppler and Mobile Mesonet Observations of Streamwise Vorticity Currents in Three Supercells. *Mon. Wea. Rev.*, **148**, 4859–4874. https://doi.org/10.1175/MWR-D-20-0239.1

Murphy, T. A., and K. R. Knupp, 2013: An Analysis of Cold Season Supercell Storms Using the Synthetic Dual-Doppler Technique. *Mon. Wea. Rev.*, **141**, 602–624. https://doi.org/10.1175/MWR-D-12-00035.1

NOAA Nation Centers for Environmental Information (NCEI): Storm Events Database. Accessed Spring 2021. ncdc.noaa.gov/stormevents/eventdetails.jsp?id=744897

O'Brien, J. J., 1970: Alternative solutions to the classical vertical velocity problem. *J. Appl. Meteor.*, **9**, 197–203, https://doi.org/ 10.1175/1520-0450(1970)009,0197:ASTTCV.2.0.CO;2.

Orf, L., R. Wilhelmson, B. Lee, C. Finley, and A. Houston, 2017: Evolution of a Long-Track Violent Tornado within a Simulated Supercell. *Bull. Amer. Meteor. Soc.*, **98**, 45–68. https://doi.org/10.1175/BAMS-D-15-00073.1

Pielke, R. A., G. A. Dalu, J. S. Snook, T. J. Lee, and T. G. F. Kittle, 1991: Nonlinear Influence of Mesoscale Land Use on Weather and Climate. *J. Climate,* **4**, 1053—1069

Parker, M. D., and J. M. L. Dahl, 2015: Production of Near-Surface Vertical Vorticity by Idealized Downdrafts. *Mon. Wea. Rev.*, **143**, 2795–2816. https://doi.org/10.1175/MWR-D-14-00310.1

Rasmussen, E. N., J. M. Straka, M. S. Gilmore, and R. Davies-Jones, 2006: A Preliminary Survey of Rear-Flank Descending Reflectivity Cores in Supercell Storms. *Wea. Forecasting*, **21**, 923–938. https://doi.org/10.1175/WAF962.1

Ray, P. S., 1976: Vorticity and divergence fields within tornadic storms from dual- Doppler observations. *J. Appl. Meteor.*, **15**, 879–890, https://doi.org/10.1175/1520-0450(1976)015<0879:VADFWT>2.0.CO;2.

Ray, P. S., K. K. Wagner, K. W. Johnson, J. J. Stephens, W. C. Bumgarner, and E. A. Mueller, 1978: Triple-Doppler observations of a convective storm. *J. Appl. Meteor.*, **17**, 1201-1212.

Ray, P. S., J. J. Stephens, and K. W. Johnson, 1979: Multiple-Doppler radar network design. *J. Appl. Meteor.*, **18**, 706-710.

Ray, P. S., C. L. Ziegler, W. Bumgarner, and R. J. Serafin, 1980: Single- and multiple-Doppler radar observations of tornadic storms. *Mon. Wea. Rev.*, **108**, 1607–1625, https://doi.org/10.1175/1520-0493(1980)108<1607:SAMDRO>2.0.CO;2.

Ray, P., and K. Sangren, 1983: Multiple-Doppler radar network design. *J. Climate Appl. Meteor.*, **22**, 1444–1454.

Roberts, B., M. Xue, and D. T. Dawson, 2020: The Effect of Surface Drag Strength on Mesocyclone Intensification and Tornadogenesis in Idealized Supercell Simulations. *J. Atmos. Sci.*, **77**, 1699–1721. https://doi.org/10.1175/JAS-D-19-0109.1

Rotunno, R., 1981: On the evolution of thunderstorm rotation. *Mon. Wea. Rev.*, **109**, 577–586, https://doi.org/10.1175/1520-0493(1981)109<0577:OTEOTR>2.0.CO;2.

Rotunno, R., and J. Klemp, 1985: On the rotation and propagation of simulated supercell thunderstorms. *J. Atmos. Sci.*, **42**, 271–292, https://doi.org/10.1175/1520-0469(1985)042<0271:OTRAPO>2.0.CO;2.

Roux, F., 1985: Retrieval of thermodynamic fields from multiple-Doppler radar data using the equations of motion and the thermodynamic equation. *Mon. Wea. Rev.*, **113**, 2142– 2157.

Rutledge, S. A., and P. V. Hobbs, 1984: The mesoscale and mi- croscale structure and organization of clouds and precipitation in midlatitude cyclones. XII: A diagnostic modeling study of precipitation development in narrow cold-frontal rainbands. *J. Atmos. Sci.*, **41**, 2949–2972.

Schenkman, A. D., M. Xue, and M. Hu, 2014: Tornadogenesis in a High-Resolution Simulation of the 8 May 2003 Oklahoma City Supercell. *J. Atmos. Sci.*, **71**, 130–154. https://doi.org/10.1175/JAS-D-13-073.1

Schueth, A., C. Weiss, and J. M. L. Dahl, 2021: Comparing Observations and Simulations of the Streamwise Vorticity Current and the Forward Flank Convergence Boundary in a Supercell Storm. *Mon. Wea. Rev.*, **1**. https://doi.org/10.1175/MWR-D-20-0251.1

Shabbott, C. J., and P. M. Markowski, 2006: Surface In Situ Observations within the Outflow of Forward-Flank Downdrafts of Supercell Thunderstorms. *Mon. Wea. Rev.*, **134**, 1422–1441. https://doi.org/10.1175/MWR3131.1

Sherburn, K. D., and M. D. Parker, 2019: The Development of Severe Vortices within Simulated High-Shear, Low-CAPE Convection. *Mon. Wea. Rev.*, **147**, 2189–2216. https://doi.org/10.1175/MWR-D-18-0246.1

Smith, B. T., R. L. Thompson, J. S. Grams, C. Broyles, and H. E. Brooks, 2012: Convective Modes for Significant Severe Thunderstorms in the Contiguous United States. Part I: Storm Classification and Climatology. *Wea. Forecasting*, **27**, 1114–1135. https://doi.org/10.1175/WAF-D-11-00115.1

Snyder, C., and F. Zhang, 2003: Assimilation of Simulated Doppler Radar Observations with an Ensemble Kalman Filter*. *Mon. Wea. Rev.*, **131**, 1663–1677. https://doi.org/10.1175//2555.1

Wade, A. R., and M. D. Parker, 2021: Dynamics of Simulated High-Shear, Low-CAPE Supercells. *J. Atmos. Sci.*, **78**, 1389–1410. https://doi.org/10.1175/JAS-D-20-0117.1

Wakimoto, R. M., and J. W. Wilson, 1989: Non-supercell tornadoes. *Mon. Wea. Rev.*, **117,** 1113–1140.

Wakimoto, R. M., and N. T. Atkins, 1996: Observations of the origins of rotation: The Newcastle tornado during VORTEX 94. *Mon. Wea. Rev.*, **124,** 384–407.

Wakimoto, R. M., C. Liu, and H. Cai, 1998: The Garden City, Kansas, Storm during VORTEX 95. Part I: Overview of the Storm's Life Cycle and Mesocyclogenesis. *Mon. Wea. Rev.*, **126**, 372–392. https://doi.org/10.1175/1520-0493(1998)126<0372:TGCKSD>2.0.CO;2

Walko, R. L., 1993: Tornado spin-up beneath a convective cell: Required basic structure of the near-field boundary layer winds. In C. Church, D. Burgess, C. Doswell, and R. Davies-

Jones (Eds.), *Geophysical Monograph Series* **79**, 89–95. American Geophysical Union. https://doi.org/10.1029/GM079p0089

Wang, Z., P. J. Wechsler, N. Mahon, D. Wu, B. Liu, M. Burkhart, B. Glover, W. Kuestner, W. Welch, & A. Thomson, 2016: Airborne Raman Lidar and its Applications for Atmospheric Process Studies. *EPJ Web of Conferences*, **119**, 09002. https://doi.org/10.1051/epjconf/201611909002

Weiss, C. C., D. C. Dowell, J. L. Schroeder, P. S. Skinner, A. E. Reinhart, P. M. Markowski, & Y. P. Richardson, 2015: A Comparison of Near-Surface Buoyancy and Baroclinity across Three VORTEX2 Supercell Intercepts. *Mon. Wea. Rev.*, **143**, 2736–2753. https://doi.org/10.1175/MWR-D-14-00307.1

Wicker, L. J., and R. B. Wilhelmson, 1995: Simulation and analysis of tornado development and decay within a three-dimensional supercell thunderstorm. *J. Atmos. Sci.*, **52**, 2675–2703, https://doi.org/10.1175/1520-0469(1995)052<2675:SAAOTD>2.0.CO;2.

Wurman, J., and S. Gill, 2000: Finescale Radar Observations of the Dimmitt, Texas (2 June 1995), Tornado. *Mon. Wea. Rev.*, **128**, 2135–2164. https://doi.org/10.1175/1520-0493(2000)128<2135:FROOTD>2.0.CO;2

Ziegler, C., L., 1985: Retrieval of thermal and microphysical variables in observed convective storms. Part I: Model development and preliminary testing. J. Atmos. Sci., 42, 1487–1509.

Ziegler, C., L., 1988: Retrieval of thermal and microphysical variables in observed convective storms. Part II: Sensitivity of cloud processes to variation of the microphysical parameterization. J. Atmos. Sci., 45, 1072–1090.

Ziegler, C. L., D. R. MacGorman, J. E. Dye, and P. S. Ray, 1991: A model evaluation of noninductive graupel-ice charging in the early electrification of a mountain thunderstorm. *Journal of Geophysical Research*, **96**, 12833. https://doi.org/10.1029/91JD01246

Ziegler, C. L., E. N. Rasmussen, T. R. Shepherd, A. I. Watson, and J. M. Straka, 2001: The evolution of low-level rotation in the 29 May 1994 Newcastle–Graham, Texas, storm complex during VORTEX. *Mon. Wea. Rev.*, **129**, 1339–1368. https://doi.org/10.1175/1520-0493(2001)129<1339:TEOLLR>2.0.CO;2

Ziegler, C. L., 2013a: A diabatic Lagrangian technique for the analysis of convective storms. Part I: Description and validation via an observing system simulation experiment. *J. Atmos. Oceanic Technol.*, **30**, 2248–2265. https://doi.org/10.1175/JTECH-D-12-00194.1

Ziegler, C. L., 2013b: A diabatic Lagrangian technique for the analysis of convective storms. Part II: Application to a radar-observed storm. *J. Atmos. Oceanic Technol.*, **30**, 2266–2280. https://doi.org/10.1175/JTECH-D-13-00036.1

Ziegler, C. L., T. Murphy, K. Elmore, M. I. Biggerstaff, Z. Wang, E. N. Rasmussen, D. P. Jorgensen, and A. A. Alford, 2018: Kinematics, thermodynamics, and microphysics of the tornadic 13-14 April 2018 Calhoun, La supercell during VORTEX-SE. Session 8.4 (recorded presentation), 29th AMS Conference on Severe Local Storms, Stowe, VT.

Appendix A: Tables

Radar	Wavelength	Beam Width	Volume Scan Time
KULM	10 cm (S-band)	1^o	~ 4.5 minutes
SR2	5 cm (C-band)	1.5^o	~ 4.5 minutes
SR3	5 cm (C-band)	1.5^o	~ 4.5 minutes
TDR-Aft	3 cm (X-band)	2^o	~ 3-5 minutes
TDR-Fore	3 cm (X-band)	2^o	~ 3-5 minutes

Table 1. Wavelength, beam width, and single-volume scan time for each of the five radars.

Analysis Time (UTC)	**KULM**	**SR2**	**SR3**	**TAFT**	**TFOR**
2230	223002-223421	223006-223435	223008-223434		
2250	225002-225421	225006-225434	225006-225434		
2255	225502-225921	225506-225934	225506-225934	224903-225534	224903-225535
2300	230002-230421	230006-230435	230006-230434	225842-230148	225842-230149
2305	230507-230935	230505-230935	230505-230935	230448-230827	230448-230828
2310	231002-231421	231007-231435	231005-231435	230448-230828*	230448-230829*
2315	231502-231921	231507-231935	231506-231904	231154-231546	231154-231547
2320	232002-232421	232007-232434	232013-232441	231933-232320	231933-232321
2325	232502-232921	232506-232934	232506-232934	231933-232321*	231933-232322*
2330	233002-233421	233006-233434	233006-233434	232657-232944	232657-232945
2335	233502-233921	233506-233934	233506-233934	233242-233752	233242-233753
2340	234002-234421	234006-234434	234006-234434	234129-234500⟨	234129-234501⟨
2345	234502-234921	234510-234940	234507-234935	234129-234501	234129-234502
2350	235002-235421	235006-235434	235006-235436	234902-235314	234902-235315
2355	235502-235921	235523-235951	235507-235935	234902-235315*	234902-235316*
0000	000002-000421	000023-000450	000007-000435	235630-000002	235630-000003
0005	000502-000921	000510-000938	000507-000935	000203-000640	000203-000641
0010	001002-001421	001006-001434	001006-001434		
0030	003002-003421	003006-003434	003007-003435		

Table 2. The time of the radar volumes for all five radars for each analysis time. Note that TDR volumes are defined by the length of the leg. Stars denote TDR volumes which were used a second time due to their proximity to two different analysis times.

Variable Name	Quantity measured (source)
AltGPS.1	Altitude, MSL (pure GPS altitude from the RINU-G intertials)
AltGPS.3	Altitude, MSL (from Novatel)
AltGPS.4	Altitude, MSL (from Novatel)
AltI-GPS.1	Altitude, MSL (blended GPS altitude from the RINU-G inertials)
AltI-GPS.2	Altitude, MSL (blended GPS altitude from the RINU-G inertials)
PSM.1	Air pressure (from measured wingtip static pressure)
TA.d	Air temperature (ambient temperature derived from corrected static pressure and corrected dynamic pressure measurements)
TD.c	Dewpoint temperature (corrected dewpoint temperature derived from measured frostpoint temperature and derived vapor pressure)
MR.d	Water vapor mixing ratio (derived from measured corrected static pressure and derived vapor pressure)

Table 3. List of the flight-level dataset, recorded at 1 Hz frequency, used in this study from the Automated Aircraft Mission Planning System (AAMPS) data system on board the P-3 aircraft. Note that the five different altitude measurements were averaged together to create the average altitude used in the analysis.

	Derived Pressure Profile	Sounding Pressure Profile
Pressure	965.73mb	963.33mb
Potential Temperature	295.40 K	295.61 K
Virtual Potential Temperature	297.87 K	298.08 K
Relative Humidity	92.83%	92.60%
Dewpoint Temperature	18.12 C	18.08 C

Table 4: A sensitivity test comparing the thermodynamic calculations using the hypsometric-derived vertical pressure profile (middle) and the sounding-measured vertical pressure profile (right) with the CRL measured temperature and water vapor mixing ratio. The random data selected came from time 99 seconds of Leg 4, at a height of 360 m MSL. The effect of the ~2.5 mb difference between the two vertical pressure profiles is negligible on the thermodynamic calculations. For consistency, the hypsometric-derived vertical pressure profile is used in all analyses in this thesis.

Time (UTC)	Location of Launched Soundings
1200z	Shreveport, LA; Jackson, MS
1700z	Shreveport, LA
1800z	Jackson, MS
2030z	Monroe, LA (research sounding)
2033z	Gilbert, LA (research sounding)
2100z	Shreveport, LA; Jackson, MS
2231z	Monroe, LA (research sounding)
2234z	Gilbert, LA (research sounding)
2300z	Little Rock, AR; Jackson, MS

Table 5: The location and time of all regional operational and research soundings.

	Mean Wind Difference (m/s)	Standard Deviation of Wind Difference (m/s)
Gilbert 2234z Sounding	3.12	0.72
Radar-Derived, on Fine Grid domain	2.14	0.91
Radar-Derived, on 15km x 15km domain	1.85	0.78

Table 6: The average and standard deviation of the differences of 1 km AGL wind from the wind measured by the P-3 from 2255 UTC – 0005 UTC. The same radar-derived wind procedure as described in section 2.6 was performed on the Fine Grid domain (see section 2.5.2), which includes the Monroe Supercell mesocyclone. The smaller 15 km x 15 km grid had less error and spread of error from the P-3 measurements, and so that was the grid used for our radar-derived hodographs.

Surface Station (Location)	Grouping	Times Data is recorded (UTC)
KMLU (Monroe Regional Airport)	Northern	2255, 2300, 2305, 2310, 2315, 2320, 2325, 2330, 2335, 2340, 2345, 2350, 2355, 0000, 0002, 0005
KBQP (Morehouse Memorial Airport-BQP)	Northern	2255, 2315, 2335, 2355
KRSN (Ruston Regional Airport)	Northern	2255, 2315, 2335, 2355
KTVR (Yerger Landing Strip, Tallulah, LA)	Northern	2253, 2305, 2313, 2320, 2327, 2333, 2342, 2351, 2353
KVKS (Vicksburg Municipal Airport, MS)	Northern	2255, 2315, 2335, 2355
KAEX (Alexandria Esler Regional Airport)	Southern	2253, 2341, 2353
KESF (Alexandria International Airport)	Southern	2253, 2334, 2353
KIER (Natchitoches Regional Airport)	Southern	2255, 2315, 2335, 2355
KHEZ (Natchez-Adams County Airport, MS)	Southern	2256, 2356

Table 7: Surface station name and location (all locations in Louisiana unless otherwise specified), along with their grouping classification based on latitude and times at which they recorded data during the Monroe Supercell Analysis period (2255 UTC – 0005 UTC). All stations are WBAN with the exception of Monroe, which is an ASOS.

Domain Name	Analysis Times (UTC)	Domain Size	Smoothing Parameter (Kappa)
Big Grid	2230, 2250 - 0010, 0030	145km x 105km x 14km	0.44
Nested Grid	2255 - 0005	120km x 80km x 14km	0.132
Fine Grid	2255 - 0005	30km x 30km x 14km	0.044
Merged Nested Grid	2255 - 0005	120km x 80km x 14km	0.132, 0.044

Table 8: The analysis times, size, and smoothing parameter of each objectively analyzed grid domain. All domains have grid spacings of 250 m x 250 m x 250 m in all direction, and also have the same grid levels. The Merged Nested Grid is comprised of the Fine Grid placed within the larger Nested Grid.

Analysis Time (UTC)	Disallowed Radar Combinations
2230	SR2—SR3
2250	KULM—SR2
2255	KULM—SR2; KULM—TFOR
2300	KULM—SR2; KULM—TAFT
2305	KULM—SR2
2310	KULM—SR2
2315	KULM—SR2; KULM—TAFT; KULM—SR2—TAFT
2320	KULM—SR2; KULM—SR2—TAFT
2325	KULM—SR2
2330	KULM—SR2; KULM—SR3; KULM—TAFT; KULM—SR2—TAFT
2335	KULM—SR2; KULM—SR2—TAFT; KULM—SR3—TAFT
2340	KULM—SR2; KULM—SR3; KULM—SR2—TFOR
2345	KULM—SR2; KULM—SR3; KULM—SR2—TFOR
2350	KULM—SR2; KULM—SR3
2355	KULM—SR2; KULM—SR3
0000	KULM—SR2; KULM—SR3; KULM—TAFT
0005	KULM—SR2; KULM—SR3
0010	KULM—SR2; KULM—SR3
0030	KULM—SR2; KULM—SR3

Table 9: All disallowed dual and triple-Doppler combinations at each analysis time.

Analysis Time (UTC)	R_min (km)	R_max (km)	Elevation_Rmin (degrees)	Elevation_Rmax (degrees)
2255	40	75	3	5
2300	40	75	3	5
2305	40	75	3	5
2310	40	75	3	5
2315	45	75	3	5
2320	45	75	3	5
2325	45	75	3	5
2330	40	75	4	6
2335	35	75	4	6
2340	35	75	4	6
2345	30	75	5	7
2350	30	75	5	7
2355	30	75	7	9
0000	30	75	7	9
0005	30	75	10	12

Table 10: Range and elevation restriction parameters for SR3 for the Merged Nested Grid analysis. R_min represents the radius range within which radar data at or below the elevation tilt of Elevation_Rmin is masked, and R_max represents the radius range within the data at or below the elevation tilt of Elevation_Rmax is masked. For this study, R_max was set to be the maximum range of the SR's data.

Analysis Time (UTC)	R_min (km)	R_max (km)	Elevation_Rmin (degrees)	Elevation_Rmax (degrees)
2255	75	75	2	4
2300	75	75	2	4
2305	70	75	2	4
2310	70	75	2	4
2315	65	75	3	5
2320	60	75	3	5
2325	60	75	3	5
2330	55	75	3	5
2335	50	75	3	5
2340	45	75	3	5
2345	45	75	3	5
2350	40	75	3	5
2355	40	75	3	5
0000	40	75	4	6
0005	40	75	4	6

Table 11: Same as Table 10, but for SR2.

Appendix B: Figures

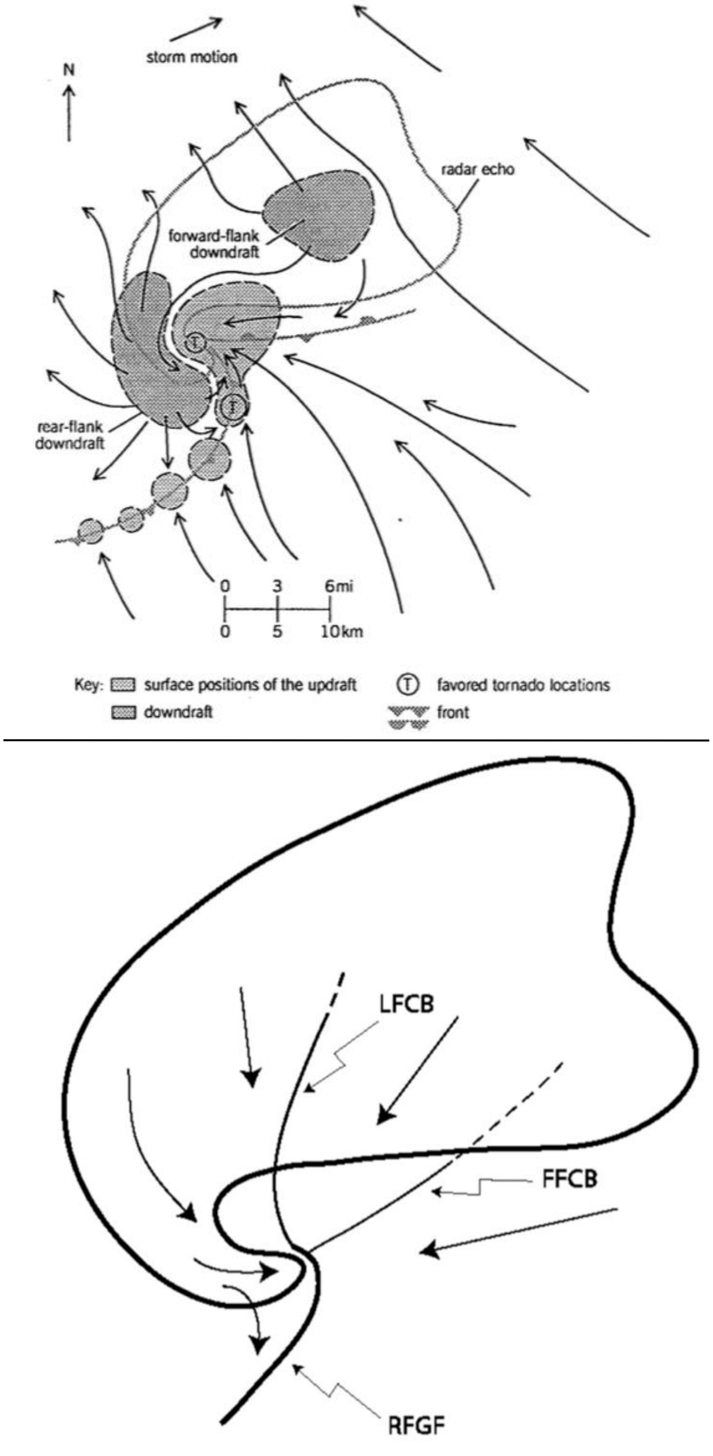

Figure 1. The conceptual model of the updraft, downdraft, and gust fronts of a supercell with favored locations for tornadoes (circled T) (top) (Davies-Jones 2015, adapted from C. Doswell). The conceptual model of the FFCB, LFCB, and RFGF locations with storm-relative streamlines in a classic steady-state supercell (bottom) (Beck and Weiss 2013).

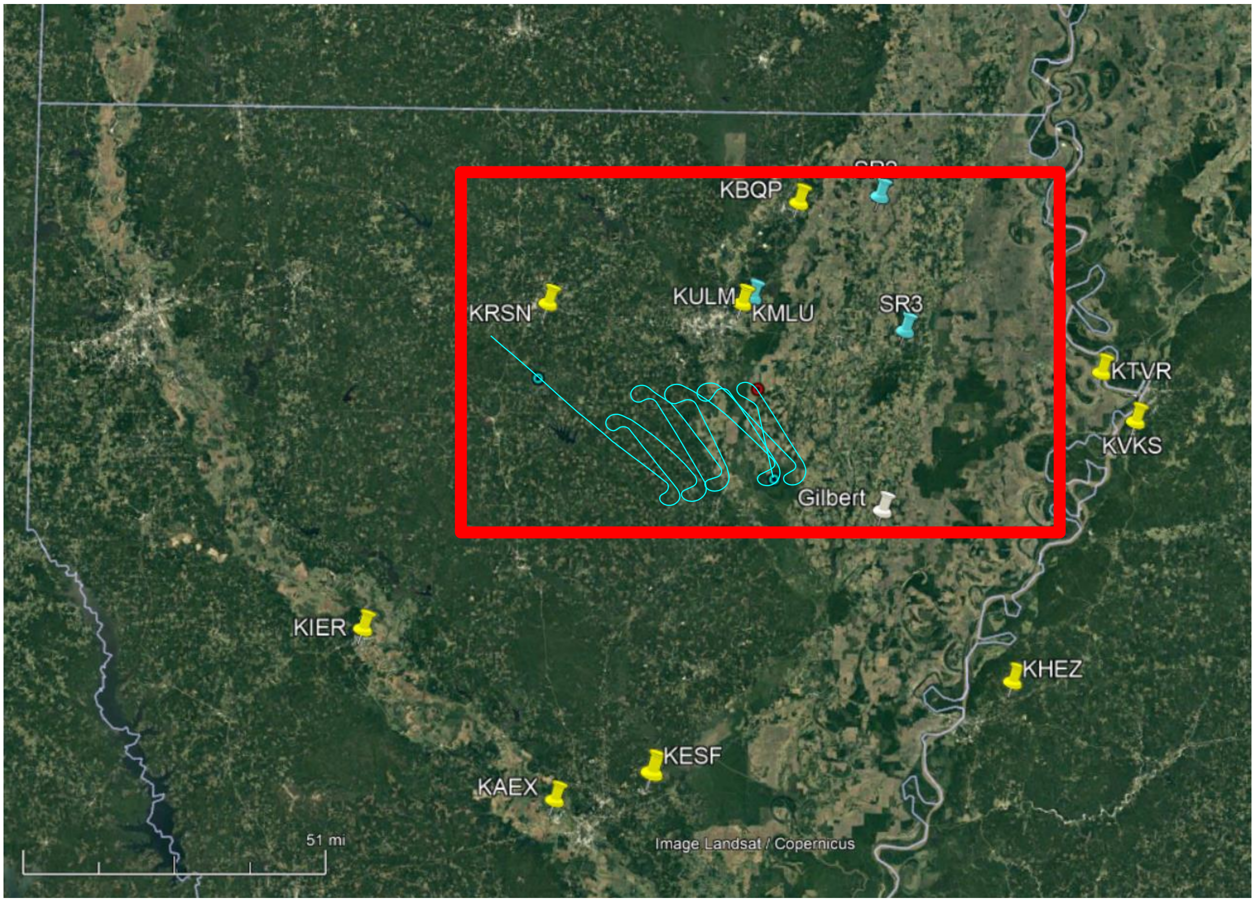

Figure 2. Location of surface stations (yellow pushpins), ground-based radars (blue pushpins), the Gilbert sounding (white pushpin – Monroe soundings are coincident with KMLU), the flight track of the P-3 (blue line), and starting location of the EF-0 tornado at 2340 UTC (red dot – note that the P-3 traversing over this location occurred at a later time). The five surface stations north of the storm were grouped together as the "northern stations", while the four stations to the south grouped as the "southern stations". The red box denotes the Big Grid analysis domain.

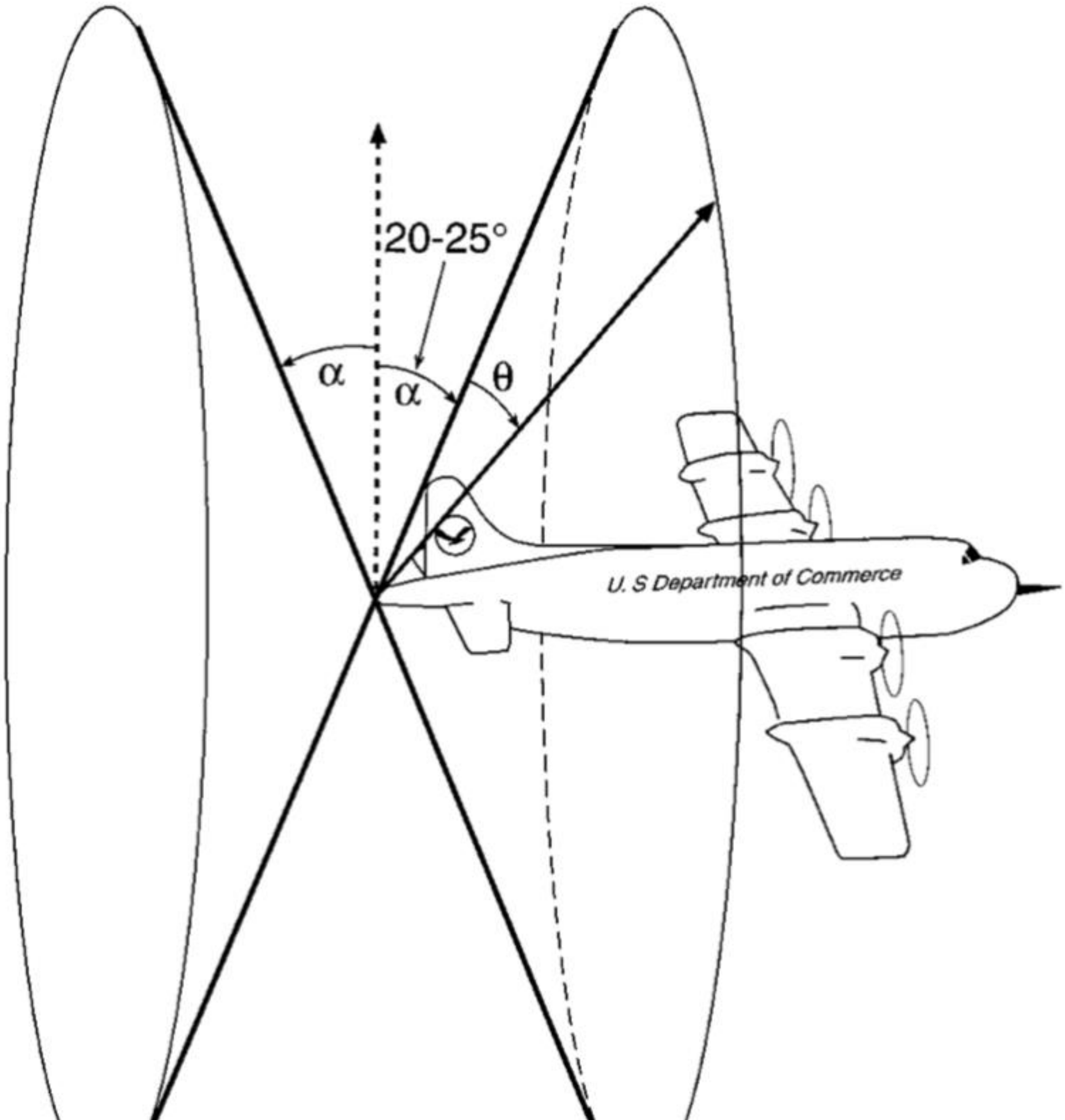

Figure 3. Scanning strategy for TDR-Aft and TDR-fore (Jorgenson and Smull, 1993; figure from Bluestein et al. 1997).

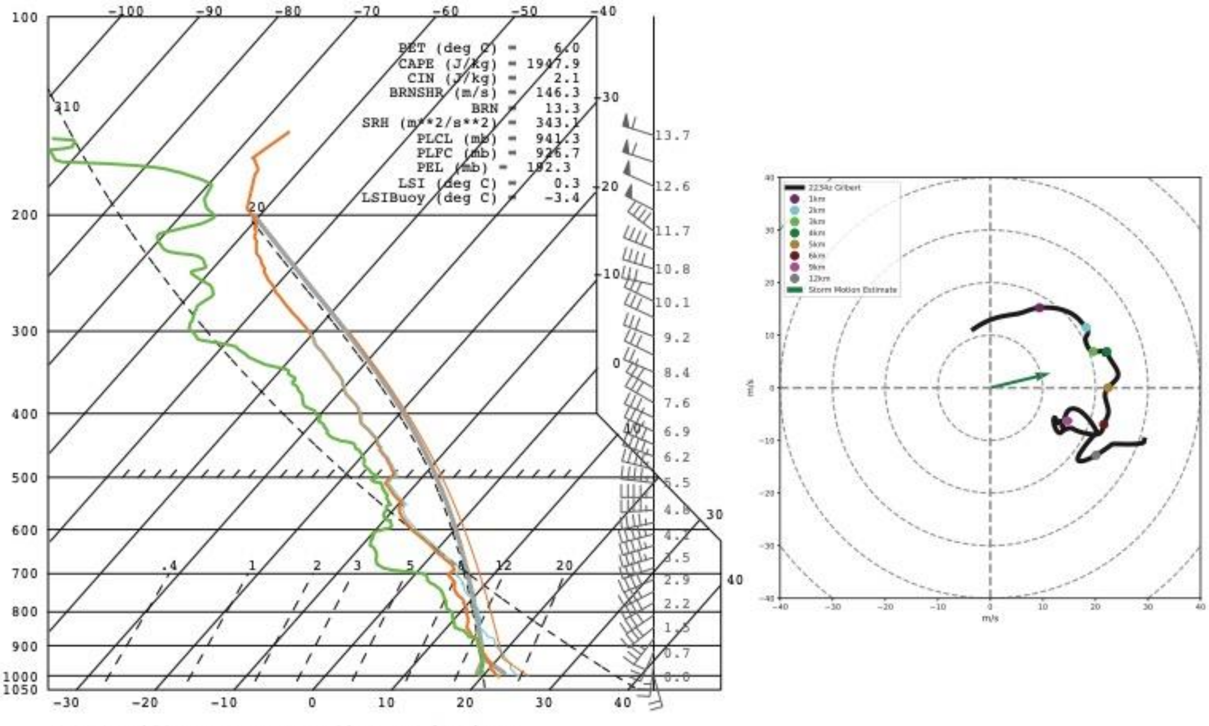

2234 Gilbert LA sounding (4/06/18)

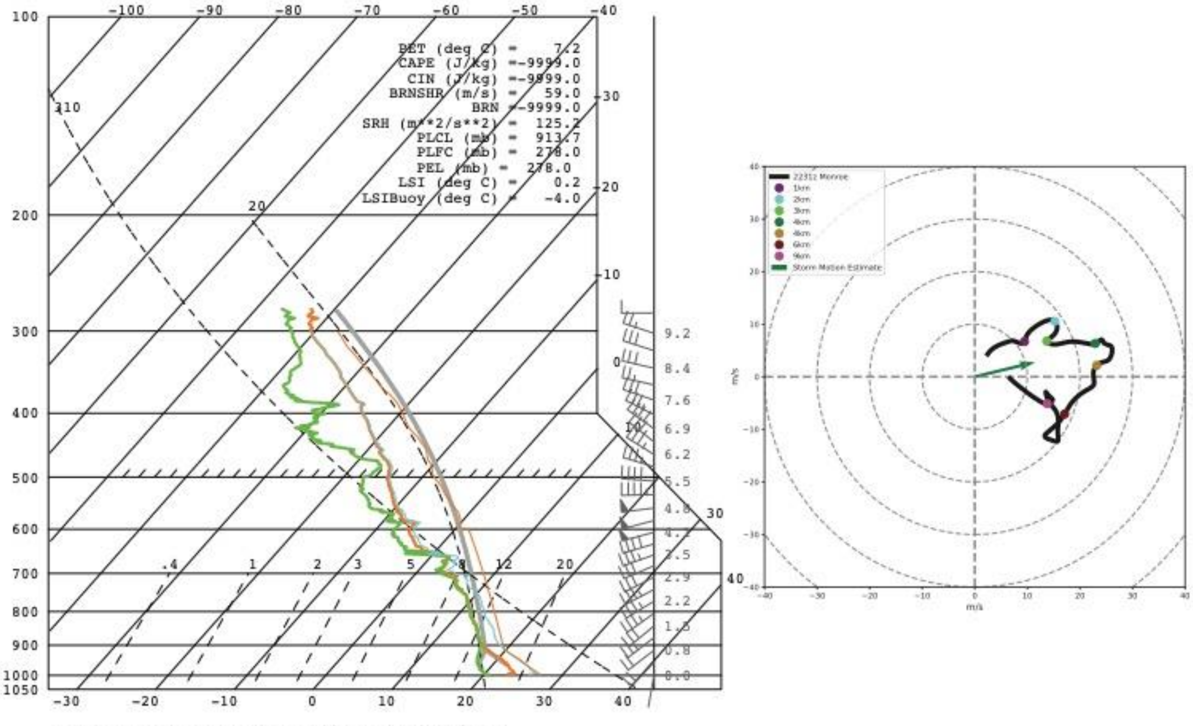

2231 Monroe LA sounding (4/06/18)

Figure 4. 2234 UTC Gilbert sounding (top) and 2231 UTC Monroe sounding (bottom). The adiabatic lifting of a surface parcel is shown in gray. Colored dots denote heights above the surface on the hodograph, with storm motion as the green arrow.

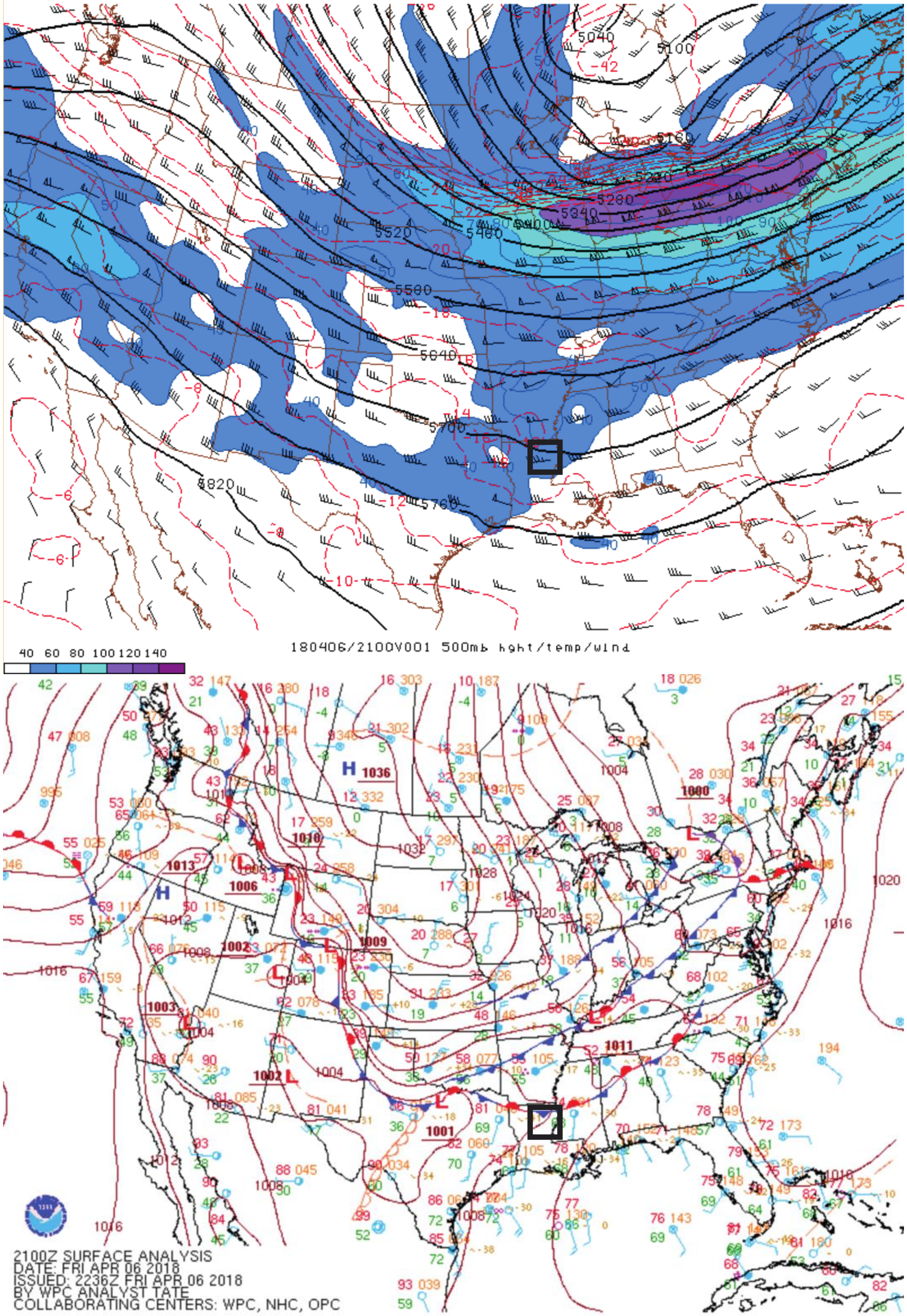

Figure 5. 500mb SPC mesoanalysis (top) with geopotential height contoured, wind speed shaded, and wind barbs (kts) at 21z. Surface analysis (bottom) at 21 UTC from the NOAA Weather Prediction Center (WPC). Box denotes the Big Grid analysis domain.

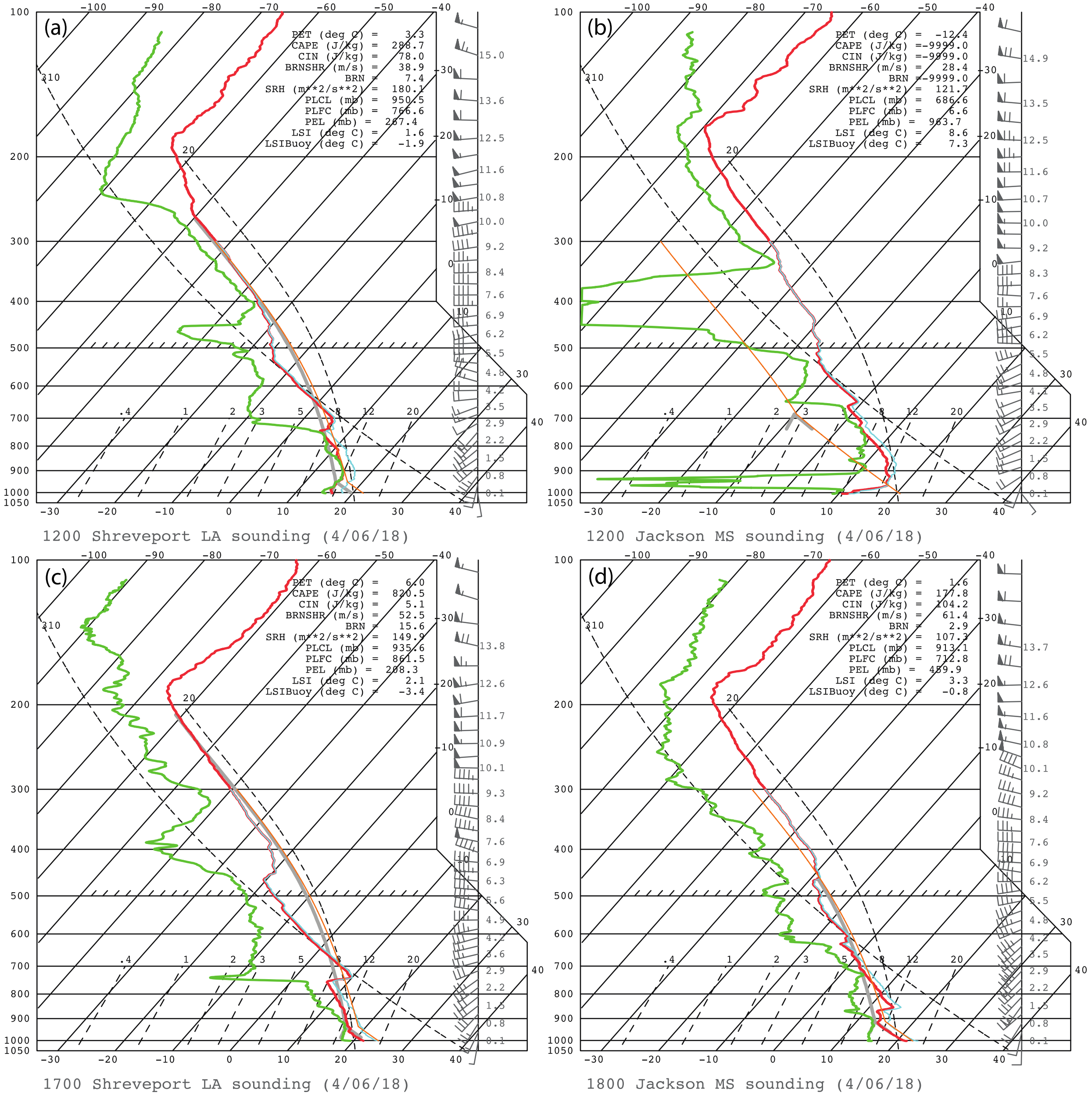

Figure 6. Regional operational soundings between 12 UTC and 18 UTC on 6 April 2018 from Shreveport, LA (a, c) and Jackson, MS (b, d).

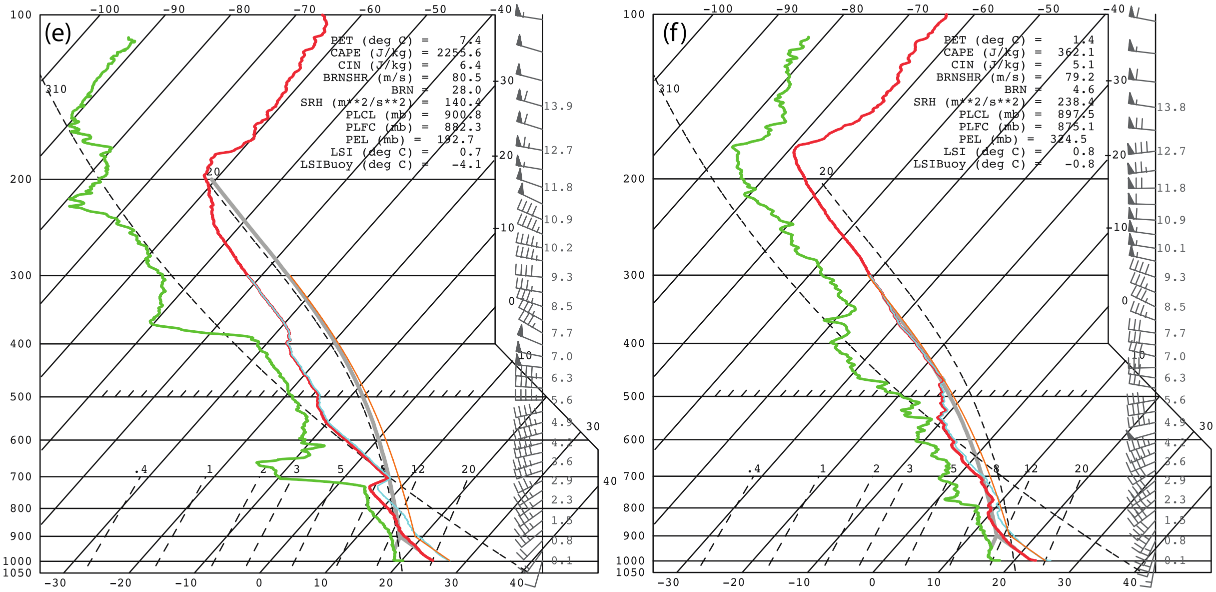

2100 Shreveport LA sounding (4/06/18)

2100 Jackson MS sounding (4/06/18)

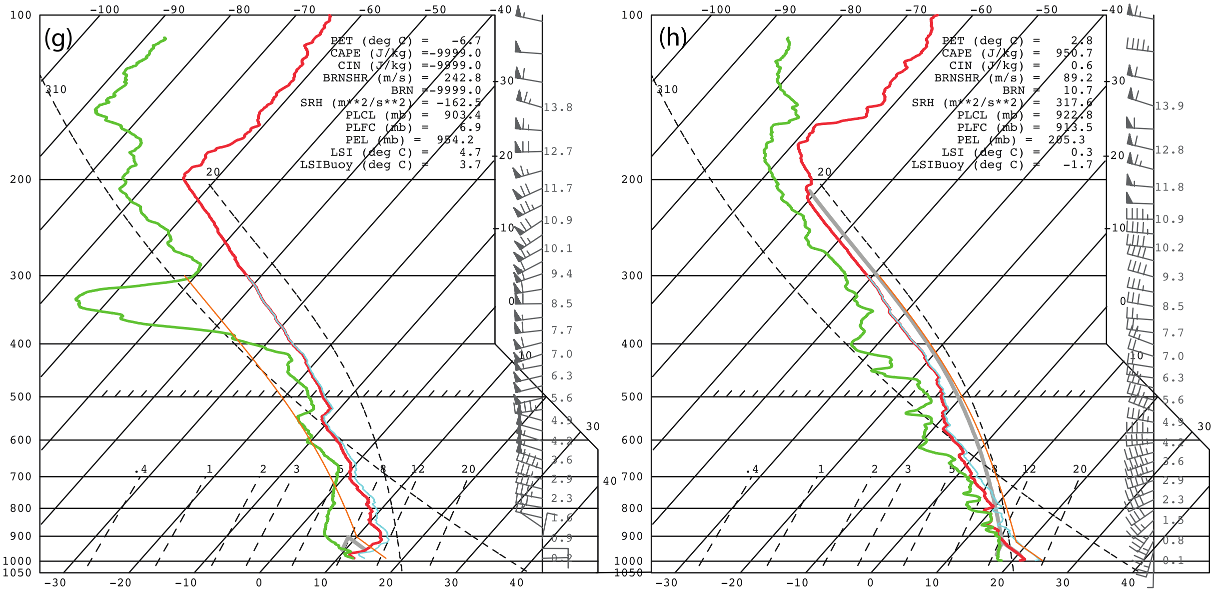

2300 Little Rock AK sounding (4/06/18)

2300 Jackson MS sounding (4/06/18)

Figure 7. Continued from Figure 6, regional operational soundings from 21 UTC on 6 April 2018 through 00 UTC on 7 April 2018 from Shreveport, LA (e), Jackson, MS (f, h), and Little Rock, AK (g).

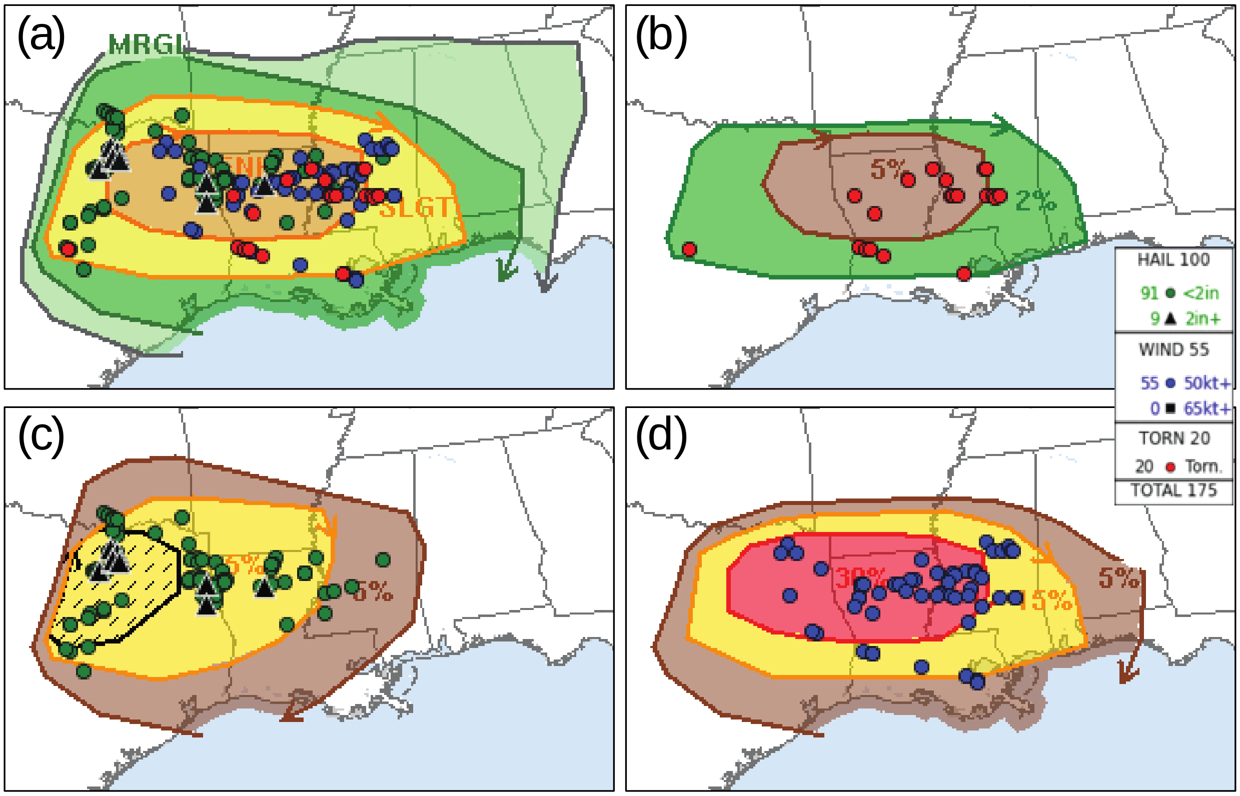

Figure 8. SPC 12 UTC day 1 outlook for 4/6/18, with storm reports. General forecast with all reports (a), tornado forecast with tornado reports (b), hail forecast with hail reports (c), and wind forecast with severe wind reports (d).

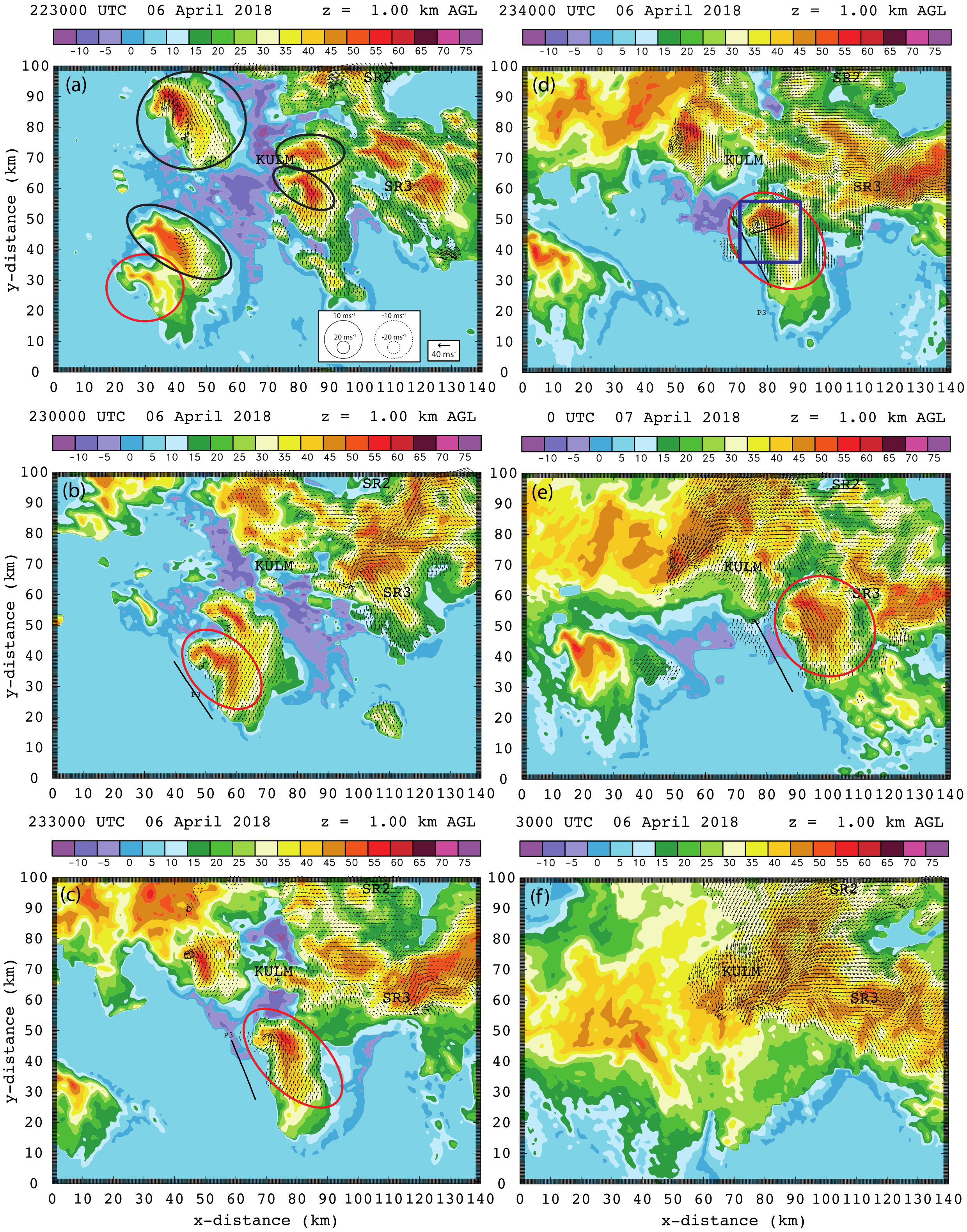
223000 UTC 06 April 2018 z = 1.00 km AGL
234000 UTC 06 April 2018 z = 1.00 km AGL
230000 UTC 06 April 2018 z = 1.00 km AGL
0 UTC 07 April 2018 z = 1.00 km AGL
233000 UTC 06 April 2018 z = 1.00 km AGL
3000 UTC 06 April 2018 z = 1.00 km AGL
-10 -5 0 5 10 15 20 25 30 35 40 45 50 55 60 65 70 75
(a)
(b)
(c)
(d)
(e)
(f)
SR2
KULM
SR3
P3
10 ms-1
-10 ms-1
20 ms-1
-20 ms-1
40 ms-1
y-distance (km)
x-distance (km)
0 10 20 30 40 50 60 70 80 90 100
0 10 20 30 40 50 60 70 80 90 100 110 120 130 140

Figure 9. Reflectivity overview on the Big Grid domain at 2230 UTC (a), 2300 UTC (b), 2330 UTC (c), 2340 UTC (d), 0000 UTC (e), and 0030 UTC (f) at an analysis height of 1 km AGL. Legend for all subplots is in the lower right corner of (a). The axes are labeled in distance from the origin, with minor tick marks signifying the grid spacing (250 m). Vectors denote radar-analyzed storm-relative winds and are present at all gridpoints with at least a 2-radar synthesis. Contours denote vertical motion. The ground-based radar locations are labeled. The red oval highlights the Monroe Supercell, while the black ovals in (a) highlight the other supercells present within the domain at that analysis time. The black line represents the flight path of the P-3 during the leg corresponding to the given analysis time, with the "P-3" label representing the exact location of the aircraft at the analysis time. The dark blue box on (d) highlights the domain of the Merged Nested Grid at that analysis time (see Figure 25).

Figure 10. Tornado damage assessment by the NOAA National Weather Service (NWS) for the EF-0 tornado (a). Blue triangle denotes EF-0 damage points and the solid blue line denotes the tornado track. The green triangle (at arrowhead) is an EF-1 damage point, separate from the EF-0 tornado, pictured in (b) (NOAA NCEI Storm Events Database). View looking west-southwest, with branch blow-down toward the northeast.

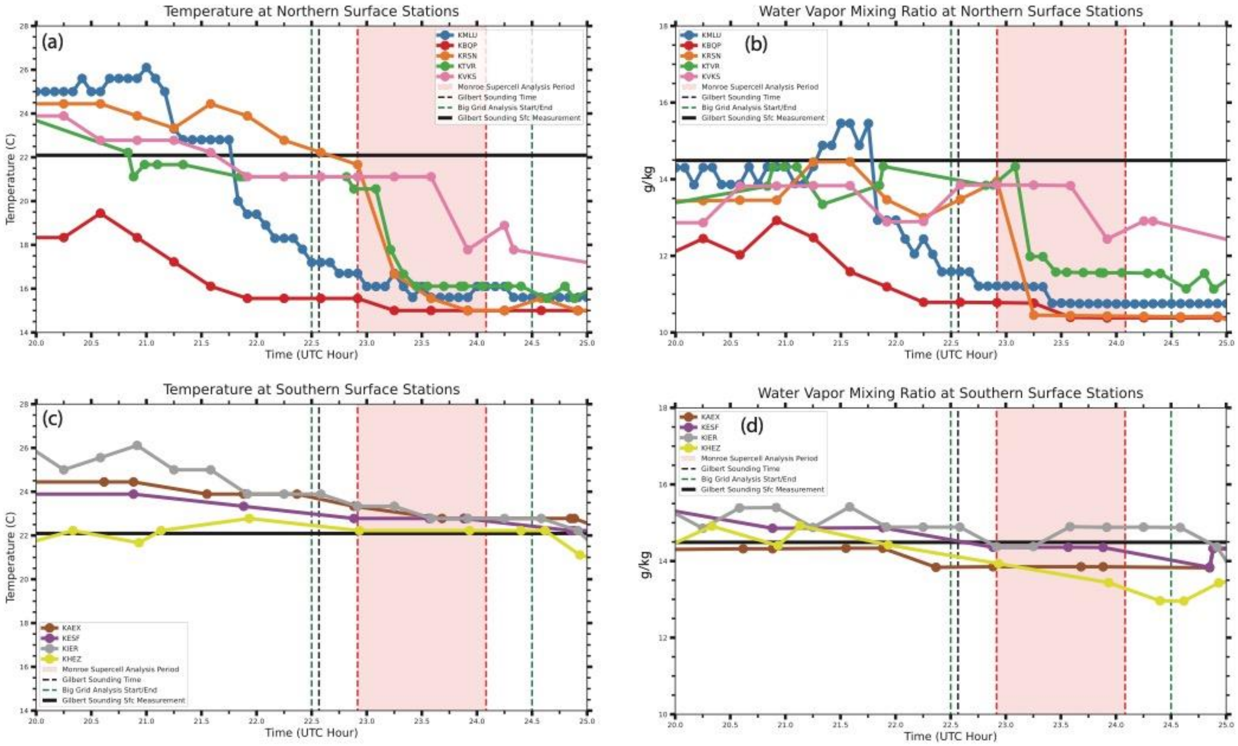

Figure 11. Time series, in UTC hour, of measured air temperature at the northern and southern suite of surface stations (a, c respectively) and water vapor mixing ratio derived from observations at the northern and southern suite of surface stations (b, d respectively). Dots represent time at which data was recorded. The black solid line represents the value of that variable at the surface for the Gilbert proximity sounding, while the vertical black dashed line represents the time that sounding was launched. Green-dashed lines denote the start and end of the Big Grid radar analyses. The red-shaded region bounded by red-dashed lines denotes the Monroe Supercell Analysis Period.

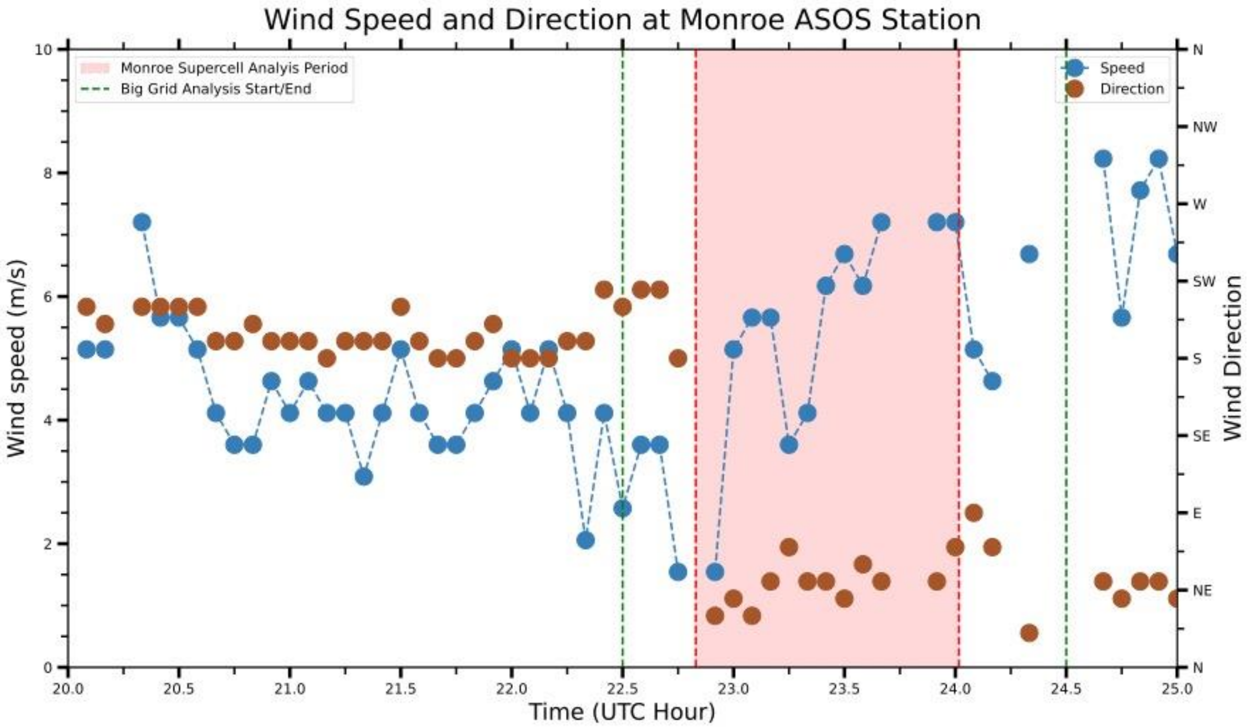

Figure 12. Time series of wind speed (blue, left axis) and direction (brown, right axis) at the KMLU (Monroe) ASOS station, as in Figure 11. Dashed-blue lines represent consecutive recordings by the station, while gaps represent one or more recording times with missing value.

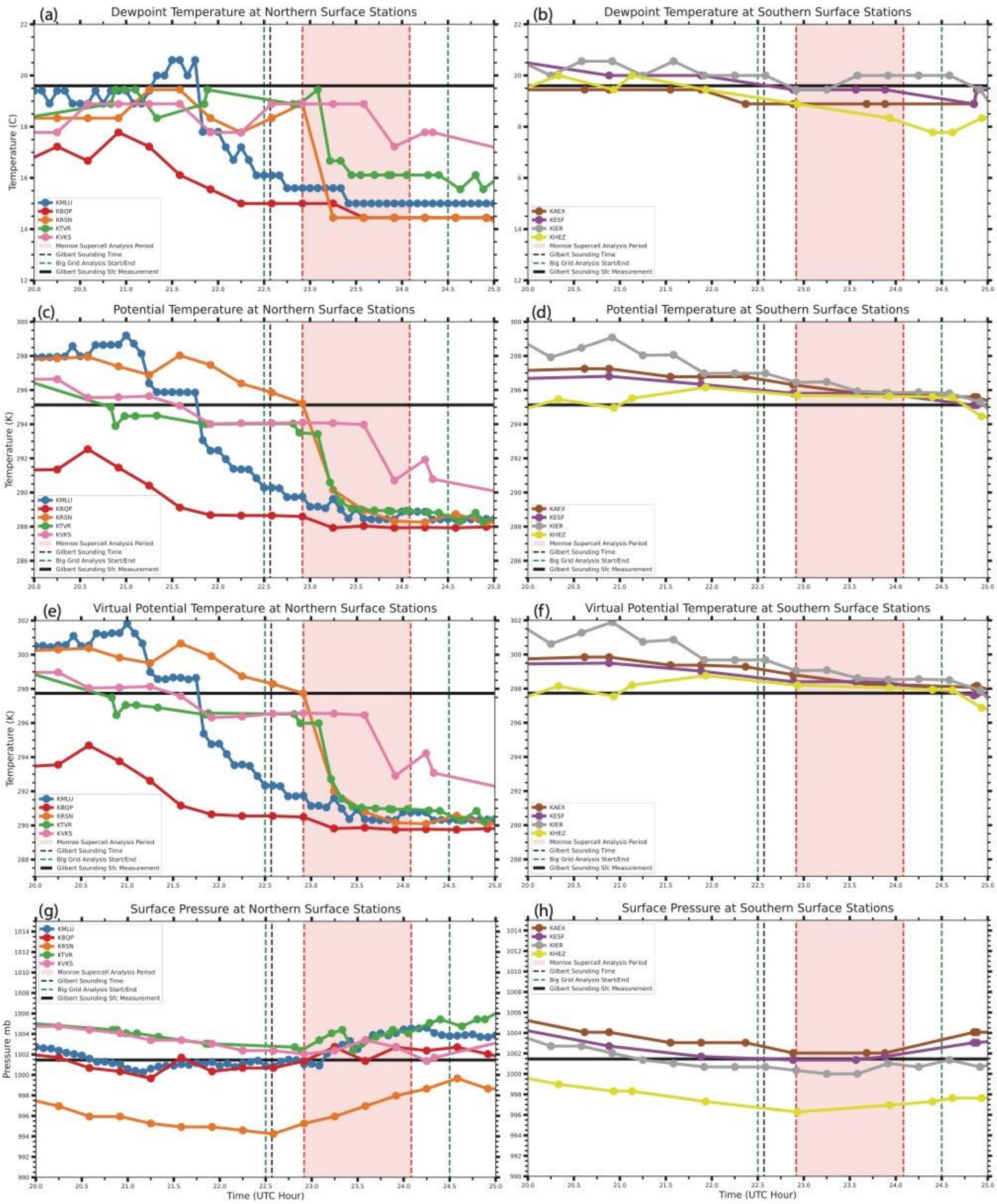

Figure 13. As in Figure 11, but for northern and southern suites, left and right respectively, for dewpoint temperature (a, b), potential temperature (c, d), virtual potential temperature (e, f), and surface pressure (g, h).

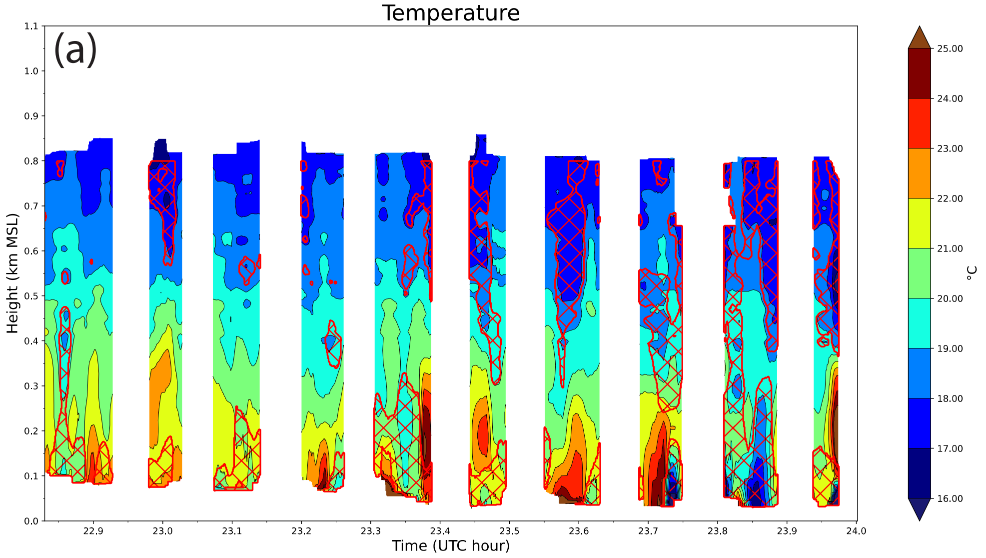
Temperature
(a)
Height (km MSL)
0.0
0.1
0.2
0.3
0.4
0.5
0.6
0.7
0.8
0.9
1.0
1.1
22.9
23.0
23.1
23.2
23.3
23.4
23.5
23.6
23.7
23.8
23.9
24.0
Time (UTC hour)
°C
25.00
24.00
23.00
22.00
21.00
20.00
19.00
18.00
17.00
16.00

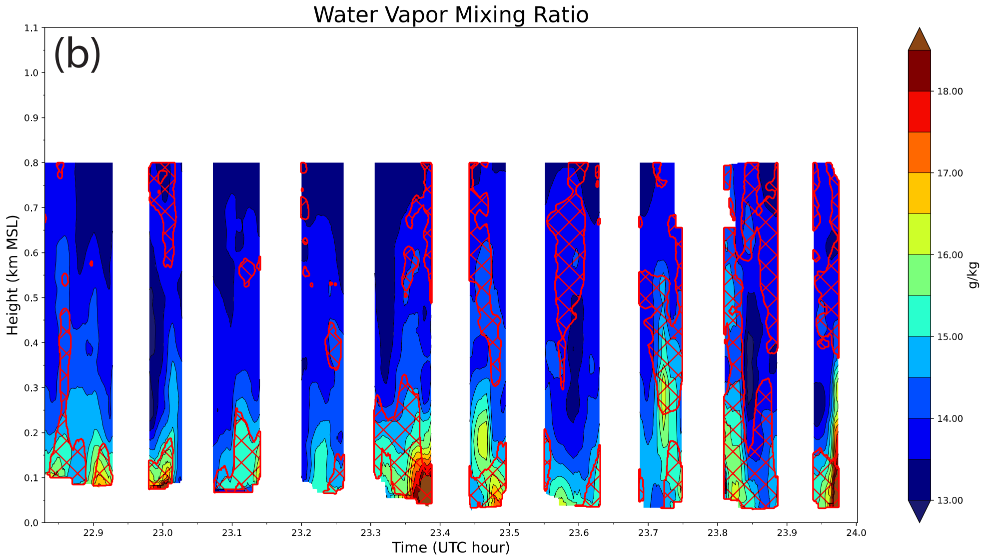
Water Vapor Mixing Ratio
(b)
Height (km MSL)
0.0
0.1
0.2
0.3
0.4
0.5
0.6
0.7
0.8
0.9
1.0
1.1
22.9
23.0
23.1
23.2
23.3
23.4
23.5
23.6
23.7
23.8
23.9
24.0
Time (UTC hour)
g/kg
18.00
17.00
16.00
15.00
14.00
13.00

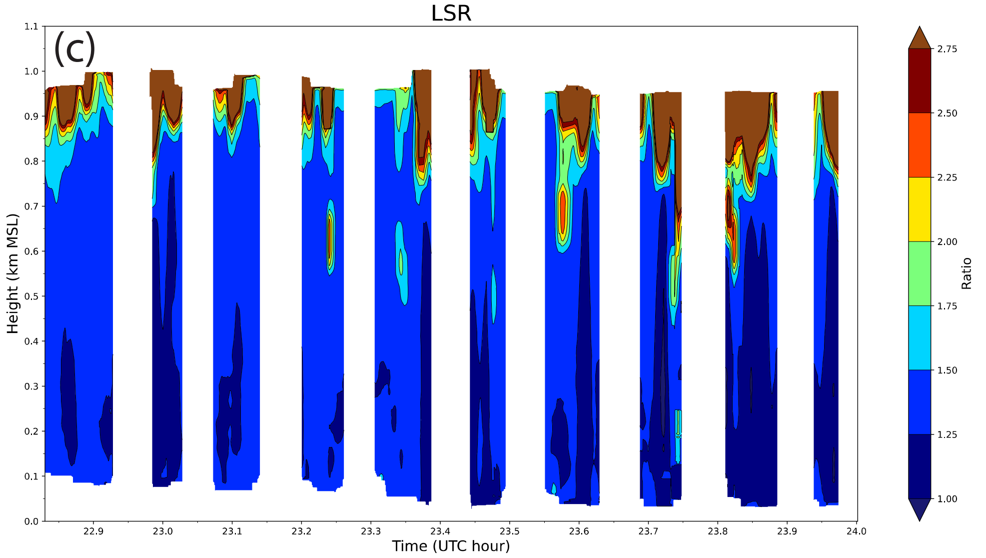
LSR
(c)
Height (km MSL)
0.0
0.1
0.2
0.3
0.4
0.5
0.6
0.7
0.8
0.9
1.0
1.1
22.9
23.0
23.1
23.2
23.3
23.4
23.5
23.6
23.7
23.8
23.9
24.0
Time (UTC hour)
Ratio
2.75
2.50
2.25
2.00
1.75
1.50
1.25
1.00

Figure 14. Time series versus height color-fill plots of CRL measured temperature (a), water vapor mixing ratio (b), and lidar scattering ratio (LSR, c). Red hatching denotes regions with non-physical relative humidity which were masked (see section 2.2.3) Time is in UTC hour, and height is in km MSL, but can reasonably be approximated to AGL due to this region of Louisiana being only ~20 m above sea level.

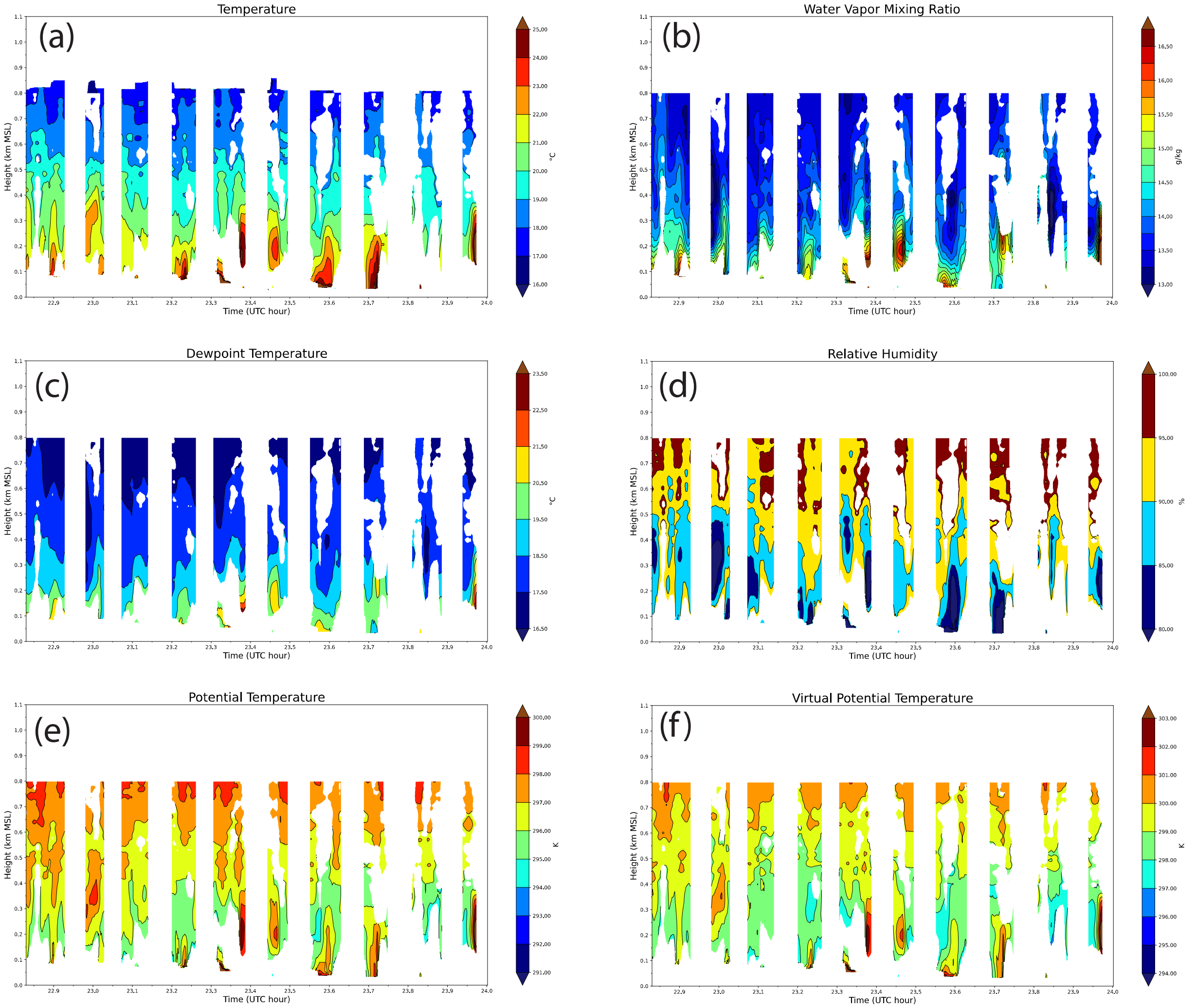

Figure 15. As in Figure 14, but with masked regions removed, for CRL measured temperature (a) and water vapor mixing ratio (b), as well as derived quantities dewpoint temperature (c), relative humidity (d), potential temperature (e), and virtual potential temperature (f).

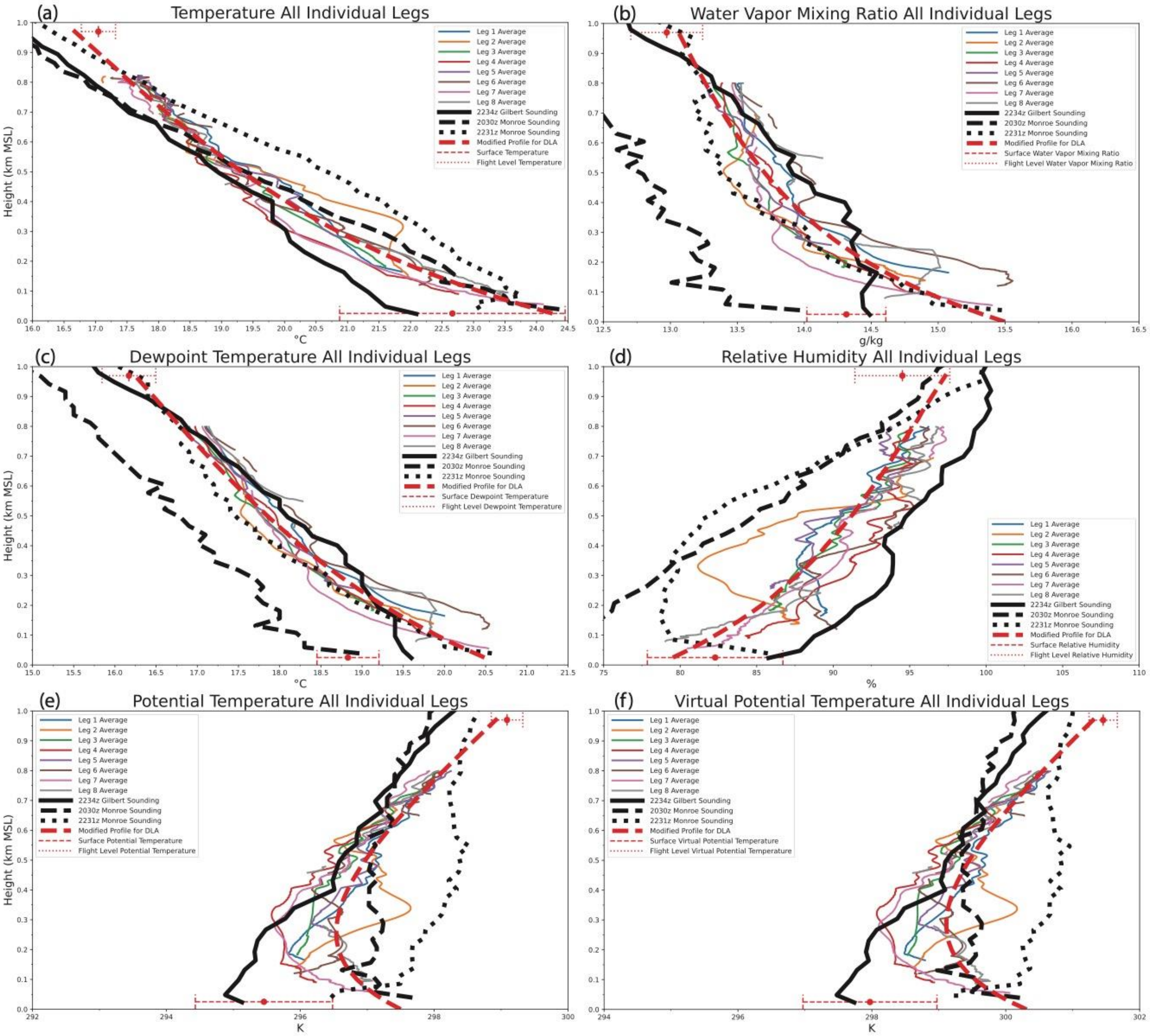

Figure 16. Leg-averaged vertical profiles of CRL measurements (colored lines) compared to the 2030 UTC Monroe sounding (dashed-black), 2231 UTC Monroe sounding (dotted-black), and 2234 UTC Gilbert sounding (solid-black) as well as to the average surface observation (red dot) +/- 1 standard deviation (red-dashed) and average value measured by the P-3 over the course of the analysis period (red dot) +/- 1 standard deviation (red-dotted) at the average elevation during the analysis period, +/- 1 standard deviation (vertical red line), for temperature (a), water vapor mixing ratio (b), dewpoint temperature (c), relative humidity (d), potential temperature (e), virtual potential temperature (f).

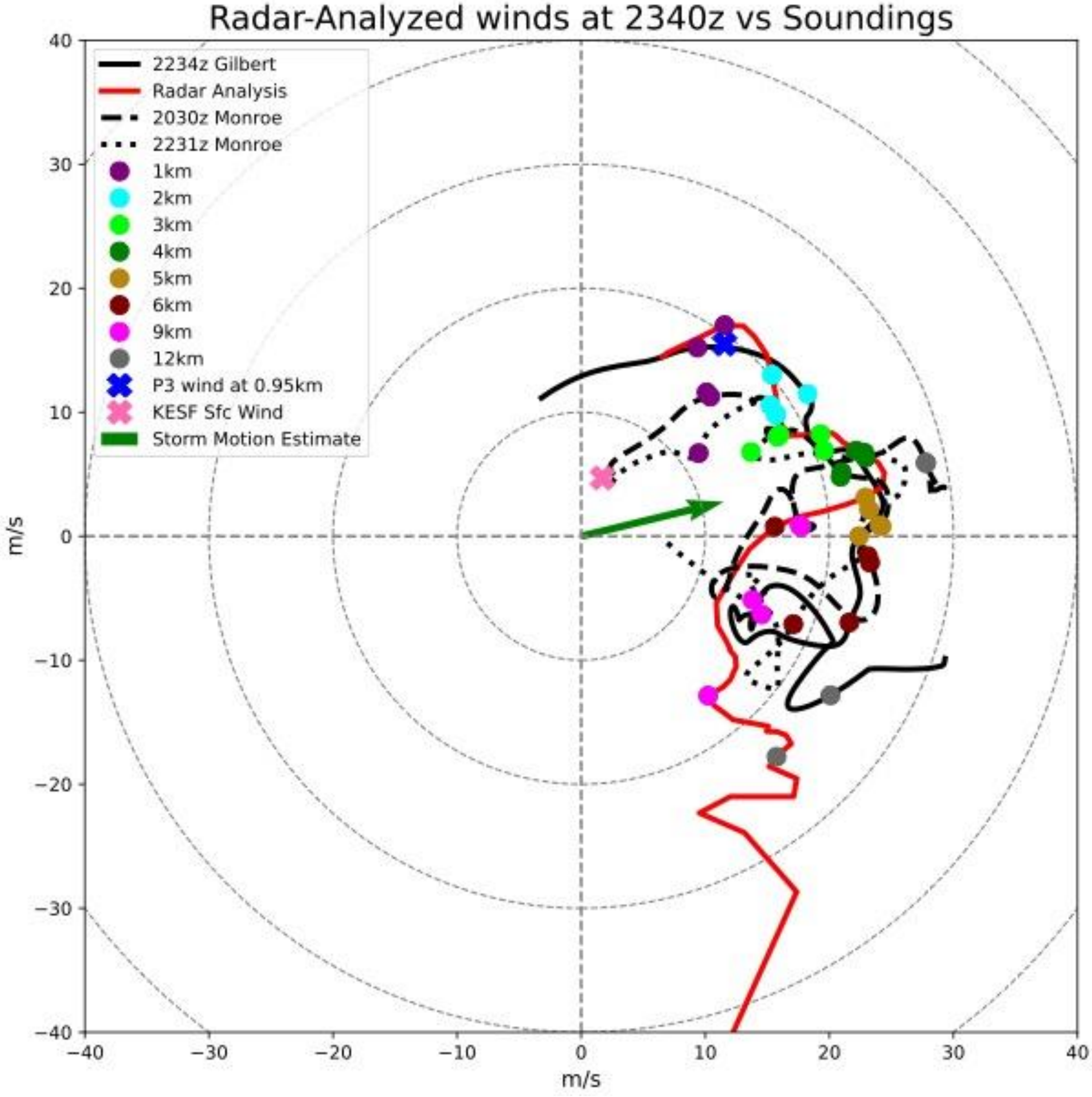

Figure 17. The radar-analyzed hodograph at 2340 UTC (red line) against the 2030 UTC Monroe hodograph (black-dashed), 2231 UTC Monroe hodograph (black-dotted), and 2234 UTC Gilbert hodograph (black-solid). Storm motion is at the tip of the green arrow. P-3 measured wind and direction at ~1km AGL during the corresponding leg is plotted at the blue "X", and KESF surface wind at 2340 UTC is plotted at the pink "X". Colored dots denote height markers.

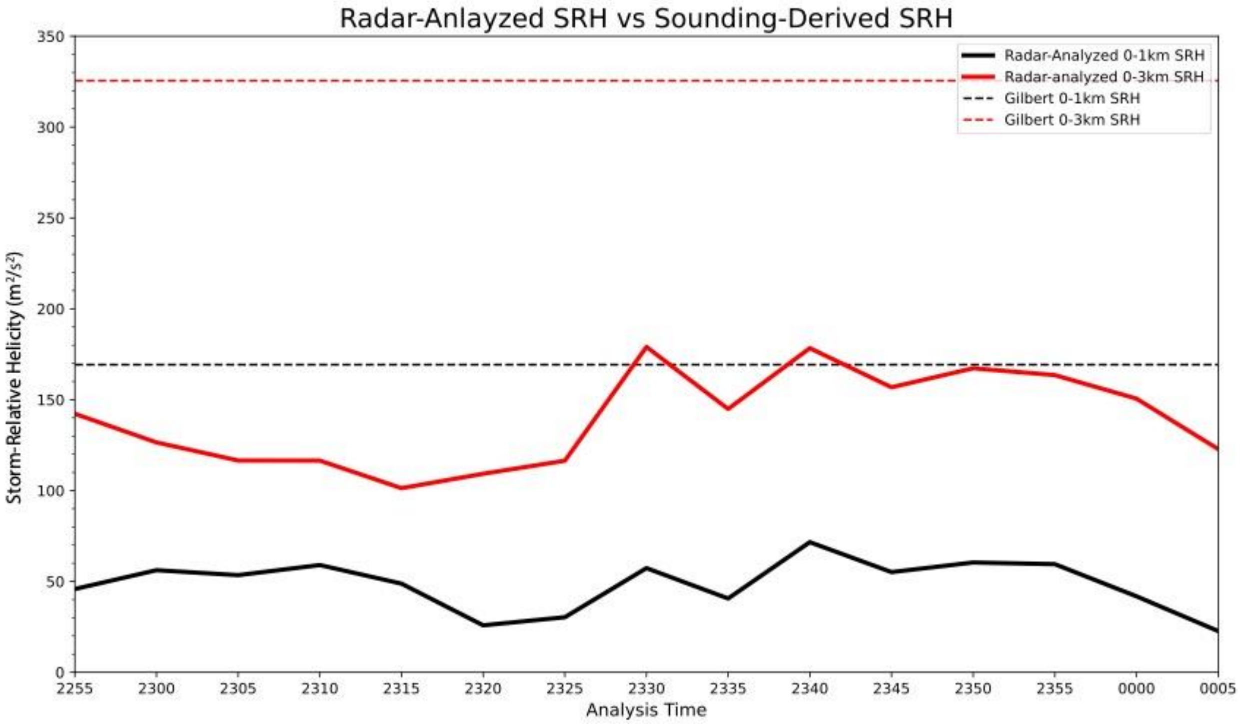

Figure 18. Calculated 0—1 km (black) and 0—3 km (red) Storm-Relative Helicity (SRH) for the Gilbert sounding (dashed) and the radar-analyzed hodographs at each analysis time of the Monroe Supercell Analysis Period (solid).

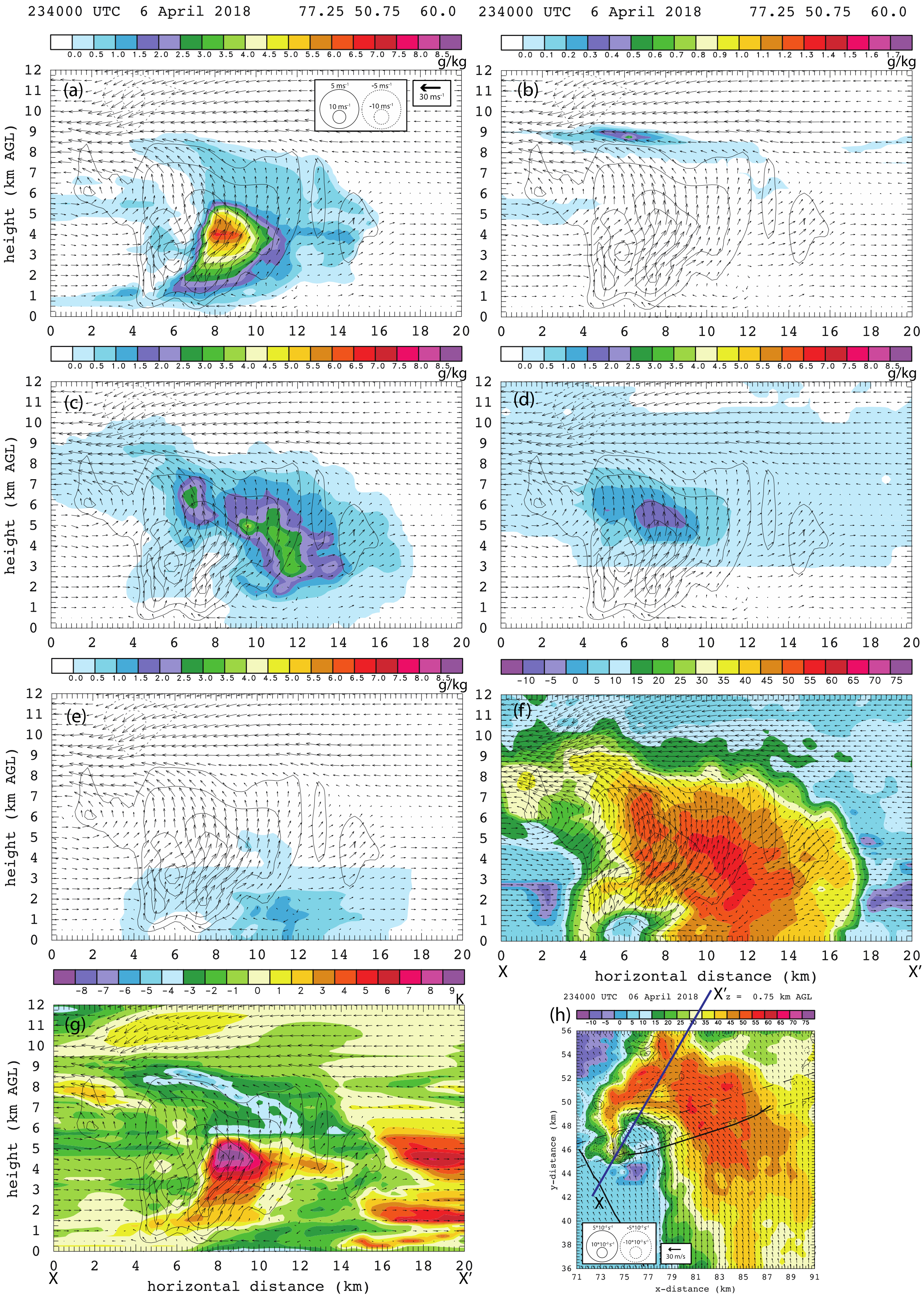
234000 UTC 6 April 2018 77.25 50.75 60.0
234000 UTC 6 April 2018 77.25 50.75 60.0
0.0 0.5 1.0 1.5 2.0 2.5 3.0 3.5 4.0 4.5 5.0 5.5 6.0 6.5 7.0 7.5 8.0 8.5
g/kg
0.0 0.1 0.2 0.3 0.4 0.5 0.6 0.7 0.8 0.9 1.0 1.1 1.2 1.3 1.4 1.5 1.6 1.7
(a)
(b)
(c)
(d)
(e)
(f)
(g)
(h)
5 ms⁻¹
-5 ms⁻¹
10 ms⁻¹
-10 ms⁻¹
30 ms⁻¹
height (km AGL)
-10 -5 0 5 10 15 20 25 30 35 40 45 50 55 60 65 70 75
-8 -7 -6 -5 -4 -3 -2 -1 0 1 2 3 4 5 6 7 8 9
K
horizontal distance (km)
X
X′
234000 UTC 06 April 2018
X′z = 0.75 km AGL
y-distance (km)
x-distance (km)
30 m/s

Figure 19. Vertical cross-sections of cloud water mixing ratio (a), cloud ice mixing ratio (b), graupel/hail mixing ratio (c), snow mixing ratio (d), rainwater mixing ratio (e), reflectivity (f), and θ_v' (g) at 2340 UTC along a 20 km distance demarcated by the dark blue line (X-X') in the horizontal cross-section plot of reflectivity (h). Vertical velocity is contoured in all subplots. The legend for each vertical cross-section (a-g) is in the top right of (a).

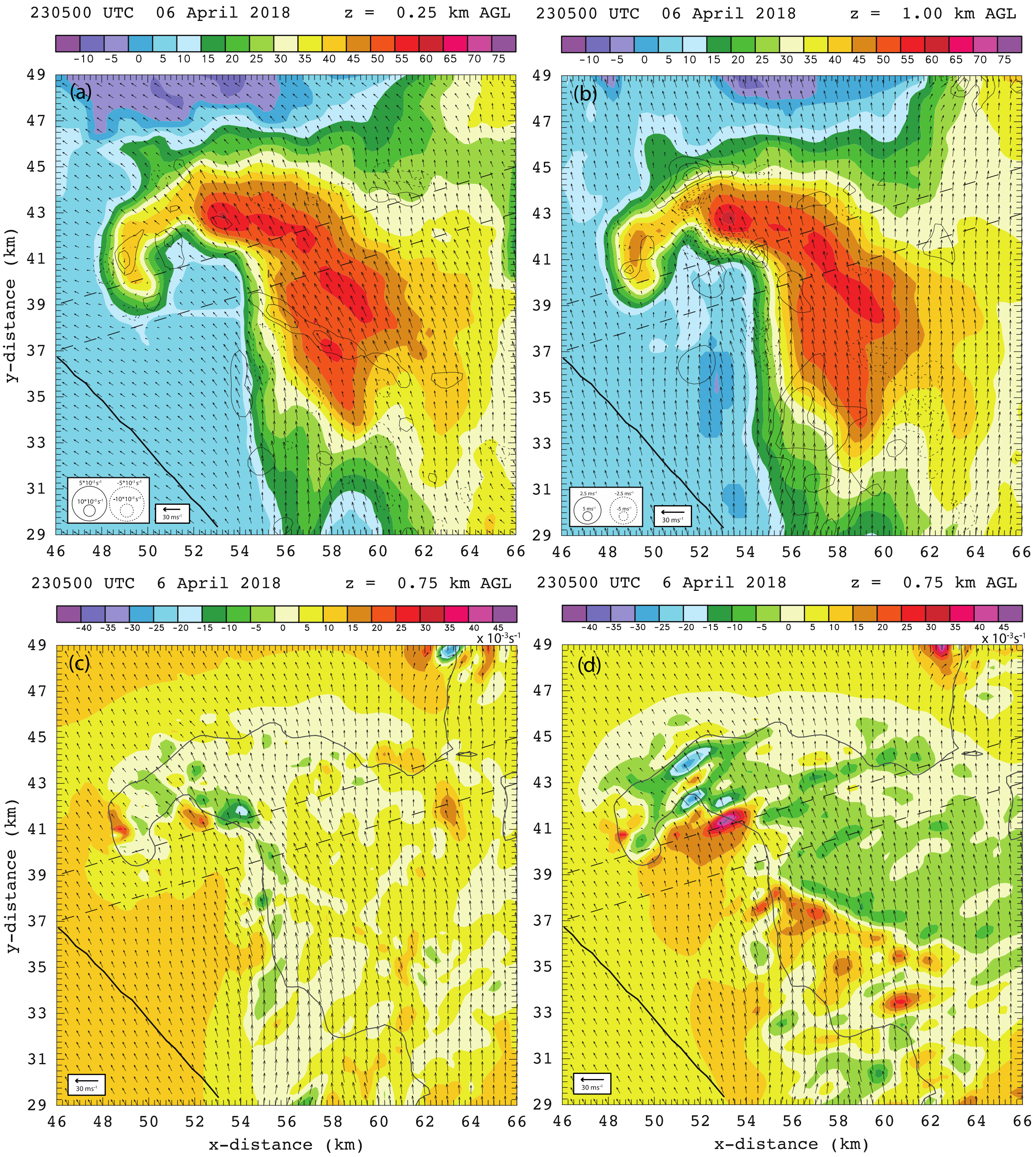

Figure 20. Radar analysis at 2305 UTC, for reflectivity-fill with vertical vorticity contoured at 0.25 km AGL (a), reflectivity-fill with vertical velocity contoured at 1 km AGL (b), streamwise vorticity fill with 10 dBZ contour at 0.75 km AGL (c), and crosswise vorticity fill with 10 dBZ contour at 0.75 km AGL (d). Solid black line to the lower right denotes the flight track for the given leg. Dashed lines denote the location, along storm motion, of the tornado-cyclone and northern low-level mesocyclone at 2340 UTC (see section 4.4.3).

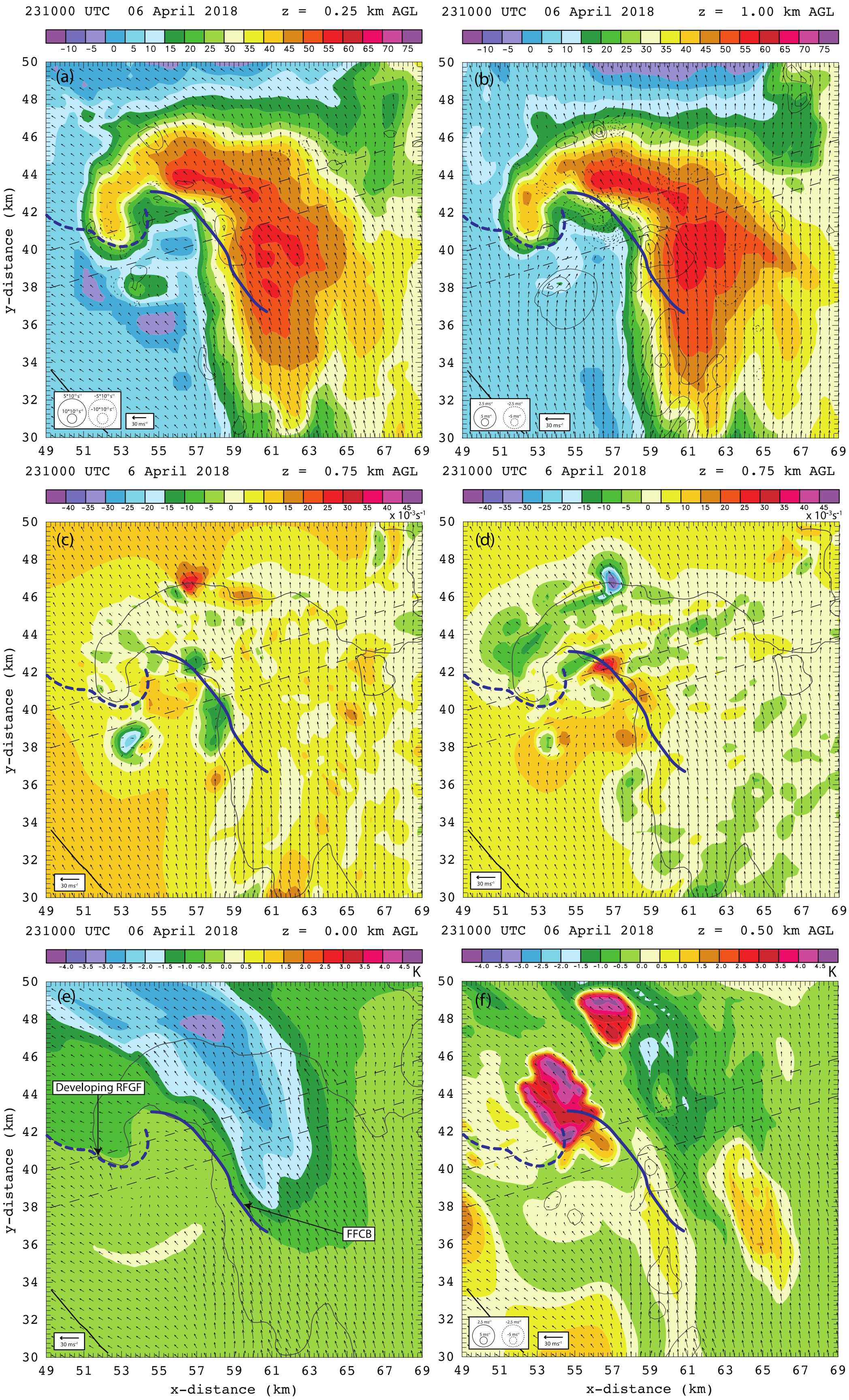

231000 UTC 06 April 2018 z = 0.25 km AGL
231000 UTC 06 April 2018 z = 1.00 km AGL
-10 -5 0 5 10 15 20 25 30 35 40 45 50 55 60 65 70 75
(a)
(b)
231000 UTC 6 April 2018 z = 0.75 km AGL
231000 UTC 6 April 2018 z = 0.75 km AGL
-40 -35 -30 -25 -20 -15 -10 -5 0 5 10 15 20 25 30 35 40 45
x 10⁻³s⁻¹
(c)
(d)
231000 UTC 06 April 2018 z = 0.00 km AGL
231000 UTC 06 April 2018 z = 0.50 km AGL
-4.0 -3.5 -3.0 -2.5 -2.0 -1.5 -1.0 -0.5 0.0 0.5 1.0 1.5 2.0 2.5 3.0 3.5 4.0 4.5 K
(e)
(f)
Developing RFGF
FFCB
30 ms⁻¹
y-distance (km)
x-distance (km)
30 32 34 36 38 40 42 44 46 48 50
49 51 53 55 57 59 61 63 65 67 69

Figure 21. As in Figure 20, for 2310 UTC and with the virtual potential temperature perturbation $\theta_v{}'$ (filled) with 10 dBZ contour at 0 km AGL (E) and $\theta_v{}'$ (fill) with vertical velocity contoured at 0.5 km AGL (f). Blue lines denote surface boundaries identified using the surface $\theta_v{}'$ field and wind field (e). Dashed lines denote surface boundaries that are weak or developing.

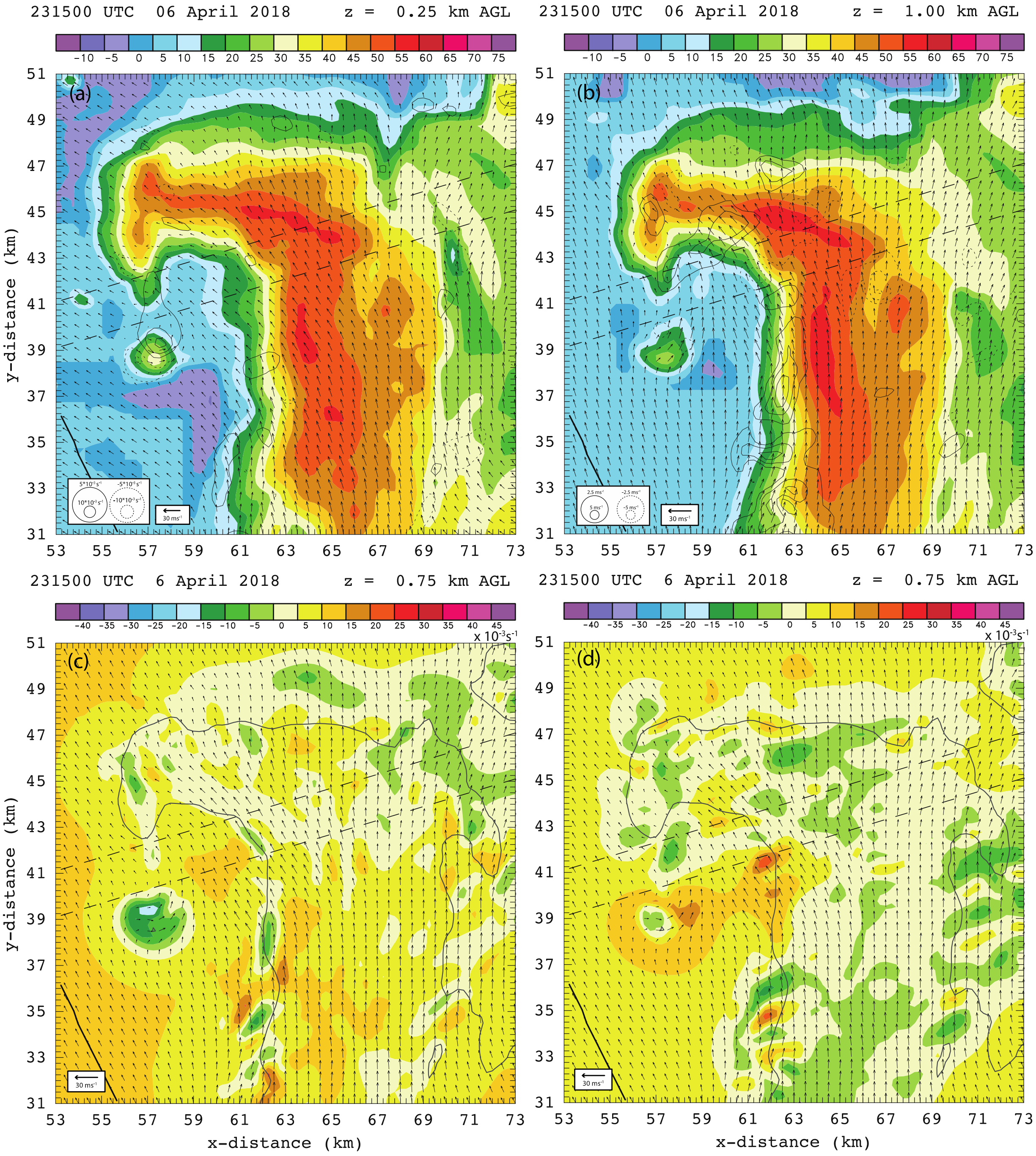

Figure 22. As in Figure 20, for 2315 UTC.

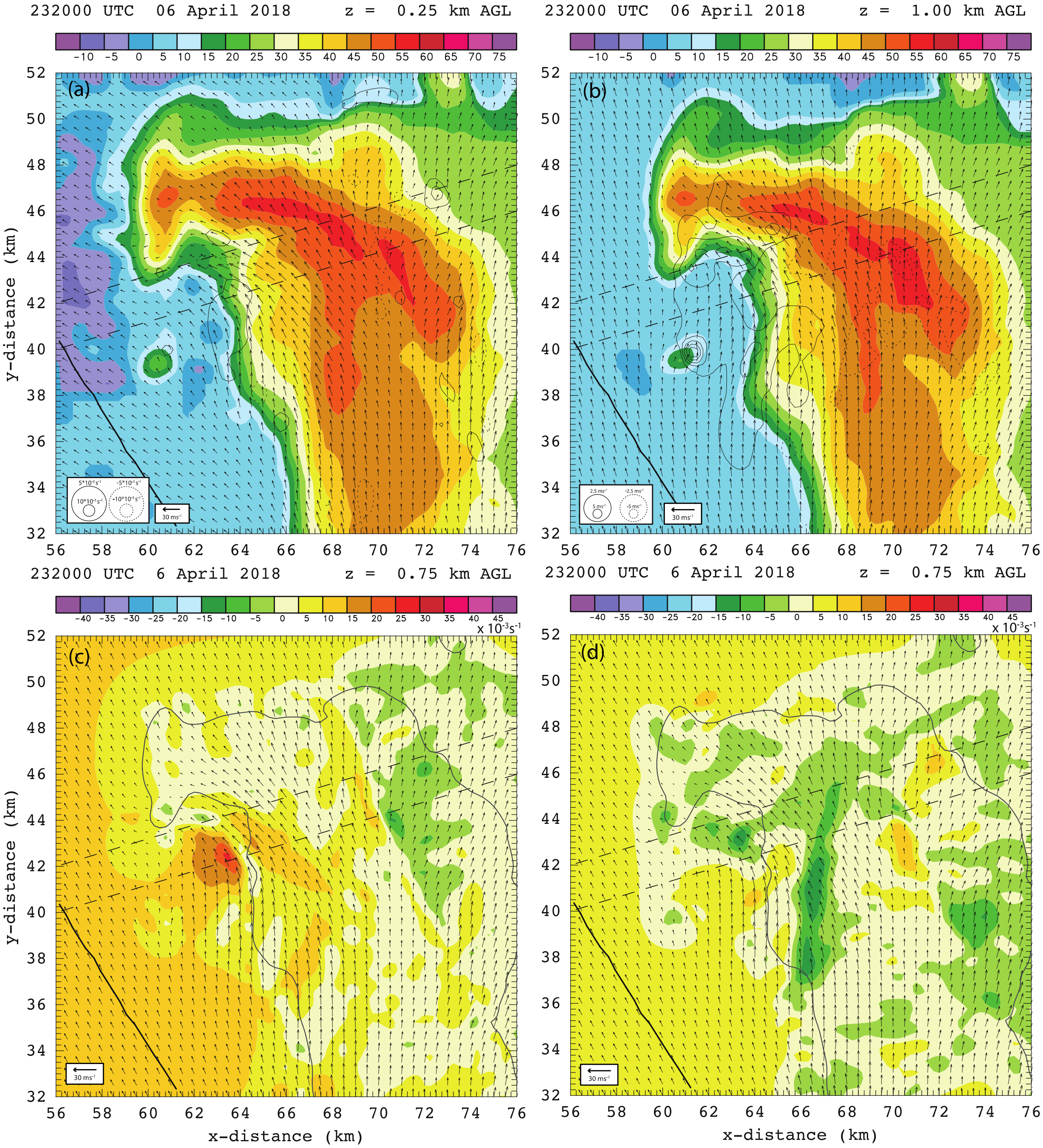

Figure 23. As in Figure 20, for 2320 UTC.

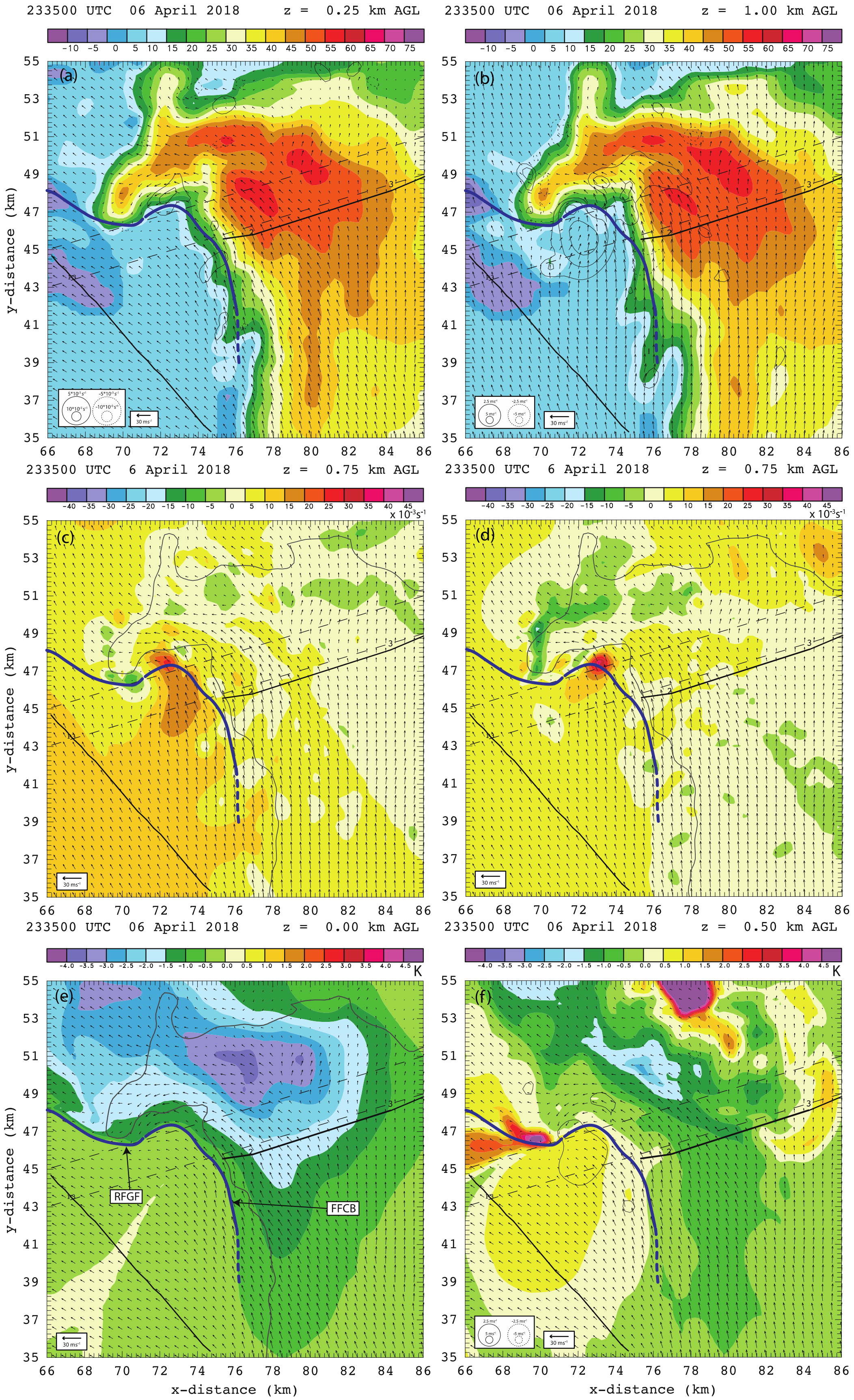

233500 UTC 06 April 2018 z = 0.25 km AGL
-10 -5 0 5 10 15 20 25 30 35 40 45 50 55 60 65 70 75
(a)
233500 UTC 06 April 2018 z = 1.00 km AGL
-10 -5 0 5 10 15 20 25 30 35 40 45 50 55 60 65 70 75
(b)
233500 UTC 6 April 2018 z = 0.75 km AGL
-40 -35 -30 -25 -20 -15 -10 -5 0 5 10 15 20 25 30 35 40 45
x 10⁻³s⁻¹
(c)
233500 UTC 6 April 2018 z = 0.75 km AGL
-40 -35 -30 -25 -20 -15 -10 -5 0 5 10 15 20 25 30 35 40 45
x 10⁻³s⁻¹
(d)
233500 UTC 06 April 2018 z = 0.00 km AGL
-4.0 -3.5 -3.0 -2.5 -2.0 -1.5 -1.0 -0.5 0.0 0.5 1.0 1.5 2.0 2.5 3.0 3.5 4.0 4.5
K
(e)
RFGF
FFCB
233500 UTC 06 April 2018 z = 0.50 km AGL
-4.0 -3.5 -3.0 -2.5 -2.0 -1.5 -1.0 -0.5 0.0 0.5 1.0 1.5 2.0 2.5 3.0 3.5 4.0 4.5
K
(f)
y-distance (km)
55 53 51 49 47 45 43 41 39 37 35
x-distance (km)
66 68 70 72 74 76 78 80 82 84 86
30 ms⁻¹

Figure 24. As in Figure 21, for 2335 UTC. The solid curving black line represents the EF-0 tornado damage track, with number labels “2”, “3”, “4”, and “5” representing individual damage markers. Not all markers or the entire length of the track may be within the domain at a given analysis time.

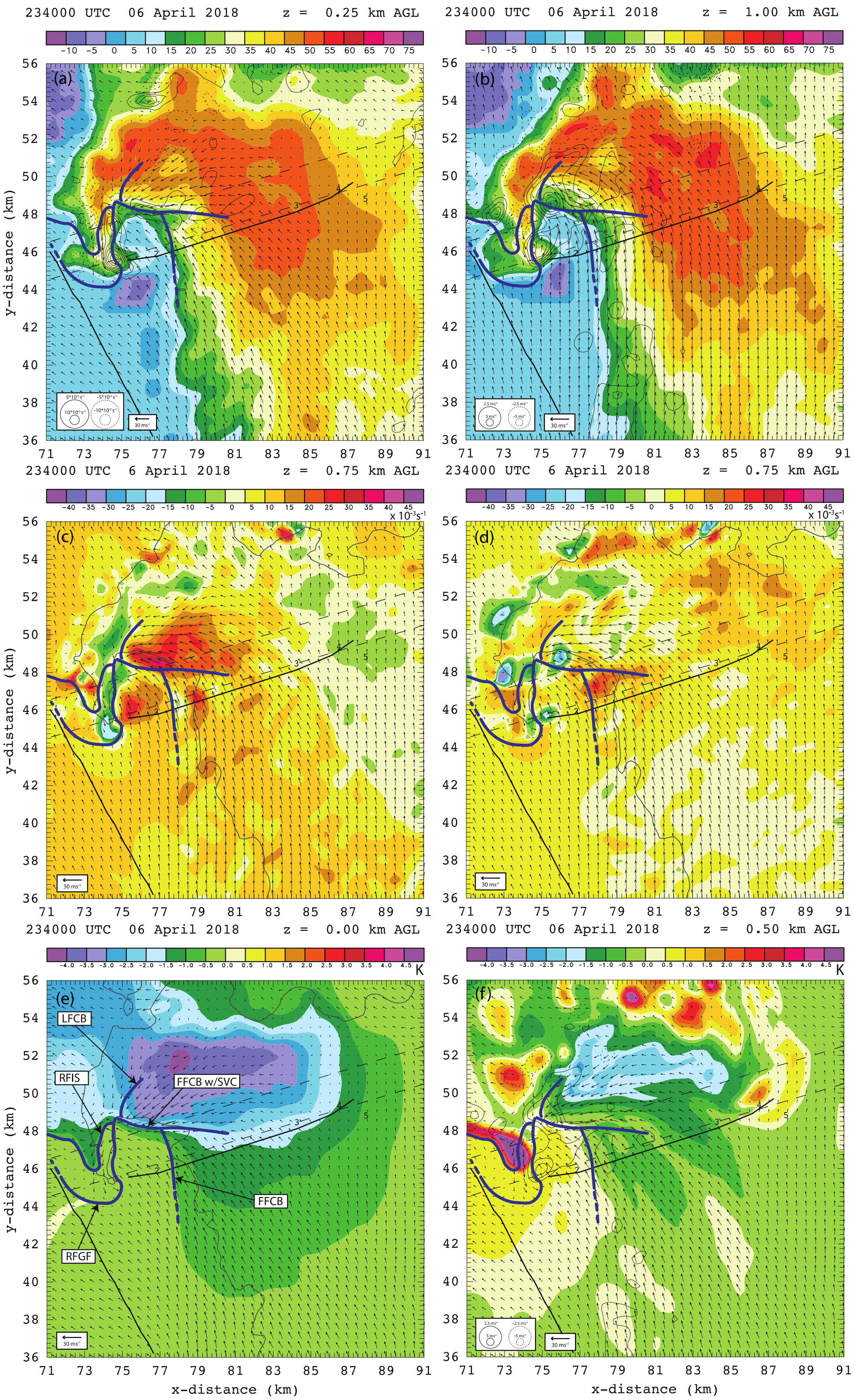
234000 UTC 06 April 2018 z = 0.25 km AGL
-10 -5 0 5 10 15 20 25 30 35 40 45 50 55 60 65 70 75
(a)
234000 UTC 06 April 2018 z = 1.00 km AGL
-10 -5 0 5 10 15 20 25 30 35 40 45 50 55 60 65 70 75
(b)
234000 UTC 6 April 2018 z = 0.75 km AGL
-40 -35 -30 -25 -20 -15 -10 -5 0 5 10 15 20 25 30 35 40 45
x 10⁻³s⁻¹
(c)
234000 UTC 6 April 2018 z = 0.75 km AGL
-40 -35 -30 -25 -20 -15 -10 -5 0 5 10 15 20 25 30 35 40 45
x 10⁻³s⁻¹
(d)
234000 UTC 06 April 2018 z = 0.00 km AGL
-4.0 -3.5 -3.0 -2.5 -2.0 -1.5 -1.0 -0.5 0.0 0.5 1.0 1.5 2.0 2.5 3.0 3.5 4.0 4.5
K
(e)
LFCB
RFIS
FFCB w/SVC
FFCB
RFGF
234000 UTC 06 April 2018 z = 0.50 km AGL
-4.0 -3.5 -3.0 -2.5 -2.0 -1.5 -1.0 -0.5 0.0 0.5 1.0 1.5 2.0 2.5 3.0 3.5 4.0 4.5
K
(f)
y-distance (km)
36 38 40 42 44 46 48 50 52 54 56
x-distance (km)
71 73 75 77 79 81 83 85 87 89 91
30 ms⁻¹
2.5 ms⁻¹
-2.5 ms⁻¹
5 ms⁻¹
-5 ms⁻¹
2 3 4 5

Figure 25. As in Figure 22, for 2340 UTC.

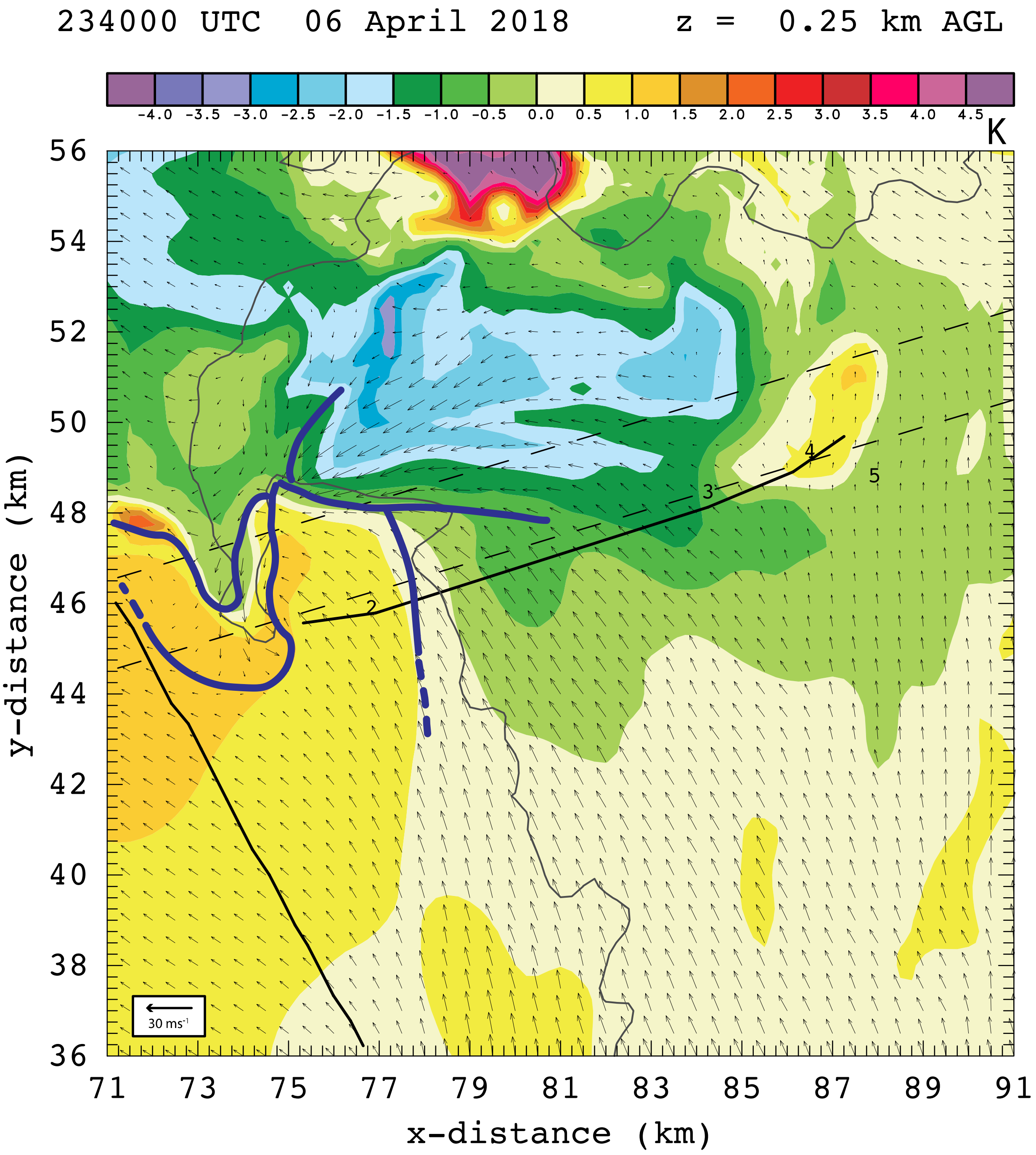

Figure 26. **Color-filled θ_v' with 10 dBZ contour at 0.25 km AGL at 2340 UTC. Surface boundaries and tornado damage track as in Figure 25e.**

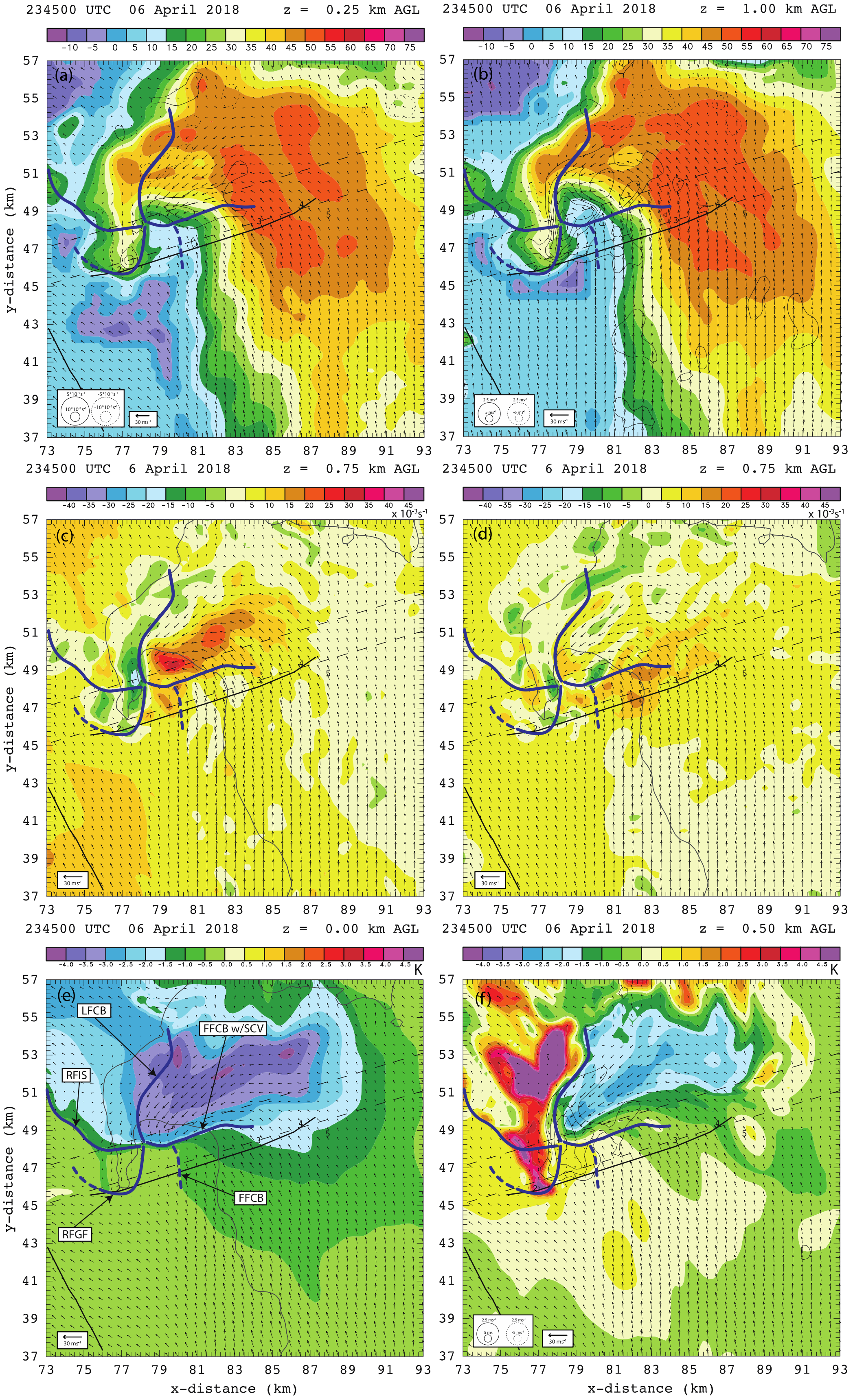
234500 UTC 06 April 2018 z = 0.25 km AGL
234500 UTC 06 April 2018 z = 1.00 km AGL
-10 -5 0 5 10 15 20 25 30 35 40 45 50 55 60 65 70 75
(a)
(b)
234500 UTC 6 April 2018 z = 0.75 km AGL
234500 UTC 6 April 2018 z = 0.75 km AGL
-40 -35 -30 -25 -20 -15 -10 -5 0 5 10 15 20 25 30 35 40 45
x 10⁻³s⁻¹
(c)
(d)
234500 UTC 06 April 2018 z = 0.00 km AGL
234500 UTC 06 April 2018 z = 0.50 km AGL
-4.0 -3.5 -3.0 -2.5 -2.0 -1.5 -1.0 -0.5 0.0 0.5 1.0 1.5 2.0 2.5 3.0 3.5 4.0 4.5
K
(e)
(f)
LFCB
FFCB w/SCV
RFIS
FFCB
RFGF
30 ms⁻¹
y-distance (km)
x-distance (km)
57 55 53 51 49 47 45 43 41 39 37
73 75 77 79 81 83 85 87 89 91 93

Figure 27. As in Figure 24, for 2345 UTC.

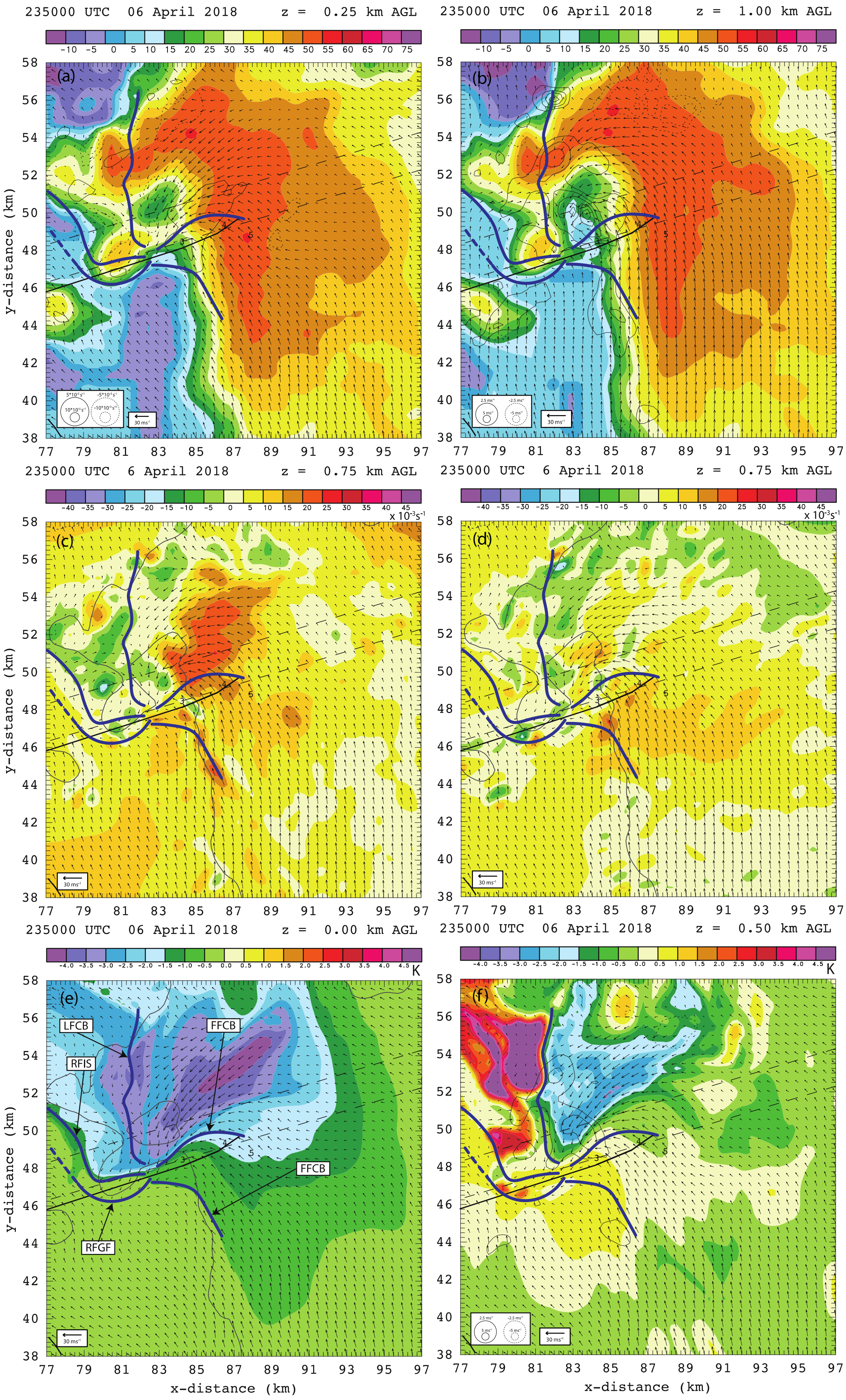
235000 UTC 06 April 2018 z = 0.25 km AGL
235000 UTC 06 April 2018 z = 1.00 km AGL
-10 -5 0 5 10 15 20 25 30 35 40 45 50 55 60 65 70 75
(a)
(b)
235000 UTC 6 April 2018 z = 0.75 km AGL
235000 UTC 6 April 2018 z = 0.75 km AGL
-40 -35 -30 -25 -20 -15 -10 -5 0 5 10 15 20 25 30 35 40 45
x 10-3s-1
(c)
(d)
235000 UTC 06 April 2018 z = 0.00 km AGL
235000 UTC 06 April 2018 z = 0.50 km AGL
-4.0 -3.5 -3.0 -2.5 -2.0 -1.5 -1.0 -0.5 0.0 0.5 1.0 1.5 2.0 2.5 3.0 3.5 4.0 4.5
K
(e)
(f)
LFCB
RFIS
FFCB
FFCB
RFGF
30 ms-1
y-distance (km)
x-distance (km)
38 40 42 44 46 48 50 52 54 56 58
77 79 81 83 85 87 89 91 93 95 97

Figure 28. As in Figure 24, for 2350 UTC.

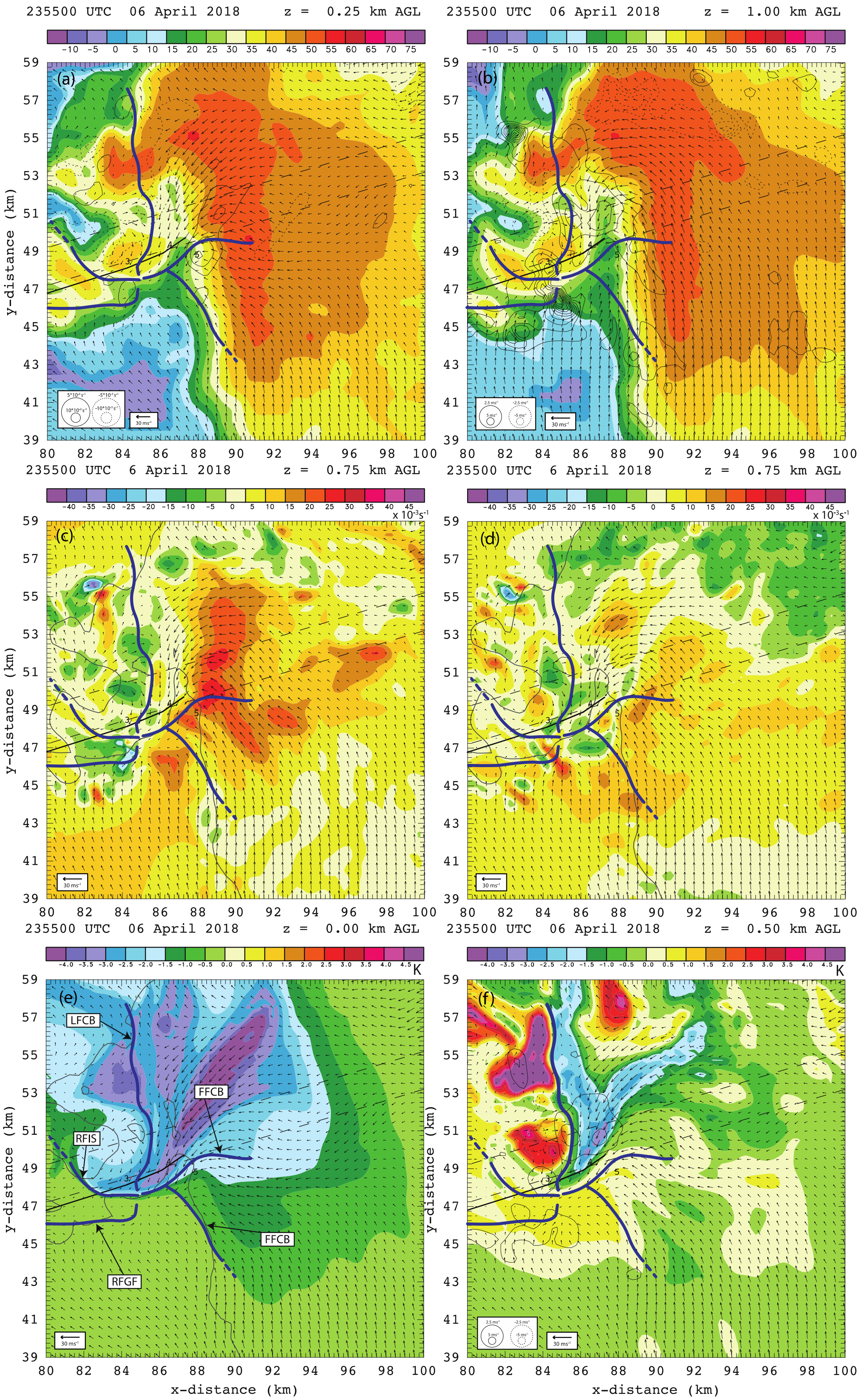
235500 UTC 06 April 2018 z = 0.25 km AGL
235500 UTC 06 April 2018 z = 1.00 km AGL
-10 -5 0 5 10 15 20 25 30 35 40 45 50 55 60 65 70 75
235500 UTC 6 April 2018 z = 0.75 km AGL
235500 UTC 6 April 2018 z = 0.75 km AGL
-40 -35 -30 -25 -20 -15 -10 -5 0 5 10 15 20 25 30 35 40 45
x 10⁻³s⁻¹
235500 UTC 06 April 2018 z = 0.00 km AGL
235500 UTC 06 April 2018 z = 0.50 km AGL
-4.0 -3.5 -3.0 -2.5 -2.0 -1.5 -1.0 -0.5 0.0 0.5 1.0 1.5 2.0 2.5 3.0 3.5 4.0 4.5 K
(a)
(b)
(c)
(d)
(e)
(f)
LFCB
FFCB
RFIS
FFCB
RFGF
3
4
5
30 ms⁻¹
y-distance (km)
x-distance (km)
39 41 43 45 47 49 51 53 55 57 59
80 82 84 86 88 90 92 94 96 98 100

Figure 29. As in Figure 24, for 2355 UTC.

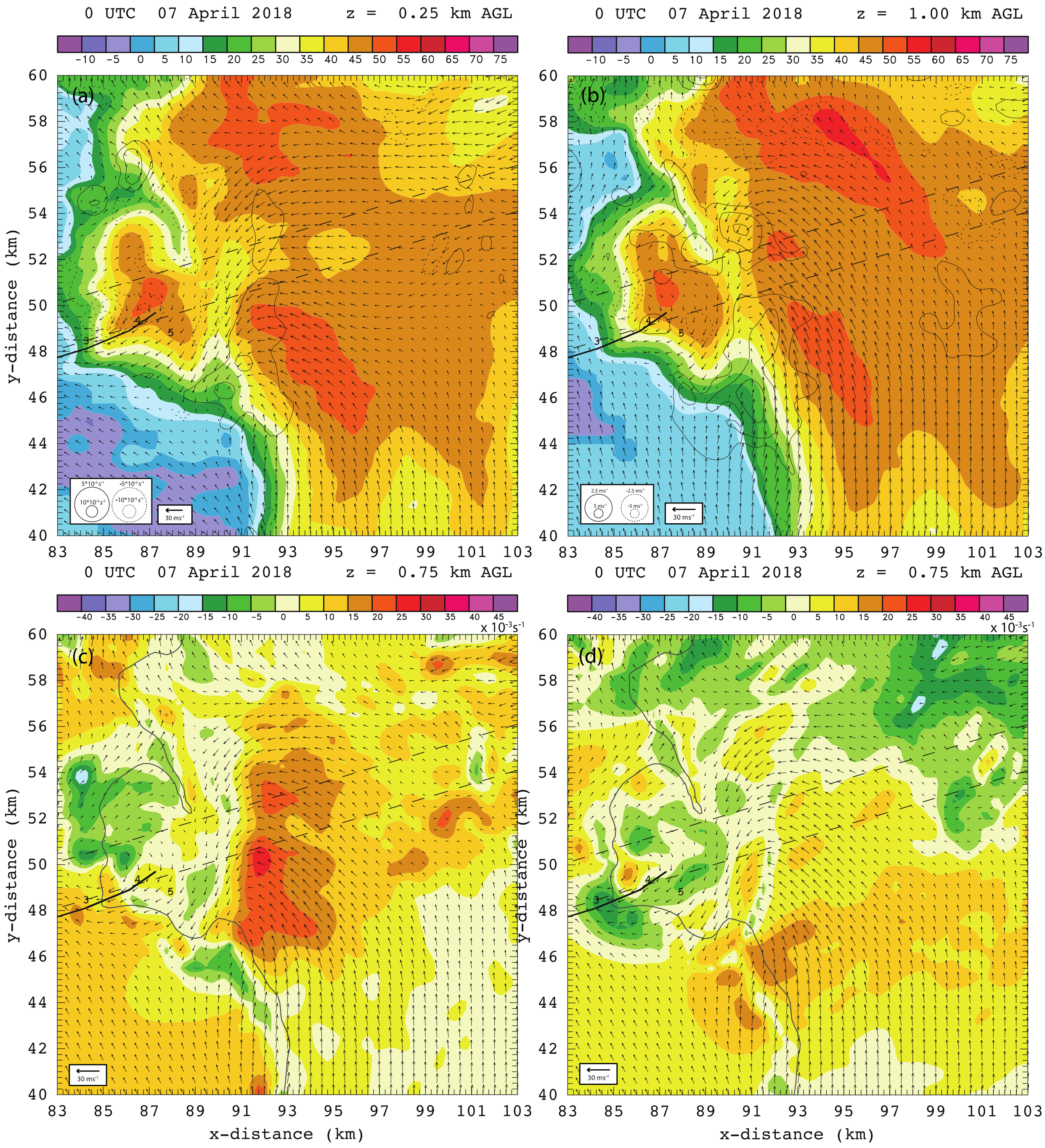

Figure 30. As in Figure 20, for 0000 UTC, with tornado damage track as in Figure 24.

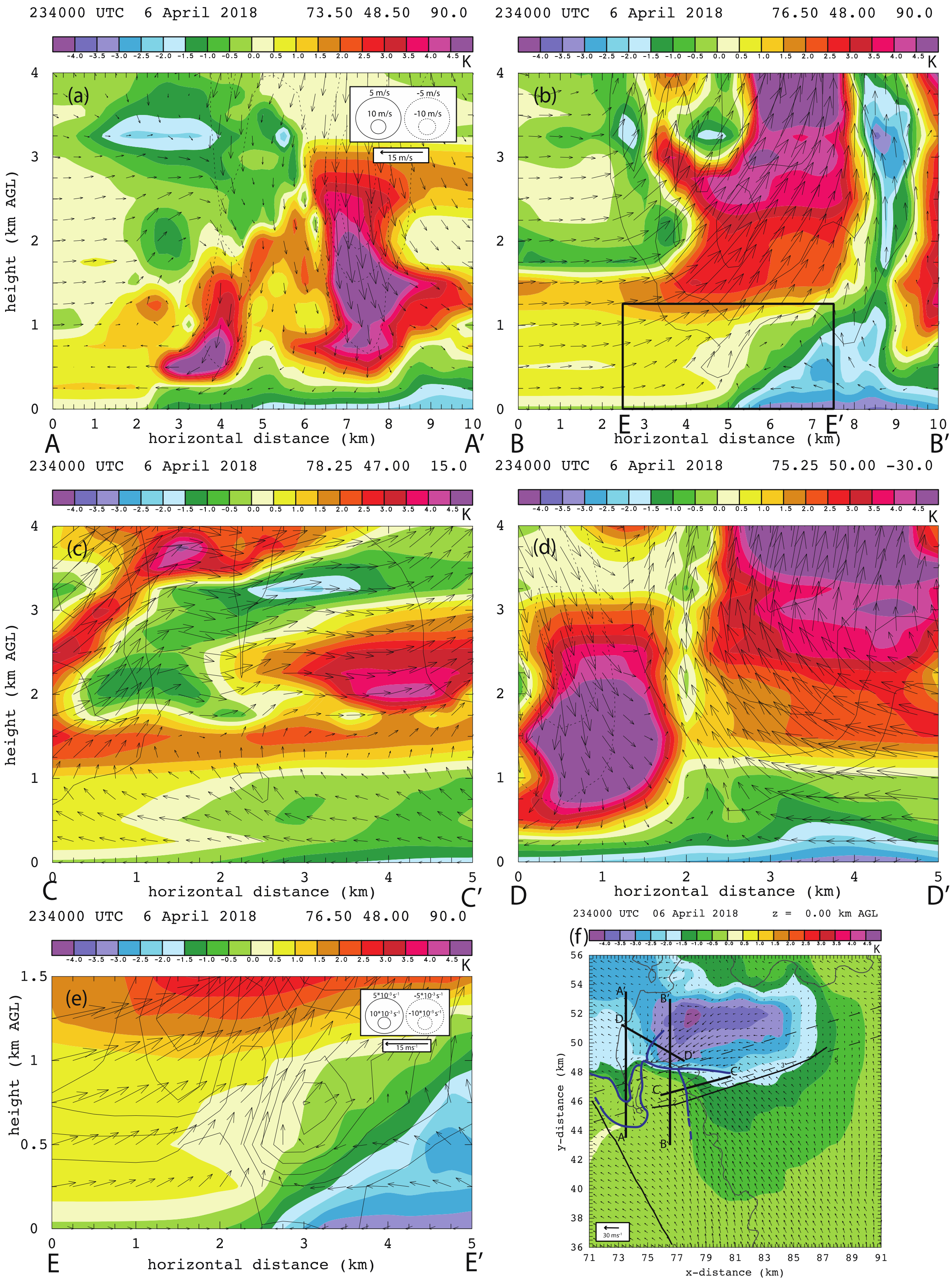
234000 UTC 6 April 2018 73.50 48.50 90.0
-4.0 -3.5 -3.0 -2.5 -2.0 -1.5 -1.0 -0.5 0.0 0.5 1.0 1.5 2.0 2.5 3.0 3.5 4.0 4.5 K
(a)
5 m/s
-5 m/s
10 m/s
-10 m/s
15 m/s
height (km AGL)
horizontal distance (km)
A
A′
234000 UTC 6 April 2018 76.50 48.00 90.0
(b)
E
E′
B
B′
234000 UTC 6 April 2018 78.25 47.00 15.0
(c)
C
C′
234000 UTC 6 April 2018 75.25 50.00 -30.0
(d)
D
D′
234000 UTC 6 April 2018 76.50 48.00 90.0
(e)
5*10⁻³s⁻¹
-5*10⁻³s⁻¹
10*10⁻³s⁻¹
-10*10⁻³s⁻¹
15 ms⁻¹
E
E′
234000 UTC 06 April 2018 z = 0.00 km AGL
(f)
y-distance (km)
x-distance (km)
30 ms⁻¹
A
A′
B
B′
C
C′
D
D′

Figure 31. Color-filled θ_v' with 10 dBZ contour at the surface at 2340 UTC, with surface boundaries drawn in as in Figure 25e with associated 4 km—high vertical cross sections of θ_v' (fill) with vertical velocity contoured (a—d) and 1.5 km—high streamwise vorticity contoured vertical cross section (e). Black labeled lines represent the location of the associated cross sections. (a) cuts through the RFGF and RFIS, (b) cuts through the eastward-FFCB and its associated SVC, (c) cuts through the southern-FFCB, (d) cuts through the LFCB, and (e) is a subsection of (b). The legend for (a—d) is located at the top right corner of (a).

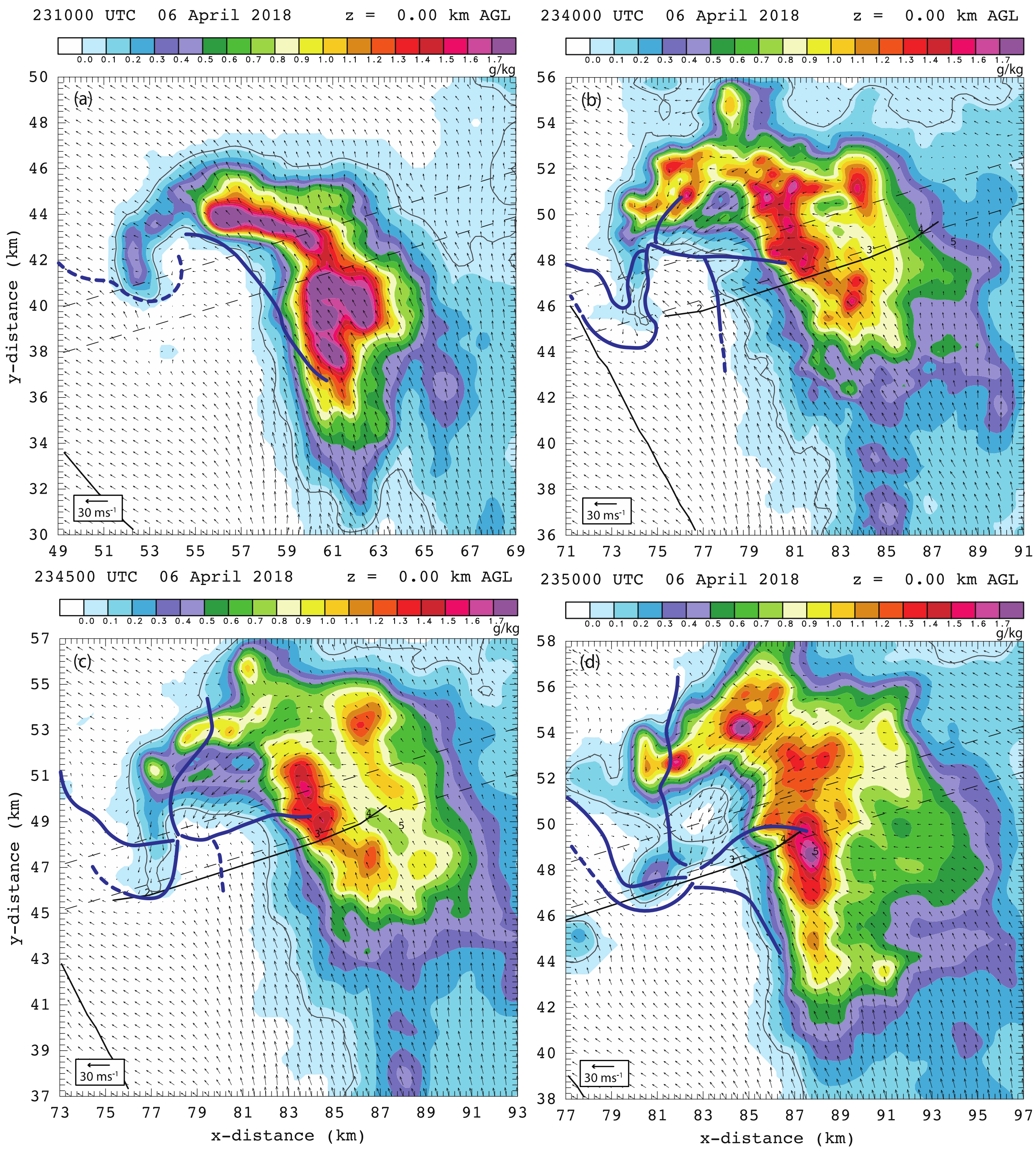

Figure 32. Rainwater mixing ratio (fill) with 10 dBZ contour at 2310 UTC (a), 2340 UTC (b), 2345 UTC (c), and 2350 UTC (d). Surface boundaries are drawn in as in Figures 21, 25, 26, and 27 respectively.

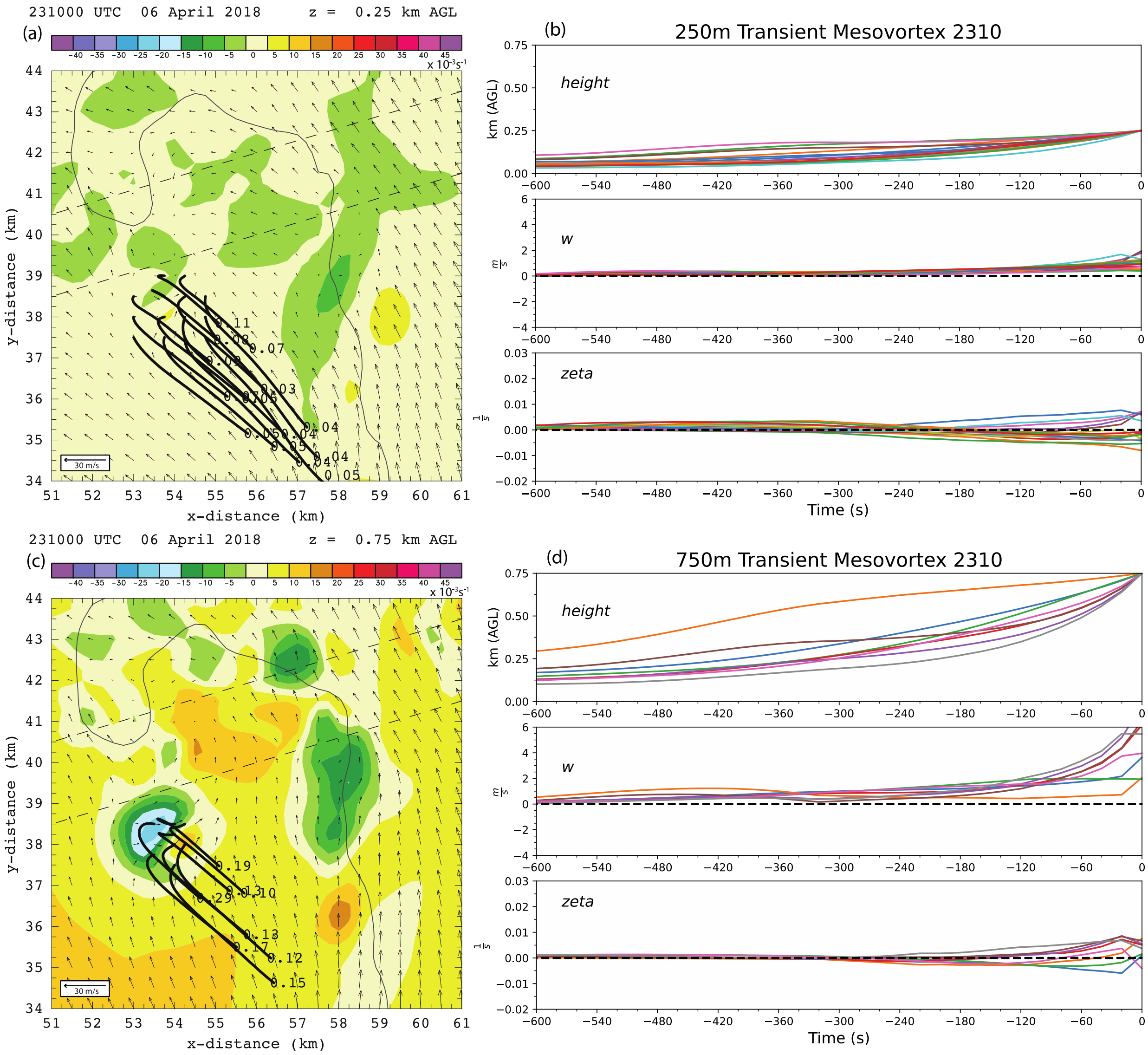

Figure 33. Streamwise vorticity fill with 10 dBZ contour at 0.25 km AGL at 2310 UTC with 14 10-minute long storm-relative trajectories ending at 0.25 km AGL within the Early Transient Mesovortex (a), along with the associated 10-minute time series of height, vertical velocity, and vertical vorticity of said trajectories (b). (c) and (d) are the same as (a) and (b), respectively, but for 8 10-minute long trajectories ending at AGL within the Early Transient Mesovortex and (c) plotted at 0.75 km AGL. Number labels associated with each trajectory in (a) and (c) represent the height, in km AGL, of each individual trajectory at its origin point.

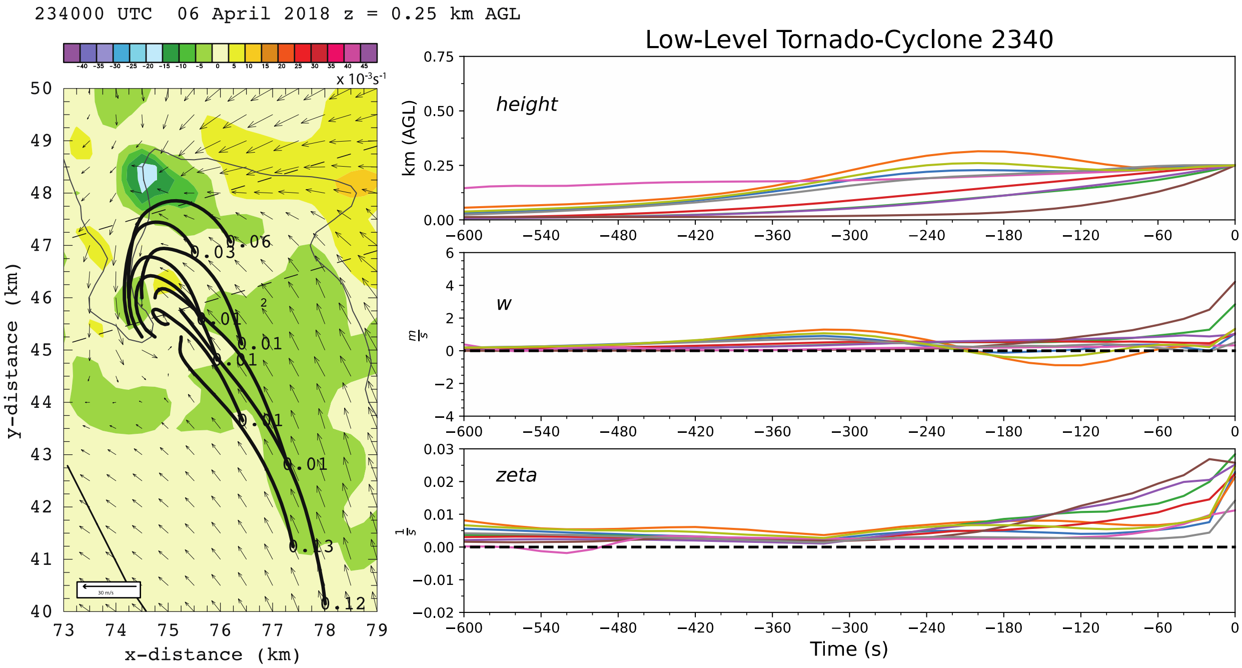

Figure 34. Streamwise vorticity fill with 10 dBZ contour at 0.25 km AGL at 2340 UTC with nine 10-minute long storm-relative trajectories ending at 0.25 km AGL within the tornado-cyclone (left), with associated height, vertical velocity, and vertical vorticity timeseries of said trajectories (right).

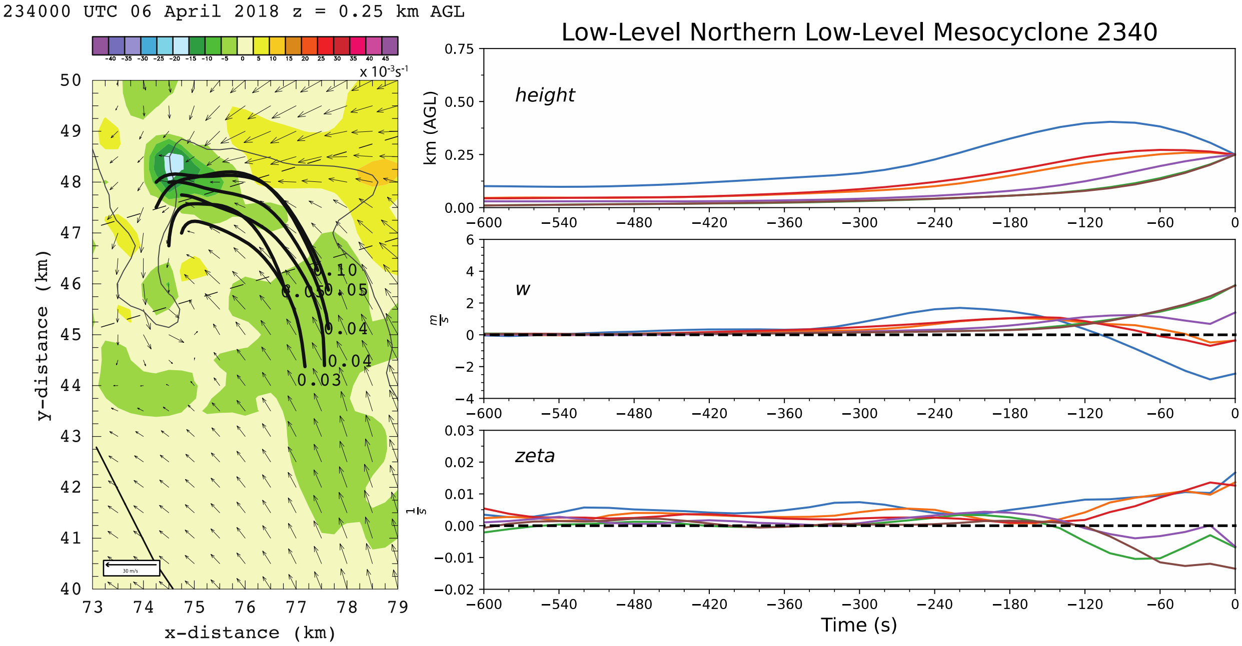

Figure 35. As in Figure 34, with six 10-minute long trajectories ending at 0.25 km AGL within the Northern low-level mesocyclone.

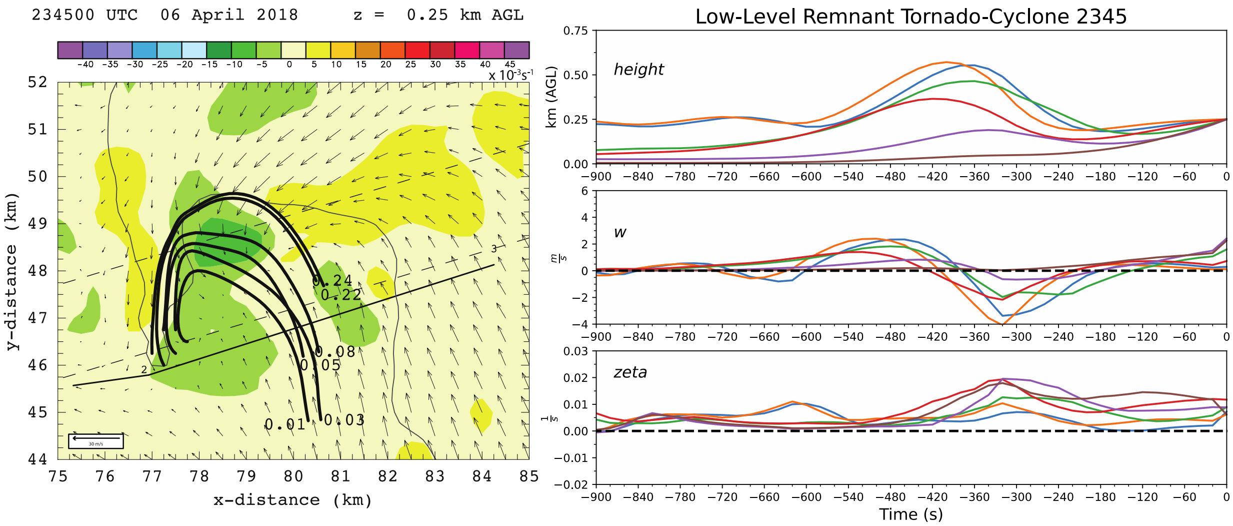

Figure 36. As in Figure 34, with 6 15-minute long trajectories ending at 0.25 km AGL within the remnant tornado-cyclone at 2345 UTC.

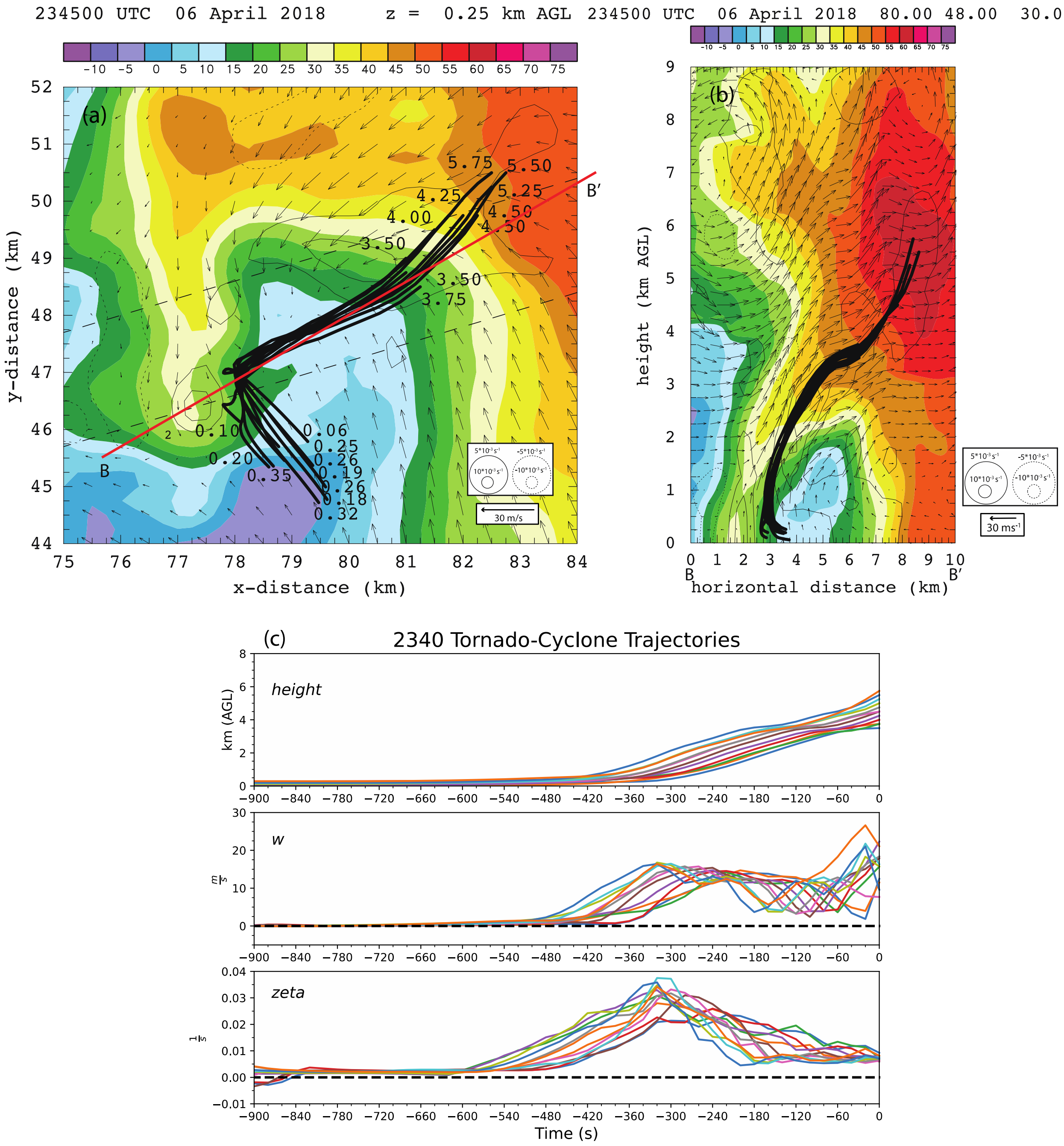

Figure 37. Reflectivity fill with vertical vorticity contoured at 0.25 km AGL at 2345 UTC with ten 15-minute long storm-relative trajectories which passed through the tornado-cyclone at 2340 UTC (a), a 9 km-deep vertical cross section of reflectivity fill with vertical vorticity contour with the projection of the trajectories (b), denoted by the red line in (a), and the corresponding timeseries of height, vertical velocity, and vertical vorticity of said trajectories (c). Number labels at the beginning and end of trajectories in (a) represent the beginning and ending height, respectively, in km AGL.

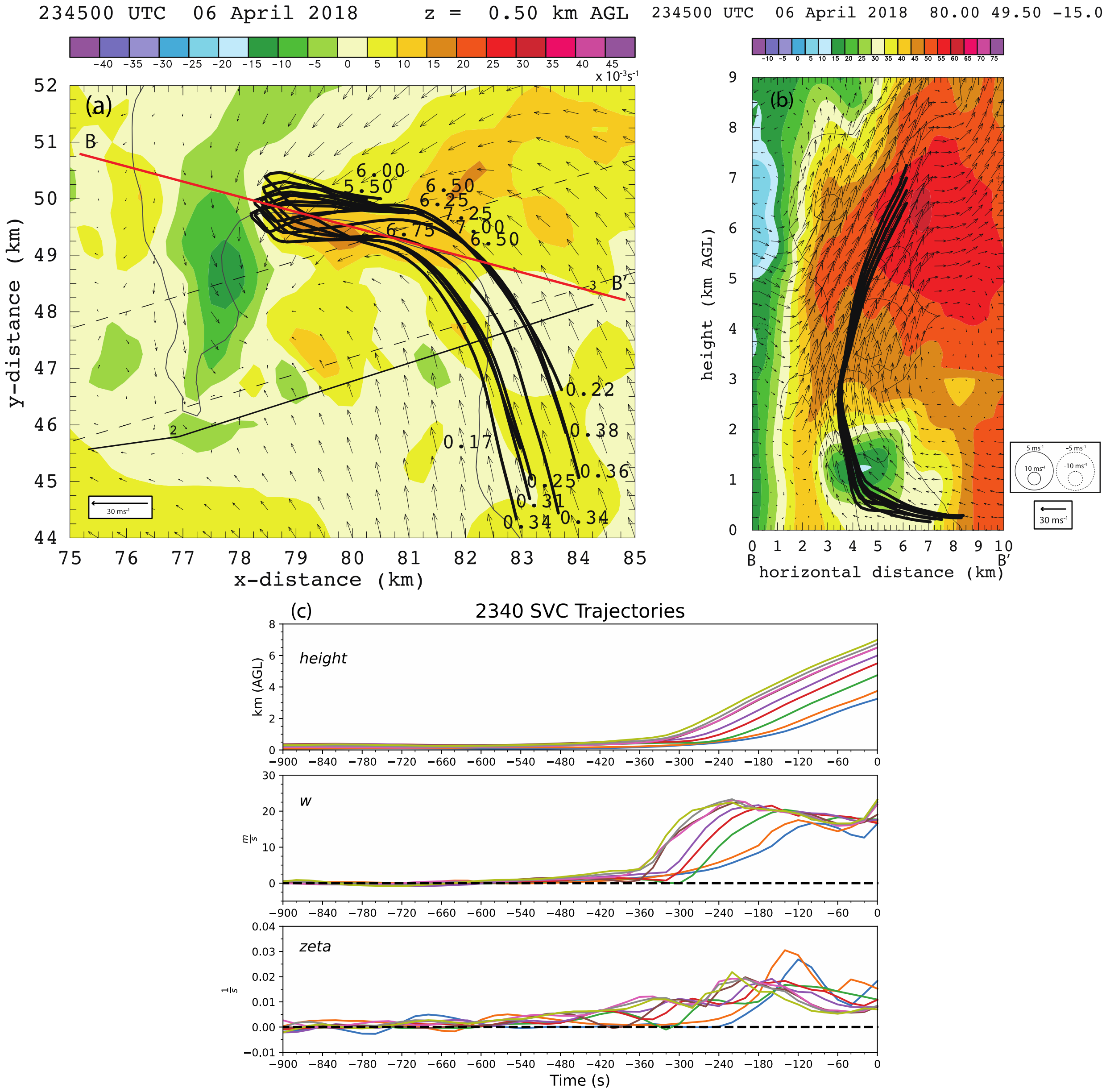

Figure 38. As in Figure 37, with streamwise vorticity fill and 10 dBZ contour at 0.5 km AGL at 2345 UTC (a) and with eight 15-minute long storm-relative trajectories which passed through the SVC at 2340 UTC.

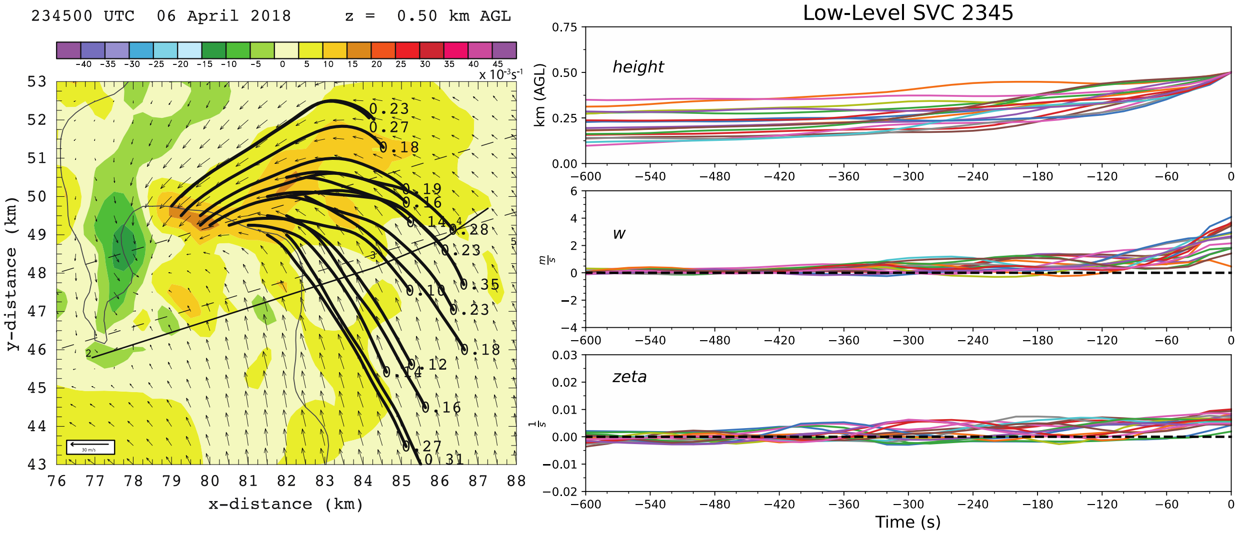

Figure 39. As in Figure 35, with streamwise vorticity fill with 10 dBZ contour at 0.5 km AGL at 2345 UTC, with 17 10-minute long trajectories ending at 0.5 km AGL within the SVC and broad region of enhanced streamwise vorticity (left) and their associated timeseries of height, vertical velocity, and vertical vorticity (right).

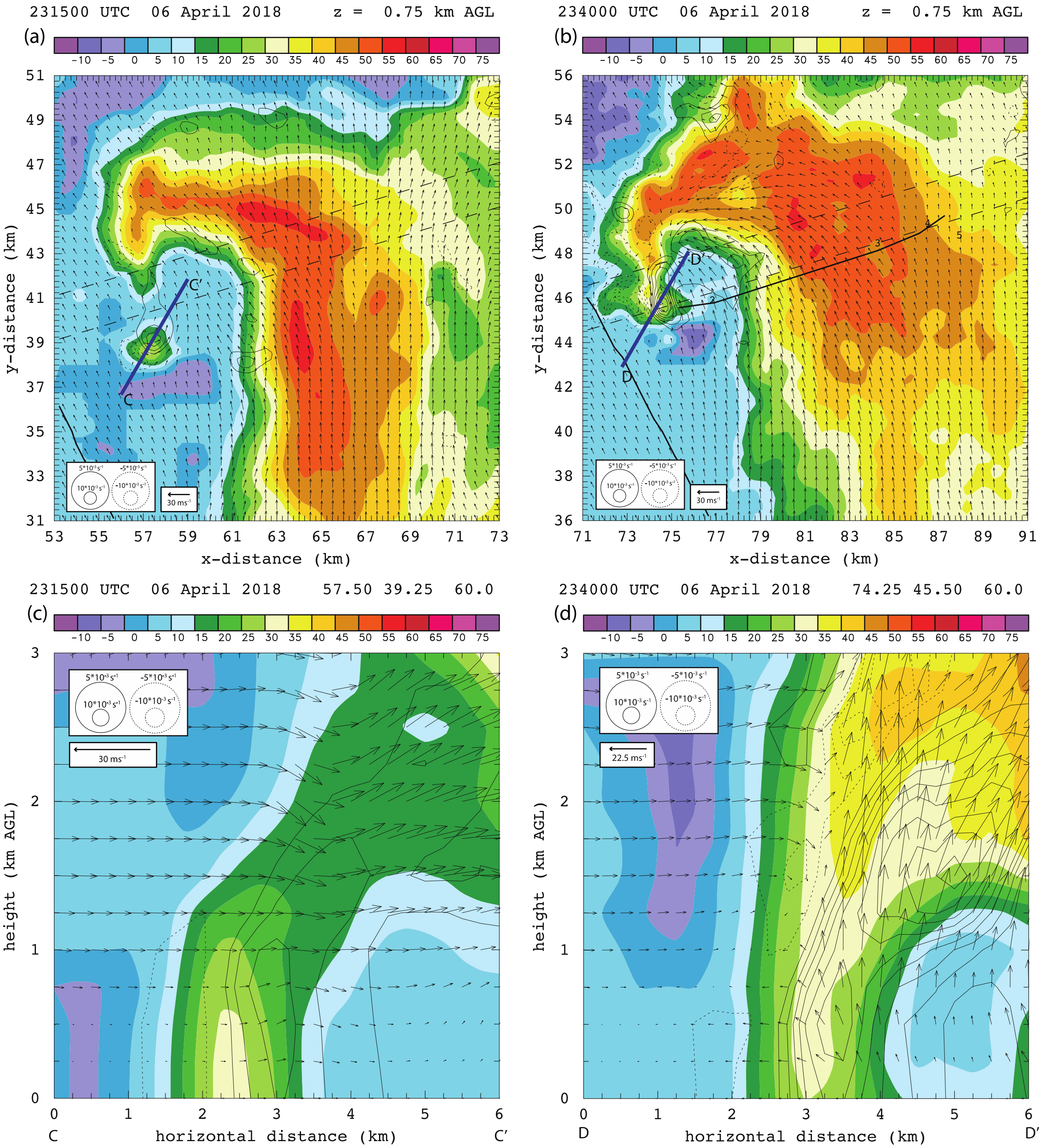

Figure 40. Reflectivity fill with vertical vorticity contour at 0.75 km AGL at 2315 UTC (a) and 2340 UTC (b). Blue labeled lines denote the location of 3 km-deep vertical cross sections of reflectivity fill with vertical vorticity contour through the Early Transient Mesovortex (c) and tornado-cyclone (d).

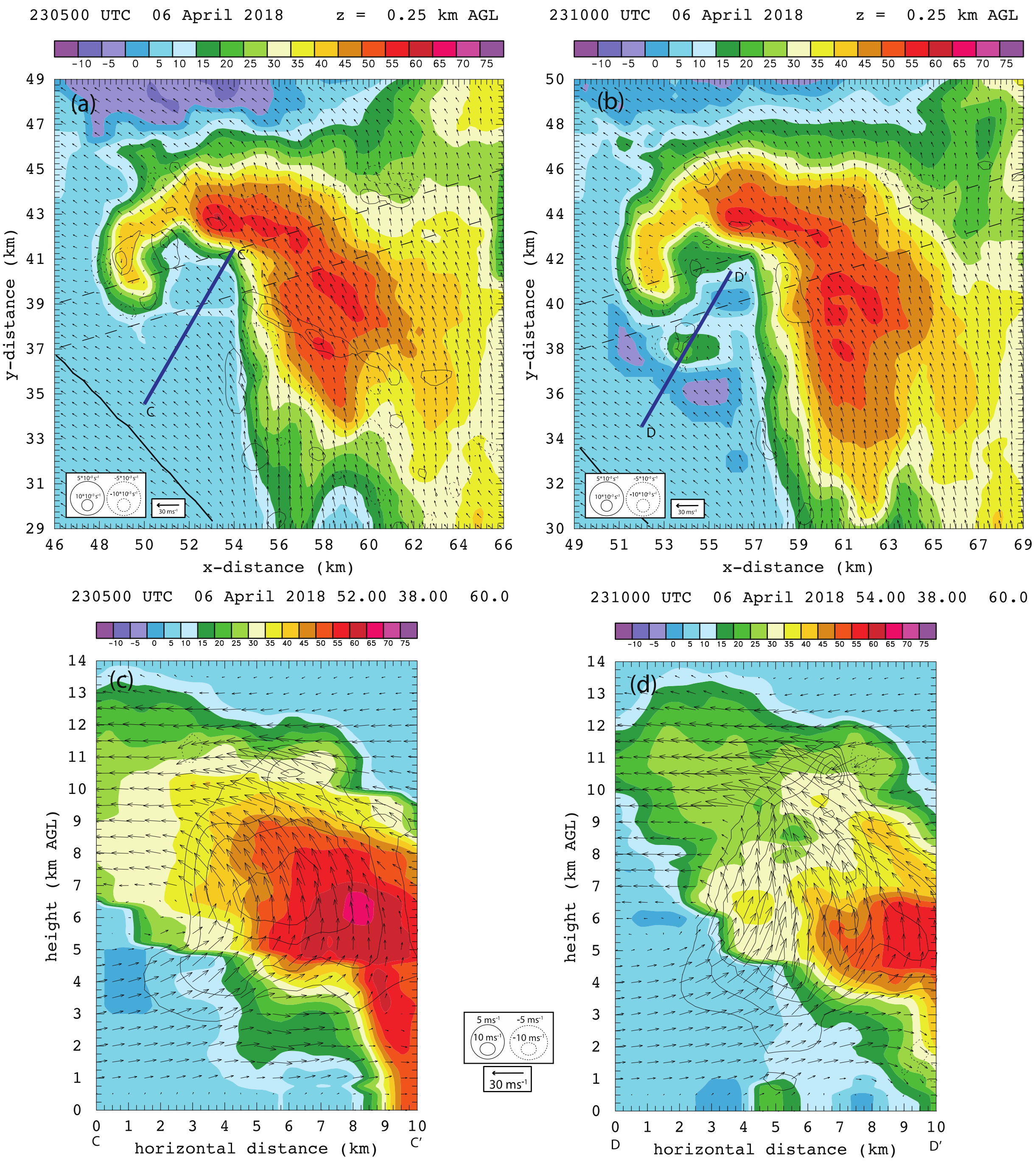

Figure 41. Sequence of reflectivity fill with vertical vorticity contoured at 0.25 km AGL at 2305 UTC (a) and 2310 UTC (b) with labeled solid blue lines representing 14 km-deep cross sections of reflectivity fill with vertical velocity contoured through the Early Transient Mesovortex at 2305 UTC (c) and 2310 UTC (d), respectively.

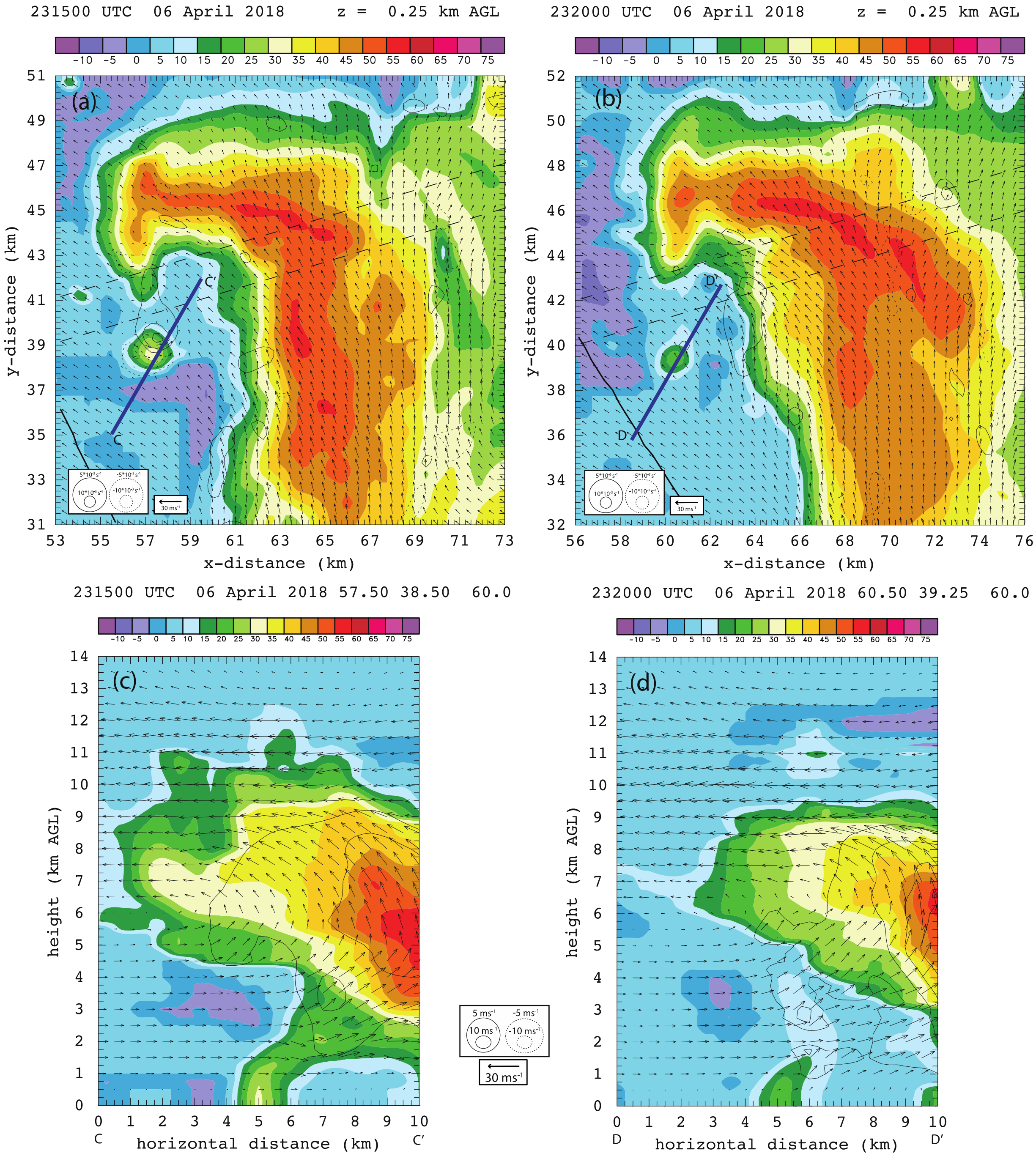

Figure 42. As in Figure 41, but for 2315 UTC (a, c) and 2320 UTC (b, d).

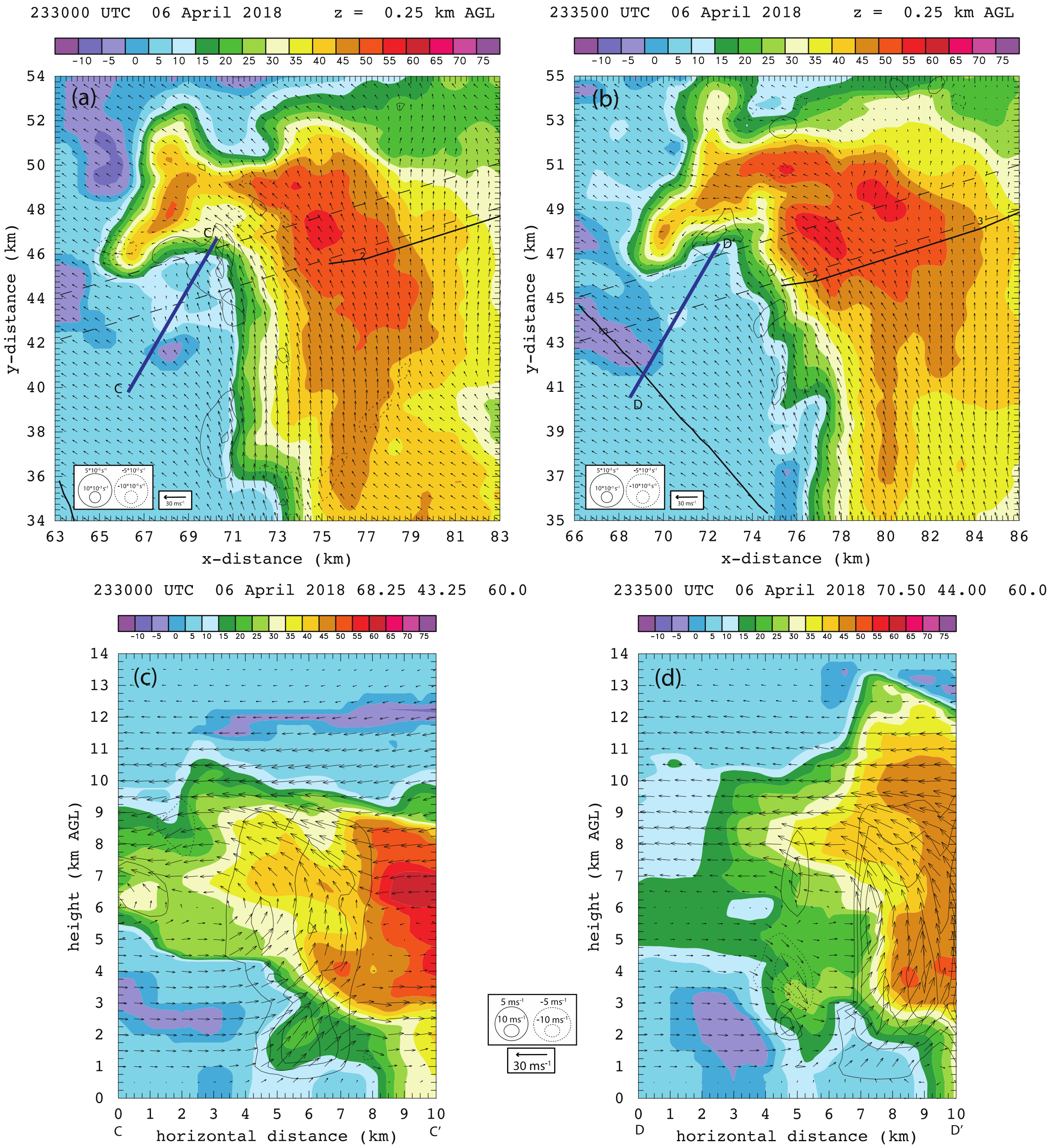

Figure 43. As in Figure 41, but for the development of the tornado-cyclone at 2330 UTC (a, c) and 2335 UTC (b, d).

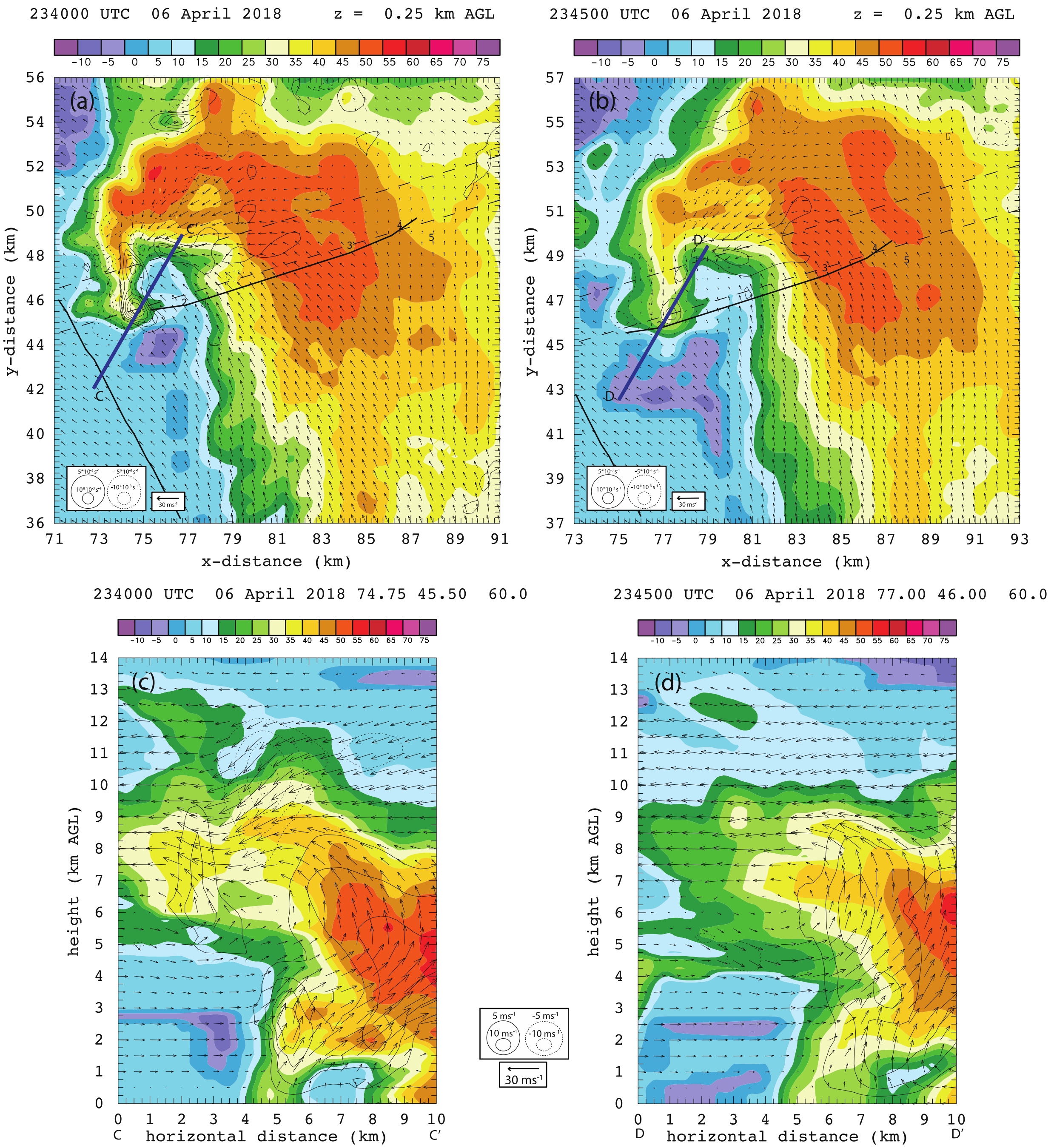

Figure 44. As in Figure 43, but at 2340 UTC (a, c) and 2345 UTC (b, d).

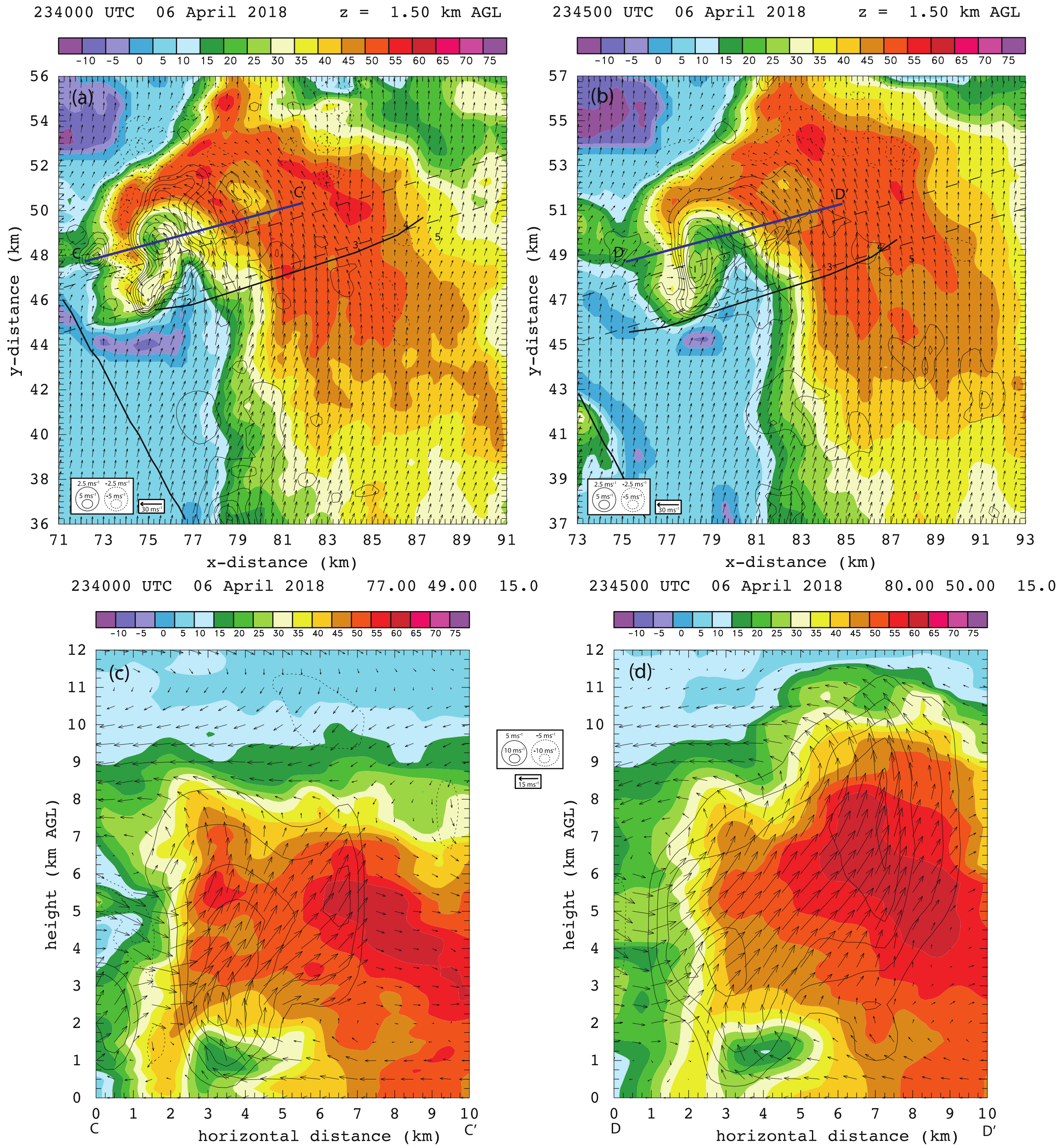

Figure 45. Reflectivity fill with vertical velocity contoured at 1.5 km AGL at 2340 UTC (a) and 2345 UTC (b), with 12 km-deep cross sections of reflectivity fill with vertical velocity contoured (c and d, respectively). Cross section location is denoted by the labeled blue line on (a) and (b).

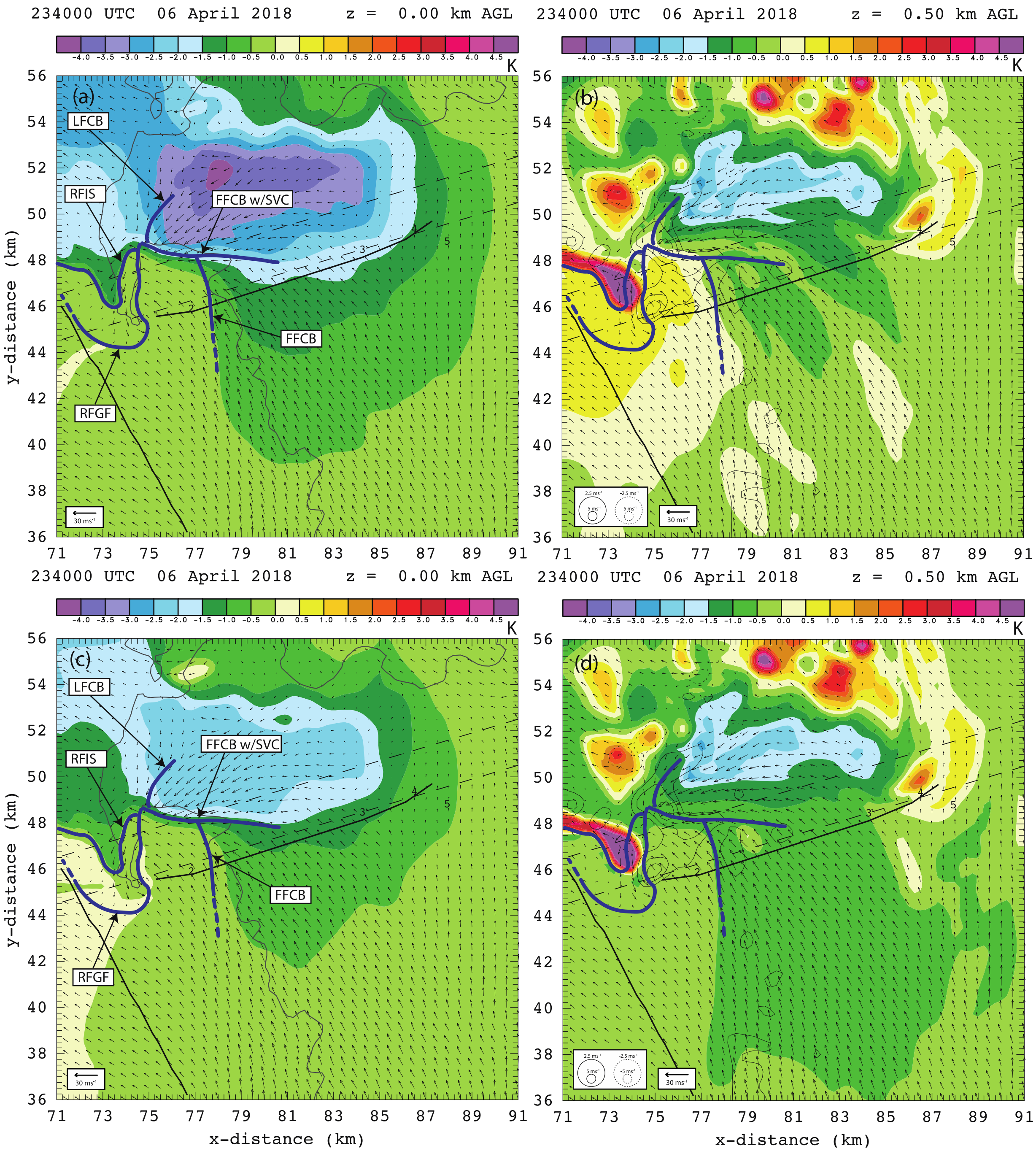

Figure 46. Color-filled θ_v' with 10 dBZ contour at 0 km AGL at 2340 UTC (a, c) and θ_v' (fill) with vertical velocity contoured at 0.5 km AGL at 2340 UTC (b, d). (a) and (b) are from the Control DLA run using the CRL-modified thermodynamic profile combined with the Gilbert proximity sounding, while (c) and (d) were a sensitivity test run with only the Gilbert proximity sounding (Test DLA). Surface boundaries (dark blue lines) are as in Figure 25, and were drawn from the Control DLA.